

POLITECNICO DI MILANO

School of Industrial and Information Engineering

Master's Degree in Materials Engineering and Nanotechnology



**FINITE ELEMENT SIMULATION OF
LASER FLASH ANALYSIS FOR INVESTIGATING THE
FILLER ORIENTATION EFFECT ON
THERMAL CONDUCTIVITY OF PLASTIC COMPOUNDS**

Supervisor: Prof. Stefano Ettore Romano Turri

Co-advisors:

Maria Agnese Zappa

Romeo Mauro

Luca Posca

Candidate:

Monika Doneva

10643845

Academic Year 2020/2021

Acknowledgements

I wish to express my honest gratitude and appreciation to my supervisor, Prof. Stefano Turri for his guidance and for his kindness in providing me the opportunity to do this thesis.

I would like to sincerely thank Luca Posca and Francesco Manarini for giving me their trust and making the thesis possible through exceptional organization. I am grateful to the company LATI for the valuable learning experience in a professional and motivating environment. I wish to express my sincere appreciation to everyone I had the pleasure to work with during my time there, for all their help, knowledge and patience. My appreciations go to Annacarla Cereti for her part in the injection molding and for her enthusiasm in the demonstration of characterization techniques. Many thanks to Jacopo Carabelli for adding considerable value to the present work with the acquisition of SEM images. Furthermore, I would like to extend my special thanks to Maria Agnese Zappa and Romeo Mauro for being always available to answer my doubts and provide me guidance and support in the work and the writing of the thesis. I am grateful to have learned a lot from their professionalism and expertise.

I gratefully acknowledge Whitecroft Lighting (UK) for providing thermography measurements and kindly allowing me to present the results in my thesis.

I must express my most profound gratitude to my family for their unconditional support and continuous encouragement during my studies. This accomplishment truly would not have been possible without them. Finally, I am extremely thankful to my boyfriend for being by my side and being inspiring, reassuring and understanding throughout this experience.

Thank you.

Abstract

Computational modeling with finite element analysis (FEA) is a valuable engineering tool for studying any physical phenomenon. Its implementation reduces the number of physical prototypes and experiments and it is a cost-effective way to better understand, predict and optimize the behavior of a given component. The aim of the present work is to evaluate the accuracy of a model for determining the anisotropic thermal conductivity of injection molded polymer composites. This was accomplished by means of comparison between experimental and simulation results for the thermal conductivity.

The laboratory measurements were carried out using laser flash analysis (LFA). Two polyamide 6-based compounds, containing 50 wt% and 70 wt% of graphite (labeled as GR/50 and GR/70, respectively) as a thermally conductive filler were considered for the investigation. Samples used for the LFA were acquired from 1.47 mm and 3.2 mm thick injection molded flame bars, under the assumption that the higher shear stress in the thinner cavity will result in stronger filler alignment along the flow direction. LFA measurements for the through-plane (TP) and in-plane (IP) conductivity of the bars were performed for specimens taken from the central zone and the zone near the injection gate. Results revealed an unanticipated trend for the directional thermal conductivity as a function of bar thickness for the compound named as GR/50. Although IP conductivity was expected to be higher for the 1.47 mm thick bars due to the higher graphite flake orientation, these samples showed slower heat transport in both directions. Such outcome is potentially explained through the relative size of the skin-core layers and the degree of filler dispersion. This trend was repeated for GR/50 specimens obtained using higher injection rates. On the other hand, results for the GR/70 material were in line with the assumption and samples with 1.47 mm thickness displayed higher IP thermal conductivity.

The FEA section of the thesis comprised simulations of the injection molding and the LFA. The latter were carried out by performing transient thermal analyses for an isotropic and an anisotropic model. The anisotropic model, obtained by Excel macros developed in LATI, produced results with a very good experimental agreement. The highest percent error for values of the thermal conductivity was 28.8%, while the smallest was only 0.7%.

Finally, the accuracy of the anisotropic model was evaluated for a case study based on a collaboration between LATI and Whitecroft Lighting. Simulation results were compared with thermographically measured temperature distributions for a GR/50 heat sink used for light-emitting diode (LED) downlights. The end result suggested that the anisotropic model needs to be revised for use in complex geometries. Enhanced accuracy is expected with using computational fluid dynamics (CFD) for a more correct estimation of the convection coefficients.

Sommario

L'analisi agli elementi finiti (FEA) è un prezioso strumento di ingegneria per lo studio di qualsiasi fenomeno fisico. La sua implementazione riduce il numero di prototipi ed esperimenti fisici ed è un modo conveniente per ottimizzare, prevedere e comprendere meglio il comportamento di un dato componente. Lo scopo del presente lavoro è valutare l'accuratezza di un modello per determinare la conducibilità termica anisotropa di compositi polimerici stampati a iniezione. Ciò è stato eseguito dal confronto tra i risultati sperimentali e di simulazione per la conducibilità termica.

Le misurazioni di laboratorio sono state effettuate utilizzando il metodo del laser flash (LFA). Per l'indagine sono stati presi in considerazione due compositi a base di poliammide 6, contenenti il 50% e 70% in massa di grafite (etichettati rispettivamente come GR/50 e GR/70) come additivo termoconduttivo. I campioni utilizzati per l'LFA sono stati ottenuti da provini per analisi UL di spessore 1,47 mm e 3,2 mm stampate a iniezione, presumendo che il maggiore sforzo di taglio nella cavità più sottile si tradurrà in un allineamento più marcato del riempitivo lungo la direzione del flusso d'iniezione. Le misurazioni LFA per la conducibilità fuori dal piano (TP) e nel piano (IP) dei provini sono state eseguite per campioni prelevati dalla zona centrale e dalla zona vicino al foro di iniezione. I risultati hanno rivelato una tendenza imprevista per la conducibilità termica in direzione dello spessore nel caso del composito denominato GR/50. Sebbene ci si aspettasse che la conduttività IP fosse maggiore per le barre spesse 1,47 mm a causa del maggiore orientamento delle scaglie di grafite, questi campioni hanno mostrato un trasporto di calore più lento in entrambe le direzioni. Tale risultato è potenzialmente spiegato attraverso la dimensione relativa degli strati della morfologia "skin-core" e il grado di dispersione dell'additivo. Questa tendenza è stata rilevata anche nei campioni GR/50 ottenuti utilizzando velocità di iniezione più elevate. D'altra parte, i risultati per il materiale GR/70 erano in linea con l'ipotesi e campioni con uno spessore di 1,47 mm hanno mostrato una conduttività termica IP superiore.

La sezione FEA della tesi comprendeva simulazioni dello stampaggio a iniezione e dell'LFA. Questi ultimi sono stati effettuati eseguendo analisi termiche transitorie per un modello isotropo e uno anisotropo. Il modello anisotropo, ottenuto dalle macro Excel sviluppate in LATI, ha prodotto risultati con un ottimo accordo sperimentale. L'errore percentuale più alto per i valori della conducibilità termica era del 28,8%, mentre il più piccolo era solo dello 0,7%.

Infine, l'accuratezza del modello anisotropo è stata valutata per un caso di studio basato su una collaborazione tra LATI e Whitecroft Lighting. I risultati della simulazione sono stati confrontati con le distribuzioni di temperatura misurate termograficamente per un dissipatore di calore GR/50 utilizzato per i faretto a diodi a emissione di luce (LED). Il risultato finale ha suggerito che il modello anisotropo deve essere rivisto per l'uso in geometrie complesse. Si prevede una maggiore precisione con l'utilizzo della fluidodinamica computazionale (CFD) per una stima più corretta dei coefficienti di convezione.

Table of Contents

Introduction	1
1. Theoretical framework.....	4
1.1. Polymer thermal conductivity	4
1.1.1. Thermally conductive fillers: overview	5
1.1.1.1. Metallic fillers	5
1.1.1.2. Ceramic fillers.....	6
1.1.1.3. Carbon-based fillers	6
1.1.1.4. Hybrid fillers.....	7
1.1.2. Orientation effect	7
1.1.3. Methods for measuring thermal conductivity.....	9
1.1.3.1. Steady-state methods.....	10
Guarded hot plate	10
Heat flow meter	11
Radial heat flow.....	11
1.1.3.2. Transient methods.....	11
Laser flash technique	12
Transient hot wire.....	14
Transient plane source.....	15
1.1.4. Mathematical modelling of thermal conductivity in polymer composites ..	15
1.1.4.1. Theoretical models for composites	15
1.1.4.2. Simulation models of composites	17
1.2. Injection molding	18
1.2.1. Filler orientation in injection molded composites.....	19
2. Materials and methods	22
2.1. Material characterization	22
2.2. Injection molding	22
2.2.1. Series 1.....	23
2.2.2. Series 2.....	23
2.3. Laser flash analysis (LFA).....	25
2.4. Finite element analysis (FEA)	26
2.4.1. Injection molding simulation.....	26
2.4.2. Laser flash simulation	28

2.4.3. Flake orientation mapping.....	32
2.4.4. Case study.....	34
3. Results and discussion.....	36
3.1. Material characterization	36
3.2. LFA experimental results	38
3.2.1. Series 1.....	38
3.2.2. Series 2.....	43
3.3. Injection molding simulation results	44
3.4. LFA simulation results.....	51
3.5. Case study	60
Conclusions and future work	64
Bibliography.....	67

List of figures

Figure 1. Schematic representation of: a) two-specimen; b) single-specimen GHP apparatus [56].	10
Figure 2. a) Diagram of the laser flash experiment [61]. b) LFA measurement principle [62].	12
Figure 3. Temperature history curve. The maximum temperature rise (ΔT_{max}) is inversely proportional to the mass (m) and specific heat (C_p) of the specimen [63].	13
Figure 4. Schematic of an injection molding machine [86].	18
Figure 5. Comparison between the through-thickness velocity and shear rate distributions for: a) Newtonian and non-Newtonian fluids; b) isothermal and non-isothermal conditions for a non-Newtonian fluid (adapted from [85]).	20
Figure 6. Filler reorientation with polymer melt passing through: a) a convergent channel; b) a divergent channel [85].	20
Figure 7. Diagram of the fountain flow present at the melt front [85].	21
Figure 8. Skin-core orientation of fillers in injection molded polymeric compounds (exaggerated) [90].	21
Figure 9. Pellets used for injection molding: a) GR/50; b) GR/70 compound.	22
Figure 10. Moldex3D material database viscosity curves for: a) GR/50; b) GR/70..	24
Figure 11. Cutting injection molded flame bars to obtain: a) through-plane; b) in-plane thermal conductivity LFA samples. The bar thickness is as previously defined (1.47 or 3.2 mm).	25
Figure 12. Schematic representation of: a) TP; b) IP thermal diffusivity samples and sample holders (adapted from [61]).	26
Figure 13. Geometry and runner system for flame bar of: a) 1.47 mm; b) 3.2 mm thickness.	27
Figure 14. Experimental pulse profiles of the: a) 0.3 ms and b) 1 ms pulse width... ..	29
Figure 15. Simplified pulse shapes for the: a) 0.3 ms; b) and c) 1 ms pulse width used for the simulation of LFA.	29
Figure 16. Extrapolation for obtaining: a) the minimum thermal conductivity and b) the maximum thermal conductivity for the GR/70 polymer compound.	31

Figure 17. Comparison between LFA experiment and LFA simulations with various time steps for Pyroceram 9606 sample of: a) 1 mm; b) 3 mm thickness.	32
Figure 18. Geometry file for the GR/50 heat sink (grey) with aluminium spreader (blue) and PCB (yellow).....	35
Figure 19. SEM images taken from the cross section of a 1.47 mm thick GR/50 flame bar.	38
Figure 20. Average values and standard deviation for the thermal conductivity of GR/50.....	40
Figure 21. High aspect ratio fillers (red) in a polymer matrix (white) with a different degree of dispersion: a) ideal; b) good dispersion with presence of agglomerates [104].	41
Figure 22. Average values and standard deviation for the thermal conductivity of GR/70.....	42
Figure 23. Average values and standard deviation for the thermal conductivity of GR/50 _{hv}	44
Figure 24. Flake orientation for GR/50 in the cross section referring to the: a) middle area; b) injection gate-area.	45
Figure 25. Representation of flake orientation in Moldex3D.	45
Figure 26. Profile of the flake orientation in z-direction for the central part of the injection molded bars: a) 1.47 mm thickness; b) 3.2 mm thickness.	46
Figure 27. Shear rate at the end of filling across the central cross-section of: a) GR/50 (1.47 mm); b) GR/70 (1.47 mm); c) GR/50 _{hv} (1.47 mm); d) GR/50 (3.2 mm); e) GR/70 (3.2 mm); f) GR/50 _{hv} (3.2 mm).....	48
Figure 28. Through-thickness velocity distribution in the center of GR/50 flame bars.	48
Figure 29. Through-thickness orientation for the middle and injection zones of the GR/50 1.47 mm bar.....	49
Figure 30. Shear rate at the end of filling across the injection zone cross-section of the GR/50 _{hv} sample of 1.47 mm thickness.	49
Figure 31. Shear stress distribution at end of filling for: a) GR/50 (1.47 mm); b) GR/50 (3.2 mm); c) GR/70 (1.47 mm); d) GR/70 (3.2 mm); e) GR/50 _{hv} (1.47 mm); f) GR/50 _{hv} (3.2 mm).....	50

Figure 32. LFA results for GR/50 samples (TP): a) middle zone of 1.47 mm thick bar; b) injection zone of 1.47 mm thick bar; c) middle zone of 3.2 mm thick bar; d) injection zone of 3.2 mm thick bar.	53
Figure 33. LFA results for GR/50 samples (IP): a) middle zone of 1.47 mm thick bar; b) injection zone of 1.47 mm thick bar; c) middle zone of 3.2 mm thick bar; d) injection zone of 3.2 mm thick bar.	54
Figure 34. LFA results for GR/70 samples (TP): a) middle zone of 1.47 mm thick bar; b) injection zone of 1.47 mm thick bar; c) middle zone of 3.2 mm thick bar; d) injection zone of 3.2 mm thick bar.	55
Figure 35. LFA results for GR/70 samples (IP): a) middle zone of 1.47 mm thick bar; b) injection zone of 1.47 mm thick bar; c) middle zone of 3.2 mm thick bar; d) injection zone of 3.2 mm thick bar.	56
Figure 36. LFA results for GR/50 _{hv} samples (TP): a) middle zone of 1.47 mm thick bar; b) injection zone of 1.47 mm thick bar; c) middle zone of 3.2 mm thick bar; d) injection zone of 3.2 mm thick bar.	57
Figure 37. LFA results for GR/50 _{hv} samples (IP): a) middle zone of 1.47 mm thick bar; b) injection zone of 1.47 mm thick bar; c) middle zone of 3.2 mm thick bar; d) injection zone of 3.2 mm thick bar.	58
Figure 38. Cross section of temperature at 1.25 s calculated by FEA for 3.2 mm thick GR/50 samples: a) isotropic model, TP measurement; b) anisotropic model, TP measurement; c) isotropic model, IP measurement; d) anisotropic model, IP measurement.	59
Figure 39. Steady-state thermal distribution [°C] of heat sink for 5000 lm LED: a) experimental; b) isotropic model ($\kappa=3.74$ W/m°C); c) anisotropic model (0.4 filler anisotropy correction); d) isotropic model ($\kappa=10$ W/m°C); e) anisotropic model (isotropic filler).	61
Figure 40. Steady-state thermal distribution [°C] of heat sink for 3000 lm LED: a) experimental; b) isotropic model ($\kappa=10$ W/m°C); c) anisotropic model (isotropic filler).	62
Figure 41. Steady-state thermal distribution [°C] of heat sink for 2000 lm LED: a) experimental; b) isotropic model ($\kappa=10$ W/m°C); c) anisotropic model (isotropic filler).	63

List of tables

Table 1. Types of fillers and their characteristic dimensions.....	8
Table 2. Comparison of techniques for measuring the thermal conductivity of polymers and polymer composites [38], [56], [57].....	9
Table 3. Popular models for predicting the thermal conductivity of composites.....	16
Table 4. Parameters for the injection molding of the two materials in Series 1.....	23
Table 5. Parameters for the injection molding of GR/50 in Series 2 (GR/50 _{hv}).	25
Table 6. Mechanical properties in Moldex3D material files for GR/50 and GR/70. ..	27
Table 7. Summary of boundary conditions used for the simulation of the through-plane (TP) and in-plane (IP) LFA experiments.....	30
Table 8. Physical, mechanical and thermal properties of used materials.....	36
Table 9. LFA results for GR/50 samples.	39
Table 10. LFA results for GR/70 samples.	41
Table 11. LFA results for GR/50 _{hv} samples.	43
Table 12. Simulation results for the thermal diffusivity and conductivity of GR/50 samples with percentage error compared to experimental results.	54
Table 13. Simulation results for the thermal diffusivity and conductivity of GR/70 samples with percentage of error compared to experimental results.	56
Table 14. Simulation results for the thermal diffusivity and conductivity of GR/50 _{hv} samples with percentage error compared to experimental results.	58
Table 15. Details for the IR camera results.....	63

Introduction

Polymers, a large class of materials, can be defined as molecules constituted of a number of building blocks (monomers), typically connected by covalent bonds. The distinct macromolecular structure gives polymers a unique set of properties, which has made them ubiquitous in everyday life. More recently, attention is focused on the so-called specialty polymers whose performance can be tailored to fit specific application requirements, such as fatigue and wear resistance, dimensional stability, thermal degradation resistance, gas barrier, solvent resistance, electrical properties, biocompatibility, flame retardant properties, corrosion protection, etc. One of the areas of great interest is the field of thermally conductive polymers and polymer composites. The importance of these materials originates from their potential to provide a solution to one of the greatest problems of modern electronics – thermal management. In fact, the small size and high integration of electronic components has greatly enhanced performance at the cost of increasing power density. Dissipation of resulting heat is a critical factor affecting the performance, stability, reliability, service life, as well as the technical possibility for further miniaturization of electronics. The most apparent mechanism for cooling a device is utilizing a high thermal conductivity (κ) material that can efficiently transport heat away from high-power components [1]. In addition to microelectronics, high thermal conductivity materials are an essential part of electric motors, generators and heat exchangers [2] and they find their place in lucrative industrial sectors like network connectivity, automation, electric vehicles and light-emitting diode (LED) lighting.

Conventionally, the materials of choice for such applications have been metals, in particular steel, aluminium and copper with high thermal conductivity values of 16, 237 and 400 W/m°C, respectively [3]. Metals have some disadvantages due to their high weight, cost and sensitivity to corrosive fluids. Polymers offer an alternative for overcoming these limitations while maintaining comparable heat dissipation efficacy. Furthermore, polymeric materials offer the advantages of less energy-intensive production, greater geometric flexibility, ease of fabrication, adaptability in terms of electrical conductivity or insulation, vibration damping and mechanical flexibility which complies to the geometry of adjacent rough surfaces. A common practice for improving the intrinsically low mechanical strength and thermal conductivity of polymers is the use of appropriate fillers. For instance, thermally conductive materials such as graphite, boron nitride and aluminium oxide are widely employed in the industry for producing polymeric compounds for heat transfer applications.

Heat transfer studies the energy transport between material bodies due to a temperature gradient and is of fundamental importance in engineering fields [3]. Heat transfer occurs through three main mechanisms: conduction, convection and radiation. Conduction takes place in solids, liquids and gases through the exchange of energy between molecules or through the motion of free electrons. The amount of heat transferred depends on the geometry, properties of the medium and temperature difference. The ability of a material to transfer heat is given by its thermal conductivity.

Convection occurs only in fluids, where the thermal energy is carried by the macroscopic motion of molecules moving from hotter to colder regions. This phenomenon includes the exchange of heat to the fluid from a solid surface, where the amount of heat is determined by the interface surface area, temperature gradient and convection coefficient (h). The latter is a property of the whole system, not the material. Depending on the origin of fluid motion, convection can be free (density variation due to temperature differences), forced (external force) or mixed (both are present). Thermal radiation is emitted by any material body at any temperature. Radiation energy is transferred by electromagnetic waves and as such it is the only mode that does not require a propagation medium. It is caused by vibration and rotation motion of molecules, atoms and electrons within a substance, which are determined by the material and its temperature.

In a real physical problem, all mechanisms of heat transfer are present to a different extent. Therefore, the combined evaluation of each contribution is imperative to optimizing overall efficiency. While the most obvious consideration for improved heat transfer is using materials with high thermal conductivity, this is not a determining parameter. In fact, the efficiency of the convective exchange on the radiating surface is often overlooked when it comes to its effect on the overall balance. Since the only influencing parameters are part geometry and properties of the surrounding [4], the heat transfer process can be optimized even for less thermally conductive materials. Thermally conductive polymeric compounds are the perfect candidates for this application, due to their capability to be formed into complex shapes.

As a result of the fast advancement of information technology, computer simulations have become a popular tool for predicting and understanding material systems and their behavior. In order to comprehend and quantify any physical phenomenon, including heat transport, it is necessary to use mathematical models. In fact, many physical processes are described by partial differential equations, that can be solved by a computer with the application of an appropriate numerical method. One of the most popular choices is the finite element analysis (FEA), which gives an approximate solution for a continuum problem of complex partial differential equations by discretization. A mesh is created to divide the geometry into small, interconnected pieces called “elements”, where the corner point of each element is known as a “node”. Therefore, the continuous problem with an infinite number of unknowns is reduced to a problem with a finite number of unknowns calculated at the nodal points. Using the nodal values, interpolation functions are defined for each element. To obtain results for the overall system, all individual element equations must be assembled in a matrix describing the behavior for the whole solution region of the problem. After including the boundary conditions, the resulting set of algebraic equations can be solved to obtain the nodal values of the unknown variable (e.g. temperature). Finally, secondary quantities (such as heat fluxes) can be calculated from these results.

Activities of the present thesis were carried out as collaboration between Research and Development (R&D) and Technical Assistance in LATI. The experimental part consisting of injection molding and laser flash analysis (LFA) of

polymeric compounds was performed in the laboratories of the R&D department. Samples for the LFA were obtained from injection molded bars of two different thicknesses. The objective was to investigate the filler orientation effect on the thermal conductivity of the plastic compounds. The work was based on previous research activities in the company which lead to an assumption that the decisive factor for filler orientation, and therefore directional thermal conductivity, is the thickness of the mold cavity, whereas the injection molding parameters showed no significant influence. The main activity in the Technical Assistance department was performing computer simulations of the LFA laboratory measurements. The goal was to compare the calculated thermal conductivities from both methods, in order to evaluate the accuracy of a model for determining the anisotropic thermal conductivity of injection molded compounds created in LATI. Finally, the model was used on a real component in a case study (joint effort with Whitecroft Lighting).

1. Theoretical framework

1.1. Polymer thermal conductivity

Thermal conduction is the irreversible heat flux generated in solids due to the presence of a temperature gradient and it follows Fourier's law:

$$\mathbf{q} = -\kappa \nabla T \quad (1)$$

where \mathbf{q} is the heat flux density (W/m^2), defined as the amount of energy flowing through a unit area per unit time, κ is the thermal conductivity (W/mK) and ∇T is the temperature gradient (K/m). The negative sign is due to the fact that the heat transfer direction is opposite to the increasing temperature direction.

In electrically conductive solids, such as metals, heat can be transferred by charge carriers (electrons and holes). On the other hand, in polymers, which are typically electrically insulating, heat conduction takes place through lattice vibrations (phonons). Phonons have no mass and obey Bose-Einstein statistics. Therefore, the heat current can be calculated by the phonon distribution obtained by solving the Boltzmann equation [5]. For theoretical description of the polymer thermal conductivity, models based on relaxation times and Debye approximations are still widely used, i.e. [6]:

$$\kappa(T) = \frac{1}{3} \sum_i \int C_i(\omega) v_i \Lambda_i(\omega) d\omega \quad (2)$$

where $C_i(\omega)$ is the specific heat capacity (J/kgK) of phonons with branch index i and frequency ω ; v_i is their group velocity (m/s) and $\Lambda_i(\omega)$ is the mean free path.

Polymeric materials have long-chain molecules, with molecular structure ranging from irregular amorphous to highly ordered crystalline. They also contain structural defects, e.g. dangling ends, entanglements, loops, random chain orientation, impurities and voids, that cause phonon scattering responsible for an extremely small κ . Therefore, for most polymers, the thermal conductivity at room temperature is limited to lower values ($0.1 - 0.5 \text{ W/mK}$) [7]. However, they possess many advantages, including light weight, corrosion resistance, ease of manufacturing and low cost. This has motivated researchers to explore new approaches of increasing the thermal conductivity of polymers, broadening their range of applications to areas like microelectronics, heat exchangers, electric motors and generators [2].

Strategies for improving the thermal conductivity of pristine polymers are based on controlling the polymer morphology, e.g. the order of chain alignment. Unlike metals and inorganics, fully crystalline polymers cannot be obtained by typical processing conditions (due to their high molecular weight and polydispersity). Instead, they have a crystalline and an amorphous phase. In the crystalline domains, heat conduction paths follow regular chain conformation and the conductivity is enhanced by coordinated vibrations [8], [9]. Highly oriented chain morphologies obtained by

mechanical stretching, nanoscale templating or electrospinning have been reported [10] to achieve thermal conductivity values as high as 104 W/mK [11]. The chain structure (backbone and side chains) also plays a part in the transport of heat. Introduction of polar groups [12], [13], rigid backbones [14], larger radius of gyration [15], [16] are found to increase the thermal conductivity of polymers. Interestingly enough, higher branching density and branch length can have both positive [17] and negative [18] influence on this property. Finally, inter-chain coupling is considered. In most cases, individual chains in the polymer interact through weak van der Waals forces. If stronger inter-chain interactions are introduced, such as hydrogen bonds [19], covalent bonds in the case of crosslinking [20], or even ionic coupling [21], the thermal conductivity of polymers can be further tuned.

It can be seen that the pristine polymer conductivity depends on many complex factors, which is a reason for large scatter (and even contradictions) in the reported data [2]. In most cases, the thermal conductivity of polymers remains rather limited. For this reason, especially in industrial applications, highly conductive fillers are used to obtain polymer composite materials with desired heat transfer properties.

1.1.1. Thermally conductive fillers: overview

Thermally conductive fillers can significantly enhance the thermal conductivity of polymeric materials. Intuition would suggest that to optimize heat transport in polymers, filler with highest possible thermal conductivity should be added. However, Bigg [22] found that the increase of polymer thermal conductivity becomes insignificant when the filler thermal conductivity is three orders of magnitude higher than that of the pristine polymer. Filler materials can be classified in three groups: metallic, ceramic and carbon-based. Hybrid fillers have also been developed. The type of filler material to be used depends on the end application. For instance, ceramic fillers are employed in cases where electrical insulation is necessary, such as in printed circuit boards. Nano-sized fillers could be used for applications requiring specific performance, like good mechanical strength in thermal interface materials [23], high corrosion resistance in heat exchangers [24] or optical transparency [25]. Variables such as shape, size, aspect ratio, amount, functionalization, dispersion etc. of the conductive fillers have a significant effect on the κ value of polymer composites [2], [9]. Furthermore, polymer composites based on semicrystalline materials (polypropylene, polyamide 6, polyamide 66, liquid crystals) exhibit higher thermal conductivity compared to composites with an amorphous matrix [26] (which is in line with the case of pure polymers).

1.1.1.1. Metallic fillers

Metals can enhance not only the thermal, but also the mechanical properties of polymers, which has a beneficial effect on their handling capability. It is important to note that they also increase the material density, electrical conductivity, corrosion and oxidation, limiting possible applications. Metallic nanoparticles have been reported as more effective for increasing the thermal conductivity compared to their micro-sized

counterparts [27]. Li et al. [28] have investigated epoxy composites with nickel nanoparticles and found that smaller particle size results with higher thermal conductivity due to wider-spread aggregation structures in the polymer matrix. The aggregation effect was also responsible for thermal conductivity higher compared to what the effective medium predicts. In the study of Luyt et al. [29], the addition of 24 vol% copper powder increased the κ value of polyethylene by a factor of two. More recently, research focus has shifted to one-dimensional metal nanowires, which form percolating networks at much lower loading with respect to particulate fillers. For example, copper nanowires were reported for achieving a thermal conductivity of 2.46 W/mK in polyacrylate at a fraction of 0.9 wt% [30]. They also performed better compared to silver nanowires, which was explained by their higher aspect ratio forming a well-connected conducting network. However, silver remains a popular candidate in commercial compounds [23].

1.1.1.2. Ceramic fillers

Ceramic materials have gained attention as thermally conductive fillers for polymeric materials due to their electrical resistivity, high mechanical strength and low coefficient of thermal expansion. They also have lower density compared to metallic fillers. Potential limitations of ceramics as thermally conductive fillers include: higher cost compared to both metallic and carbon materials (due to the obstacles in preparing ceramics compatible with polymer matrices) [31], low thermal conductivity in the through-plane direction for two-dimensional ceramic fillers [32] and sensitivity to hydrolysis [33]. Boron nitride (BN) has been extensively investigated for increasing the thermal conductivity in polymer composite materials. It is suitable for electronic packaging applications due to its excellent temperature resistance and light weight [34]. Leung et al. successfully used spherical BN particles (33.3 vol%) to improve the thermal conductivity of polyvinylidene fluoride by eight times [35]. BN has performed better as a thermally conductive filler in epoxy composites, compared to other ceramic fillers with comparable or higher κ values such as alumina (Al_2O_3), diamond, silicon carbide (SiC), and silicon nitride (Si_3N_4), as demonstrated by Han et al. [36]. Thermal conductivity can be further enhanced if BN is used together with Al_2O_3 short fibers [32]. On the other hand, Lee et al. [37] compared thermal conductivities of ethylene-vinyl acetate composites filled with SiC, zinc oxide (ZnO), or BN, obtaining results of 2.85, 2.26, and 2.08 W/mK, respectively, at a loading of 60 vol%. Studies have also reported that oxide ceramic fillers (except BeO) typically have a lower thermal conductivity [38].

1.1.1.3. Carbon-based fillers

Carbonaceous materials, such as graphite, carbon fiber, graphene and carbon nanotubes (CNTs) have attracted great attention because they improve not only the thermal conductivity, but the mechanical properties of composites as well. They also increase the electrical conductivity, but maintain the advantage of low density and are inert and compatible with polymeric materials [31]. Graphite is an attractive choice for conductive filler, especially in the industry, due to its good thermal conductivity, fair

dispersibility in the polymer matrix, low cost and availability in various shapes and sizes [39], [40]. Zhou et al. [41] have investigated a polyamide 6/polycarbonate (PA6/PC) blend compounded with graphite flakes, and found that thermally conductive paths were formed at graphite content of 30 wt% (17.97 vol%). Thermal conductivity of the composites increased with increasing the filler loading and reached 4.754 w/mK (16.3 times higher compared to the unfilled system) at the maximum loading fraction of 50 wt% (33.83 vol%). Using expanded graphite, an exfoliated form of graphite, offers potential advantages due to its layered structure (20–100 nm layer thickness), where carbon atoms interact strongly on the hexagonal plane, but have weaker interactions in the normal direction. This can be exploited by a combination of synthesis and processing techniques to obtain a very good dispersion of graphite particles in the polymer matrix, while maintaining an extent of connectivity between the flakes which is necessary for effective heat transport [42], [43]. Chen and Ting [40] obtained epoxy composites based on vapor grown carbon fiber with a κ value higher than that of copper (695 W/mK at 56 vol% of filler) and low density of 1.48 g/cm³. More recently discovered allotropes of carbon, graphene and CNTs, have attracted great interest due to their record-breaking thermal conductivity of up to 5000 W/mK [44] and 3500 w/mK [45], respectively. However, these values are not easily translated to high thermal conductivity nanocomposites. Two possible causes for this are: 1) the graphene and CNTs prepared for individual characterization of thermal properties are of much higher quality compared to those used in nanocomposites, and 2) the thermal resistance across the filler/polymer interface [10]. In any case, graphene and CNTs have been successfully utilized to improve the heat transport in polymers [2], [46].

1.1.1.4. Hybrid fillers

Hybrid conductive fillers use a combination of different materials to take advantage of the synergy effect and fine-tune the final properties. Polymer composites with hybrid fillers can have better thermal performance with respect to those with single-type fillers, mainly due to better dispersion and connectivity between the conductive particles. For instance, Pan et al. [47] observed that the through-plane conductivities of polytetrafluoroethylene (PTFE) filled with hexagonal boron nitride (hBN), aluminium nitride (AlN), and hybrid hBN/AlN fillers at 30 vol% were 0.680, 0.723 and 1.04 W/mK, respectively. Similar results have been recorded for using fillers of the same material with different morphologies, e.g. AlN as whiskers and isotropic spheres [48], or the same material with different size particles [49]. Literature reports various combinations of filler materials (CNT/Al₂O₃, silver/graphene, copper/CNT/carbon fiber, etc.) obtained using a number of techniques, such as direct blending, physical adsorption and chemical bonding [9].

1.1.2. Orientation effect

Thermally conductive fillers described in the previous section have a variety of shapes, so it is useful to classify them into one-dimensional (fibers, rods, wires, tubes), two-dimensional (platelet-like) and spherical fillers. There exist also 11 artificially

designed filler shapes [38]. Defining the filler shape is important because it determines the contact type among fillers, which in turn affects the conductivity of the composite. The contact types, listed by increasing magnitude are: point, line and face contact. Spherical particles form point contact, and generally achieve lower, isotropic values for the thermal conductivity. One-dimensional and two-dimensional fillers form line and face contact, respectively; hence they impart higher thermal conductivity and anisotropy to the polymer composites. In order to better demonstrate this effect, fillers can be described by their aspect ratio (Table 1). At the same loading concentration, anisotropic fillers are more effective than spherical ones because phonon transport is facilitated along the greater dimension(s), i.e. along the length l [50]. In one-dimensional fillers, this is typically referred to as the longitudinal direction, and in two-dimensional fillers as the in-plane direction. Formation of longer conduction paths reduces the number of polymer/filler interfaces that tend to decrease the overall thermal conductivity. The formation of conductive paths beyond a certain filler concentration is described by the percolation threshold [51]. Apart from reducing the number of interfaces, aligning the filler particles can improve the macromolecular chain alignment, which in turn increases the κ value of the polymer matrix itself [52]. Therefore, the thermal conductivity of composites depends strongly on the filler orientation and a strategy to maximize the efficiency of heat transfer is orienting fillers in the direction of the heat flow.

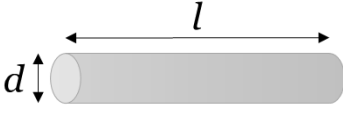
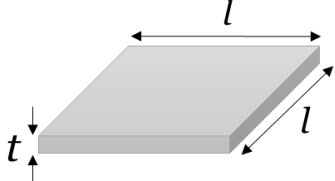
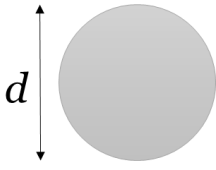
Type of filler	One-dimensional	Two-dimensional	Spherical
Graphical representation			
Aspect ratio	$l/d > 1$	$l/t > 1$	$d/d = 1$

Table 1. Types of fillers and their characteristic dimensions.

Researchers have proposed different methods for increasing the alignment of filler particles in a polymer matrix, such as mechanical stretching, electric and magnetic field. Zhao et al. [53] used hot stretching technology to increase the thermal conductivity of polyoxymethylene/multi-walled carbon nanotube composites for 180% with respect to an isotropic sample. This effect was achieved due to increased crystallinity and orientation of the polymer matrix and increased alignment and orientation of the CNTs. Liu et al. [54] reported that the application of an AC electric field on polydimethylsiloxane with less than 5 wt% clay particles improves the thermal conductivity and decreases the percolation threshold, which in turn allows good thermal and mechanical performance of the composite without compromising the flexibility and transparency of the polymer matrix. Thermally conductive filler particles can be covered with a superparamagnetic material to become magnetically

responsive. Yuan et al. successfully used this for magnetic field alignment of BN platelets in a silicone matrix to increase the thermal conductivity up to 44.5%.

Other effective methods for enhancing microstructural orientation in polymer composites include: doctor blading, vacuum-assisted filtration and injection molding [55]. Injection molding is discussed in detail in Section 1.2.

1.1.3. Methods for measuring thermal conductivity

There exist a number of methods for evaluating thermal conductivity, generally classified as steady-state and transient. The suitable technique for a given material depends on its thermal properties and the medium temperature. Table 2 gives an overview of the different thermal conductivity test methods. Only methods suitable for measuring the thermal conductivity of polymers and their composites are considered.

Type	Method	Temperature range [°C]	Conductivity range [W/m°C]	Uncertainty	Advantages	Disadvantages
Steady-state methods	Guarded hot plate	-200 – 500	< 0.8	2%	High accuracy	Long measurement time, large specimen size, low conductivity materials
	Heat flow meter	-100 – 200	< 10	3%	Simple construction and operation	Measurement uncertainty, relative measurement
	Radial heat flow	20 – 2500	0.02 – 200	2%	Temperature range	Specimen preparation, long measurement time
Transient methods	Laser flash diffusivity	-100 – 3000	> 0.01	3 – 5%	Temperature range, ability to test most solids, liquids and powders, small specimen, speed, accuracy at high temperatures	Expensive, not for insulation materials
	Transient hot wire	20 – 2000	< 25	1 – 10%	Temperature range, speed, accuracy	Limited to low conductivity materials
	Transient plane source	-200 – 900	0.005 – 1800	5%	Speed, accuracy	Very large samples required for highly conductive materials

Table 2. Comparison of techniques for measuring the thermal conductivity of polymers and polymer composites [38], [56], [57].

1.1.3.1. Steady-state methods

Steady-state techniques record the thermal conductivity in a state of thermal equilibrium, meaning that the temperature varies across the sample but is constant with time. These methods use Fourier's law, therefore they are based on measuring a heat flux and a temperature gradient to determine the thermal conductivity. Steady-state implies constant signals, so the analysis is direct and straightforward. Disadvantages are the long time needed to reach required equilibrium and the complex experimental setup. This is necessary for eliminating systematic errors caused by heat losses at the sample surface, thus ensuring accurate results.

Guarded hot plate

The guarded hot plate (GHP) is one of the basic steady-state methods and it is widely used for measuring the thermal conductivity of insulating materials. The apparatus used can be two-specimen or single specimen (Figure 1). In either case, the sample material is placed between two plates with different temperatures. The hot plate is also called a guarded heater, because it is electrically heated and embedded in a metal plate (guard). The metallic guard is employed in order to approach the ideal case where heat flows only in one direction. Its temperature is regulated to match the hot plate using a hot water circulation system. Heat losses from the hot plate are more effectively controlled in the two-specimen apparatus, due to its symmetric arrangement. The cold plate is also typically temperature-controlled by a water system, but at a lower temperature [58]. When the system reaches a steady-state heat flux, the temperature at each side of the sample(s) is recorded. Finally, κ value of the sample can be calculated based on heat flux, thickness, surface area and temperature difference [38]. Therefore, GHP is an absolute technique which does not require any calibration or correction. Its disadvantages are the time needed to reach steady state and relatively large specimen size (to ensure a sufficiently high temperature gradient).

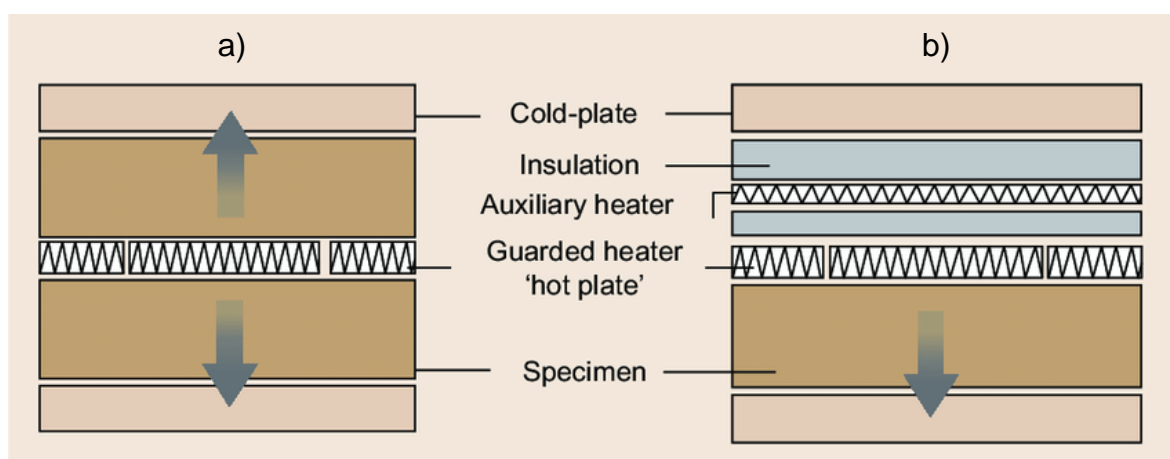


Figure 1. Schematic representation of: a) two-specimen; b) single-specimen GHP apparatus [56].

Heat flow meter

The setup for the heat flow meter (HFM) method is similar to a single-specimen GHP apparatus. In this case, heat flux transducers are used in place of the main heater. The working principle is based on the measurement of a voltage drop through an electrical resistor. The electrical output signal is proportional to the temperature drop across the plate. Therefore, steady-state temperatures, heat flux input and specimen thickness and metered area are the parameters used to calculate the thermal conductivity of the material. Contrary to the GHP, the HFM technique is a relative (comparative) technique, meaning that the heat flux output needs to be calibrated using reference specimens with known parameters. The advantage in this case is that steady-state conditions can be achieved in relatively short times, increasing the productivity output [57]. The disadvantage is the greater probability for measurement errors, due to the presumed linear dependency between heat flow and output signal (which is not always the case). In order to avoid this issue, the thermal conductivity and geometry of the reference sample should be as close as possible to the sample of interest. For thinner samples, thermal radiation is an additional source of errors. However, due to the shorter measurement times and lower apparatus costs, the HFM method is appropriate for monitoring in a series production [59].

Radial heat flow

This method is also known as the pipe method, and it is used for cylinder-shaped samples. A core heating source (tube, rod or wire-shaped) is placed inside the specimen, eliminating radial heat losses. Axial heat losses can also be minimized by using additional end heaters, or taking advantage of a high length-to-diameter sample ratio. The arrangement is surrounded by thermal insulation and then a liquid-cooled heat sink or a water jacket (depending on the temperature range). The thermal conductivity is determined from the cylinder length, heating power, and the temperature difference and radial position of two internal sensors [57].

1.1.3.2. Transient methods

Transient methods record the change of temperature versus time after applying periodic or transient heat at the sample surface. They are typically used to determine the thermal diffusivity (α), which describes the rate of temperature spread through the material. Thermal diffusivity is calculated by knowing the specimen thickness and the time required for reaching a specific temperature rise. The thermal conductivity can then be calculated using the following relation:

$$\kappa = \alpha C_p \rho \quad (3)$$

The main advantage of transient over steady-state methods is the faster measurement; the typical duration is reduced from one hour to few minutes or seconds. The fact that the temperature rise is followed only at one position also makes

the instrument design of transient methods simpler. One disadvantage with respect to the steady-state methods is the more complex data analysis [38].

Laser flash technique

The laser flash analysis (LFA) was developed from studies by Parker et al. [60] in 1961. It is a frequently used technique for determining thermal transport properties of materials due to the compatibility with a wide range of temperatures and thermal conductivities. The LFA working principle is summarized in Figure 2-a. During the measurement, a short laser energy pulse is applied on the lower surface of a specimen with plane parallel geometry, causing a temperature increase that propagates through the sample thickness as a heat wave (Figure 2-b). The resulting temperature rise over time on the opposite side is recorded by an infrared detector and the typical output signal is shown in Figure 3. A mathematical analysis of this temperature-time function allows the determination of the thermal diffusivity. The parameter used for calculating the thermal diffusivity is the half-time ($t_{1/2}$), which corresponds to the time value at half of the maximum signal height (ΔT_{max}). In a one-dimensional, adiabatic case, the following equation is used:

$$\alpha = 0.1388 \frac{d^2}{t_{1/2}} \quad (4)$$

where d represents the sample thickness. From the given relationship it is evident that steeper curve slopes correspond to more thermally conductive samples. The sample itself is usually only a few millimeters thick and the LFA measurement is completed in a matter of milliseconds. Finally, the thermal conductivity can be determined from Equation 3. Since the thermal transport properties of materials are temperature-dependent, LFA instruments are often equipped with a furnace and the measurements can be carried out at different sample temperatures.

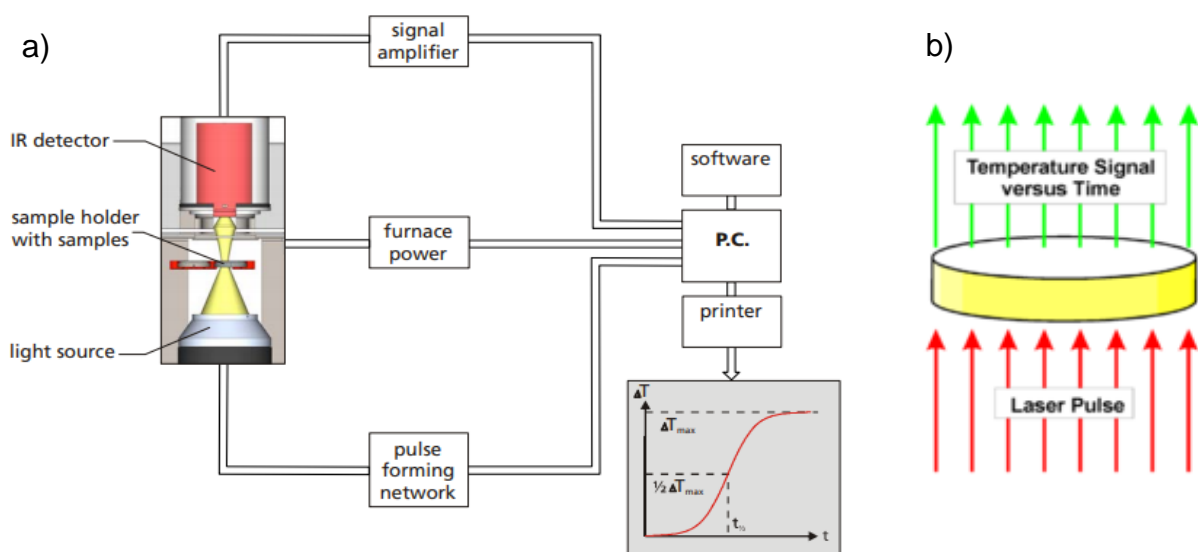


Figure 2. a) Diagram of the laser flash experiment [61]. b) LFA measurement principle [62].

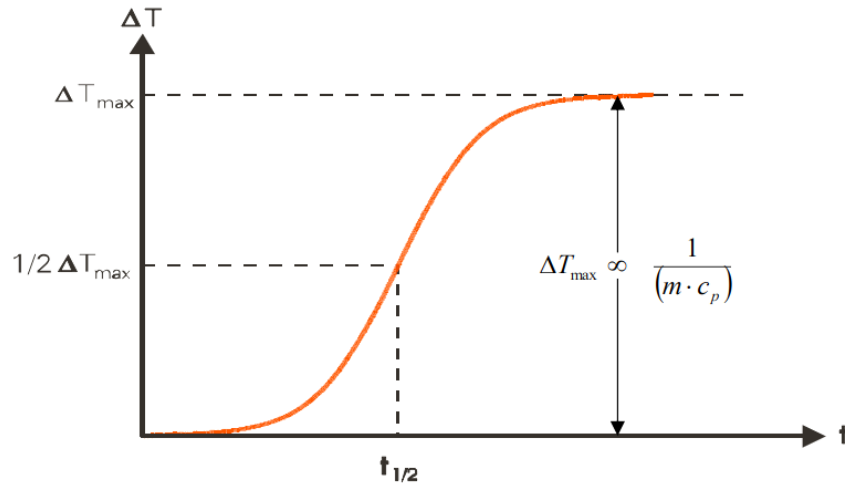


Figure 3. Temperature history curve. The maximum temperature rise (ΔT_{max}) is inversely proportional to the mass (m) and specific heat (C_p) of the specimen [63].

The model used for evaluating the thermal diffusivity using LFA has gone through several improvements since its introduction. Some examples are presented in the following. The original proposal by Parker et al. [60] reduced to a simple algebraic relation considering ideal conditions (homogeneous sample, one-dimensional conduction, pulse input, adiabatic boundary and constant properties):

$$\alpha = \frac{1.37d^2}{\pi^2 t_{1/2}} \quad (5)$$

Later, Parker himself was the first to consider the problem of heat losses; a correction curve was created for decreasing the value of the constant in Equation 5 nonlinearly as the radiation loss increases [64]. Cowan [65] was observing the cooling behavior of the temperature history curve at $5t_{1/2}$ and $10t_{1/2}$ by considering one-dimensional conduction with linearized radiation loss for a finite square pulse. By using this he was able to obtain a dimensionless solution for radiation and convection losses on the top and bottom surfaces. Cape and Lehman [66] assumed two-dimensional conduction and therefore also took into account the heat exchange at the circumference of the specimen. Their model considers radiation losses and the finite pulse-time effect. The latter applies to cases where the laser pulse width is comparable to the characteristic thermal diffusion time, so the temperature increase of the specimen is expected to be slowed down. Since this approach maintains higher order terms, the solution is nonlinear and more accurate at high temperatures. Heckman [67], similarly to Cowan, generated correction data for heat loss from the front and rear faces, but additionally reported dimensionless terms for the heating as well as the cooling curve. He also considered finite-pulse effects. Clark and Taylor [68] developed a correction factor K_R by evaluating the times to reach 25% and 75% of the maximum temperature change ($t_{0.25}$ and $t_{0.75}$, respectively):

$$K_R = -0.3461467 + 0.361578 \left(\frac{t_{0.75}}{t_{0.25}} \right) - 0.06520543 \left(\frac{t_{0.75}}{t_{0.25}} \right)^2 \quad (6)$$

The corrected value for the thermal diffusivity ($\alpha_{corrected}$) using this factor is:

$$\alpha_{corrected} = \frac{\alpha K_R}{0.13885} \quad (7)$$

Additionally, several modifications for the laser flash method have been developed, e.g. determination of the specific heat capacity. This is performed by comparing the maximum temperature change of the sample with the maximum temperature change of a reference sample. Both materials are measured under the same conditions and in order to increase the accuracy, their absorptivity and emissivity should be equal (apply same coating) and the absolute heat capacity (product of C_p and m) should be similar. The heat capacity of the sample of interest is calculated using the following relationship [69]:

$$C_{p,sample} = \frac{C_{p,reference} \cdot \Delta T_{reference} \cdot m_{reference}}{\Delta T_{sample} \cdot m_{sample}} \quad (8)$$

Due to its advantages, the laser flash method is becoming increasingly important in industrial applications. Analyses using the laser flash method generally require significantly less time compared to the GHP or the HFM. Sample preparation is relatively simple and while single-piece solid samples are the most straightforward, this technique is also compatible with powder, liquid, layered and porous materials. LFA follows only the relative temperature change as a function of time, and therefore the measurement of absolute temperature or heat flow is not necessary. This allows measurement uncertainties of 3 – 5% even at elevated temperatures.

Transient hot wire

The transient hot wire (THW) can be considered as an adaptation of the steady-state radial heat flow method. The material is heated by a hot wire (linear heat source) embedded between two homogeneous solid samples with the same size. Sample preparation should be performed carefully, in order to achieve sufficiently low thermal contact resistance with the wire. This disadvantage can be avoided by using a thin metal foil strip in place of the wire, resulting in an increasingly popular variation called the “hot strip method”. The hot wire simultaneously plays the role of heater and temperature sensor. It is heated by application of a constant electrical current and therefore it is considered to have a constant output. By knowing the power input, the thermal conductivity is determined from rate of the linear temperature increase, while the thermal diffusivity can be found as the intercept. For eliminating the effect of interference from the large-diameter power supply leads attached to the ends of the hot wire, two different-length wires are used in a differential mode. This technique is more convenient for use with foams, fluids, and melted plastics, because in this case the heating wire can be simply immersed in the specimen. Other variations of the THW are the parallel and cross-wire methods [56].

Transient plane source

Transient plane source (also known as hot-disk) is a recent modification of the previously mentioned hot strip technique. It uses a double spiral-shaped sensor made of nickel with a thin polymeric coating that provides electrical insulation and physical protection from the environment. The shape of the sensor allows the current to travel between the two ends. Similarly to the hot wire and hot strip methods, the sensor also acts as a heat source. It is heated by applying an electrical current pulse during the measurement. Generated heat dissipates on either side throughout the specimen. Thermal diffusivity and conductivity can be determined by recording the increase in resistance as a function of time [57]. The main advantage of the transient plane source technique is the large flexibility regarding specimen shape and size. Samples can be as small as 2 mm and there is no limitation for the maximum sample size.

1.1.4. Mathematical modelling of thermal conductivity in polymer composites

There exist a number of factors that influence the heat transfer behavior of polymer composites. Filler characteristics, including thermal conductivity, aspect ratio, shape, orientation, modulus, and loading concentrations have been extensively studied by researchers [26]. Some of them were already discussed in Section 1.1.1. Modelling of the thermal transport in polymer composites helps not only to better understand the effect of different parameters, but also predict the material behavior. This is especially valuable in cases when conducting an experiment is not feasible due to high costs or environmental surrounding [70]. Typically, the models refer to the effective thermal conductivity (κ_{eff}), i.e. the thermal conductivity of the composite after all influencing factors have been taken into consideration. Each model may be applicable to only one or a number of composites. Modelling methods can be classified into two categories: theoretical and simulation models. The former is related to the mechanisms of heat transfer, while the latter describes the features of microstructures.

1.1.4.1. Theoretical models for composites

Various reports in literature are focused on models for predicting the thermal conductivity of polymer composites based on simplifying assumptions (no changes in the matrix due to the presence of the filler, perfect filler alignment, good bonding between matrix and filler, no agglomerations or interactions between filler particles) [71]. The most basic theoretical models are:

- Standard mixture rule [72]

$$\kappa_{eff} = (1 - \phi) \cdot \kappa_m + \phi \cdot \kappa_f \quad (9)$$

- Inverse mixture rule [72]

$$\frac{1}{\kappa_{eff}} = \frac{1 - \phi}{\kappa_m} + \frac{\phi}{\kappa_f} \quad (10)$$

– Geometric mixture rule [73]

$$\kappa_{eff} = \kappa_m^{1-\phi} \cdot \kappa_f^\phi \quad (11)$$

where κ_m and κ_f are the thermal conductivities of the polymer matrix and thermally conductive filler and ϕ is the filler volume fraction. Equation 9 is known as the parallel model and, like Equation 11, it is used to estimate the thermal conductivity in the filler direction for unidirectional composites with continuous fibers. The series model (Equation 10) predicts thermal conductivity in the direction perpendicular to the fillers. Other well-known models are summarized in Table 3. Based on dispersed particles into a polymer matrix, the Maxwell [74] model is often utilized for composites with a low content of randomly distributed and non-overlapping homogeneous spheres. The model of Russell [75] was developed based on the assumption that the thermally conductive filler particles are dispersed, isolate cubes in the polymer matrix. Bruggeman [76] considered diluted suspensions of spherical particles in a continuous matrix. For fiber- or disc-shaped particles, the Halpin-Tsai [77] model takes into account the filler anisotropy. Shape, orientation and packing of the filler can be included by the modification of Lewis and Nielsen [78].

Model	Equation
Maxwell	$\kappa_{eff} = \kappa_m \frac{2\kappa_m + \kappa_f + 2\phi(\kappa_f - \kappa_m)}{2\kappa_m + \kappa_f - \phi(\kappa_f - \kappa_m)} \quad (12)$
Russell	$\kappa_{eff} = \kappa_m \left[\frac{\phi^{2/3} + \frac{\kappa_m}{\kappa_f} (1 - \phi^{2/3})}{\phi^{2/3} - \phi + \frac{\kappa_m}{\kappa_f} (1 + \phi - \phi^2)} \right] \quad (13)$
Bruggeman	$1 - \phi = \left[\frac{\kappa_f - \kappa_{eff}}{\kappa_f - \kappa_m} \right] \left(\frac{\kappa_m}{\kappa_{eff}} \right)^{1/3} \quad (14)$
Halpin-Tsai	$\kappa_{eff} = \kappa_m \left(\frac{1 + \xi\eta\phi}{1 - \eta\phi} \right) \quad (15)$ with $\eta = \frac{\frac{\kappa_f}{\kappa_m} - 1}{\frac{\kappa_f}{\kappa_m} + \xi}$ and $\xi = \sqrt{3} \ln \left(\frac{a}{b} \right)$; a = particle width; b = particle thickness
Lewis-Nielsen	$\kappa_{eff} = \kappa_m \left[\frac{1 + A \cdot B \cdot \phi}{1 + B \cdot \phi \cdot \psi} \right] \quad (16)$ with $A = k_E - 1$, $B = \frac{\frac{\kappa_f}{\kappa_m} - 1}{\frac{\kappa_f}{\kappa_m} + A}$, and $\psi = 1 + \frac{1 - \phi_m}{\phi_m^2} \phi$; k_E = Einstein coefficient; ϕ_m = maximum packing filler fraction

Table 3. Popular models for predicting the thermal conductivity of composites.

Furthermore, more extensive models have been developed to recognize complex shape particles, folded and crooked particles, hybrid fillers, aggregation structures, connectivity and porosity [79]. For example, the contact between filler

particles produces contact thermal resistance and heat transfer pathways which have a significant effect on κ_{eff} . Zhou et al. [80] have taken this into consideration for modelling the in-plane thermal conductivity of a polymer composite with a very high content of graphite flakes. By observing the microstructure of a tape-casted composite sheet, the authors found high orientation and formation of conductive networks for the graphite. Therefore, the assumption is that the heat flow is transported only through the thermally conductive filler network. The model is based on simplifying the composite geometry into two different parallel layers of random particles and oriented network. The effective thermal conductivity is given by:

$$\kappa_{eff} = \kappa_o \frac{\rho f_m}{\rho_o} + \kappa_r \frac{\rho(1 - f_m)}{\rho_r} \quad (17)$$

where the indices o and r refer to the oriented and random layer, while f_m is the mass fraction of oriented flakes and it is a representation of the degree of orientation. Zhang et al. [81] suggested a model for prediction of the thermal conductivity of filled polymer composites based on percolation theory. The effective thermal conductivity is calculated as:

$$\kappa_{eff} = \kappa_f \left(\frac{\kappa_c}{\kappa_f} \right)^{(1-\phi/1-\phi_c)^n} \quad (18)$$

where κ_c is the thermal composite thermal conductivity when $\phi = \phi_c$, ϕ_c is the percolation threshold and n is a percolation exponent determined by filler size, shape and distribution in the matrix.

1.1.4.2. Simulation models of composites

The simulation models for bulk composites can be considered at the microscale, mesoscale or macroscale. Authors have also reported multiscale models that combine varying time and length scales [79]. Simulation of the thermal conductivity of composite materials at the microscopic point of view is most often performed by utilizing non-equilibrium molecular dynamics (NEMD). This method allows working with arbitrary shapes and structures without any simplifying assumptions and can also give a detailed description of the vibrational motion of phonons. However, due to the complex computations long calculation times are needed. As an alternative, the equilibrium molecular (EMD) method is also available. Wang et. al [82] applied NEMD for calculating the thermal conductivity of functionalized graphene and graphene/epoxy nanocomposites. It was reported that κ_{eff} of the composite improved by adding functional graphene, despite its lower intrinsic thermal conductivity compared to raw graphene. Evaluation of the phonon spectrum revealed that functional graphene can reduce the phonon mismatch, therefore improving the thermal transport at the graphene/epoxy interface. Most commonly used techniques for thermal simulations at mesoscopic level are the dissipative particle dynamics (DPD), lattice Boltzmann method (LBM) and off-lattice Monte Carlo. LBM is

widely used to implement complex boundary conditions and various particle-particle interactions. A two-step numerical LBM numerical model was developed by Zhou et al. [83]. The composite microstructure is first assembled by considering a random particle distribution, after which the heat flow through the microstructure is analyzed according to the LBM. This model has shown good consistency with experimental results for different composites [79]. The finite element method (FEM) and finite difference method (FDM) are the most well-known and widely used when it comes to computer simulations at the macro scale. Fang et al. [84] compared experimental and simulation results for the LFA and HFM techniques for determining the in-plane thermal conductivity of unidirectional carbon fiber/polymer composites. They found that in-plane orientation angle of the fibers (θ) significantly affects the apparent thermal conductivity. FEM results suggested that there exists a change in process of heat transfer from a continuous to a zig-zag path when the radius-to-thickness ratio of the carbon fibers is lower than $\tan\theta$. This fact can be exploited to optimize thermal performance of fibers in laminate composites.

1.2. Injection molding

Injection molding is one of the most important polymer processing methods for production of plastic and plastic composite parts. It is one of the few manufacturing processes able to produce near net shape components. Polymeric compounds containing filler particles can be injection molded into complex shape with the standard machines used for base plastics. A typical reciprocating screw injection molding machine consists of an injection unit, a clamping unit and a mold unit (Figure 4). As the name implies, the screw can be moved horizontally (reciprocated) to complete the injection, or rotated to act as a melt pump when moving the melt forward. The role of the injection unit is to plasticize (melt) the polymer feed granules, supply homogeneous melt to the nozzle, and finally inject the melt into the closed mold. The clamping unit maintains the moving half of the mold clamped shut for the duration of the high-pressure injection stage. The mold unit contains the cavity into which the polymer melt is injected and cooled to form the part shape. The mold unit comprises a fixed (“cavity”) and a moving (“core”) half [85].

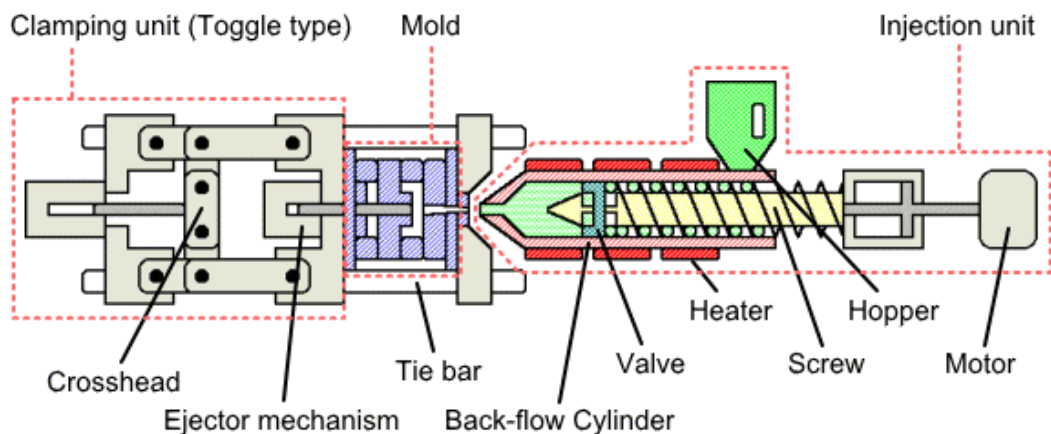


Figure 4. Schematic of an injection molding machine [86].

The material in granular form is fed into the machine through the hopper. The polymer is melted within the barrel through a heater and through the shear heating generated within the melt. During this stage, the melt is accumulated in front of the screw, pushing it back against an adjustable backpressure until the required melt volume (shot size) is achieved. The machine is now ready for injection, where the screw pushes forward in order to force the melted polymer through a runner system into the empty, relatively cold cavity of the closed mold. To compensate for shrinkages caused by cooling of the melt inside the mold, the melt in front of the screw is held under pressure for forcing more material into the cavity. When the injection gate solidifies no additional material can be supplied, therefore the product cools down further with no compensation for shrinkage. The temperature of the mold is kept between room temperature and the glass transition (amorphous polymers) or melting temperature (semi-crystalline polymers). This is typically regulated through a water circulation system. After the system has cooled to a state of sufficient rigidity, the mold opens and the product is ejected.

Injection molding is a cyclical process, with cycle times ranging from 10 to 100s (controlled by the cooling stage). It offers many advantages, such as close tolerances on small intricate parts, little post-production processing required, possibility for waste-reduction by regrinding and reusing the scrap material, possibility for full automation. Injection molding is capable of producing high volumes of filled polymer components for industries ranging from aerospace to toys and hobbies. However, due to its intrinsic complexity, a good understanding of the process is necessary to obtain high quality of the molded products and to avoid defects [87].

1.2.1. Filler orientation in injection molded composites

For beginning to understand the principles of orientation during the injection molding, it is important to highlight the fundamental flow conditions in this complex process. The three main types of flow that influence filler orientation are: in-plane shear flow, in-plane tensile or compressive flow and out-of-plane fountain flow.

In-plane shear occurs in uniform cross-section channels with a pressure gradient along the length and it is the most commonly seen type of flow. In the simplest case of a Newtonian fluid under isothermal conditions the velocity distribution has a parabolic shape, which causes a linear variation of the shear strain going from its maximum value at the walls to zero at the center of the channel (Figure 5-a). However, polymer melts under typical injection molding conditions are non-Newtonian (shear-thinning) and non-isothermal fluids. The non-Newtonian profiles deviate from the Newtonian case as shown in Figure 5-a; velocity has a flatter distribution and the shear strain peak at the walls increases with a wider low shear region in the center of the channel. The non-isothermal behavior refers to the through-thickness temperature gradient caused by melt freezing on the cavity walls. Viscosity increases in the low-temperature regions near the wall, resulting with a reduction in the velocity. This, in turn, shifts the shear rate peak towards the channel core (Figure 5-b).

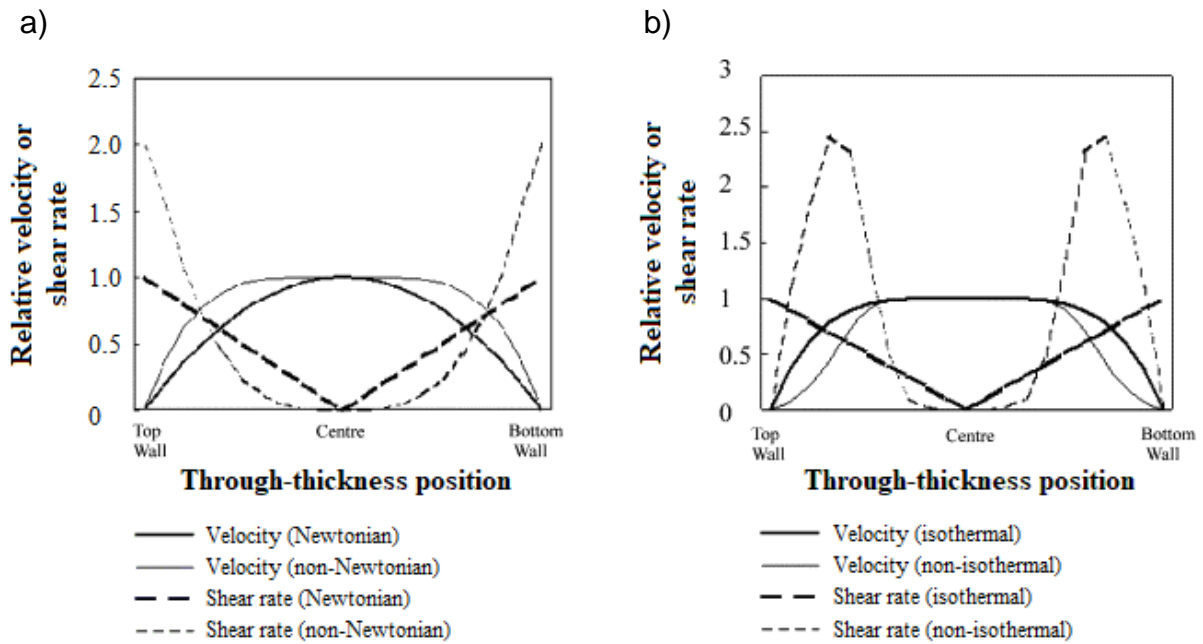


Figure 5. Comparison between the through-thickness velocity and shear rate distributions for: a) Newtonian and non-Newtonian fluids; b) isothermal and non-isothermal conditions for a non-Newtonian fluid (adapted from [85]).

In-plane tensile and compressive flow occur in the presence of convergent and divergent channels, respectively. When passing through a convergent channel, the polymer melt elements undergo a stretching force (in-plane tensile flow) causing fillers to orient along the flow direction. On the other hand, divergent channels cause compression in the flow direction (in-plane compressive flow), aligning fillers perpendicularly to the flow direction. This effect of flow channel geometry is depicted in Figure 6.

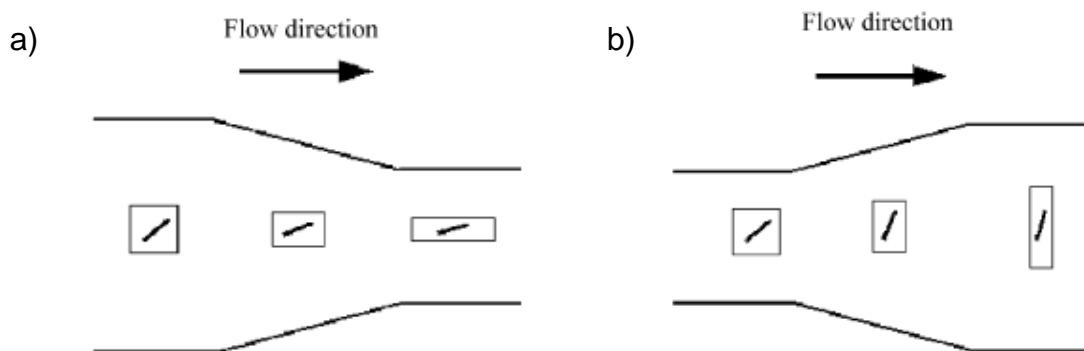


Figure 6. Filler reorientation with polymer melt passing through: a) a convergent channel; b) a divergent channel [85].

Fountain flow can be found at the melt front and it is a result of the through-thickness gradient of velocity and conservation of mass. The higher velocity of the polymer melt along the longitudinal axis results with spraying out of the core material at the flow front. Upon contact of this material with the mold cavity walls, it quickly solidifies into a frozen layer due to the relatively large temperature difference

(Figure 7). Figure 7 also depicts the stretching and rotation of melt elements subjected to the fountain flow. This complex phenomenon produces a surface layer with a random-in-plane filler orientation, whose relative thickness is much smaller with respect to the core region and the high-shear layer in vicinity of the wall.

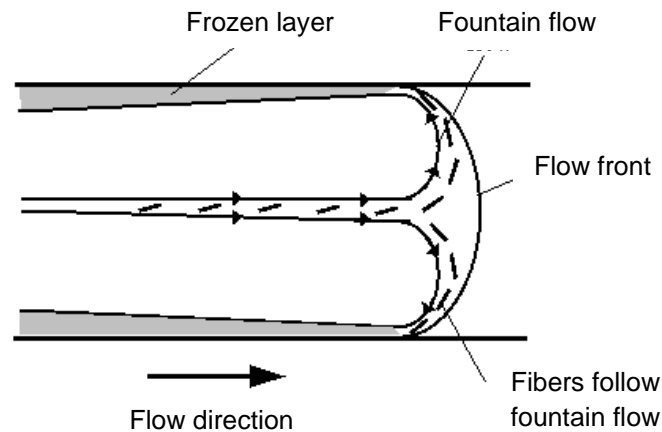


Figure 7. Diagram of the fountain flow present at the melt front [85].

All three previously described types of flow superimpose in a complex manner during the injection molding process to result with a specific through-thickness orientation distribution. The filler orientation varies throughout the part and it is influenced by geometry, processing conditions and melt rheology. The typical filler orientation profile is a three layer skin-core-skin structure shown in Figure 8. The outer layers show strong alignment in the flow direction due to the elongation forces at the melt front developed during fountain flow, as well as due to the shear flow after the front has passed [88]. The core layer tends to have a more random orientation due to slower cooling rate and lower shearing. Studies have also reported a completely transversal filler orientation along the central longitudinal axis of the channel [85], [89]. Alignment in the core layer is further influenced by the mold geometry and relative occurrence of convergent and divergent channels. Furthermore, the orientation in each layer and its relative thickness does depend on the existing conditions. As previously mentioned, an additional thin outer layer is formed due to fountain flow, but it is often disregarded as it only has a marginal effect on part properties [85].

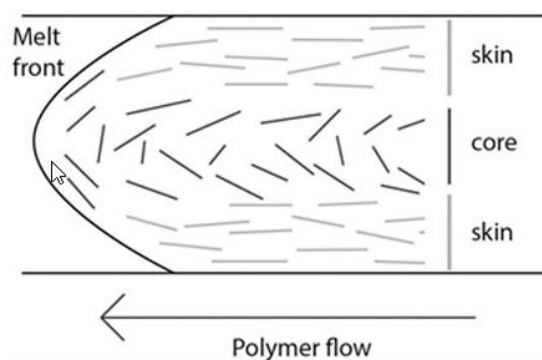


Figure 8. Skin-core orientation of fillers in injection molded polymeric compounds (exaggerated) [90].

2. Materials and methods

For the research purposes of this thesis, two proprietary materials were selected. Both materials are compounds with a polyamide 6 (PA6) polymer base and different content of expanded graphite as filler. A single lot was selected for each of the materials, and their graphite content is 50 wt% and 70 wt% (hereafter referred to as GR/50 and GR/70, respectively).

2.1. Material characterization

Characterization of the physical, mechanical and thermal properties of the materials was done using various techniques. The density was measured via immersion method (ISO 1183). Young modulus and ultimate tensile strength were determined by tensile test (Galdabini Quasar 25) following the ISO 527 standard. Material toughness was evaluated by Charpy impact test (ISO 179-1) for notched and unnotched specimens using the Instron CEAST 9050 impact pendulum. Specific heat capacity for 25, 50 and 75°C was recorded using a TA Instruments Q1000 DSC machine, according to the ASTM E2716 standard. Scanning electron microscopy (SEM) images of selected samples were obtained with a Zeiss EVO40 microscope operated at 20kV.

2.2. Injection molding

The raw material was in form of pellets of the previously described compounds (Figure 9). PA6 is known to have high water absorption, so to avoid hydrolysis during the injection molding (which leads to degradation of properties), the pellets were pre-dried in an oven (80-100°C) for a minimum of 2 hours. The injection molding process was carried out on laboratory scale, using the Negri Bossi CANBIO V40-150 machine with 28 mm screw diameter. The materials were molded into parts of various shape and size according to the characterization techniques to be used. In the following, only the injection molding of LFA samples is described, being the one of interest for the aim of the thesis.

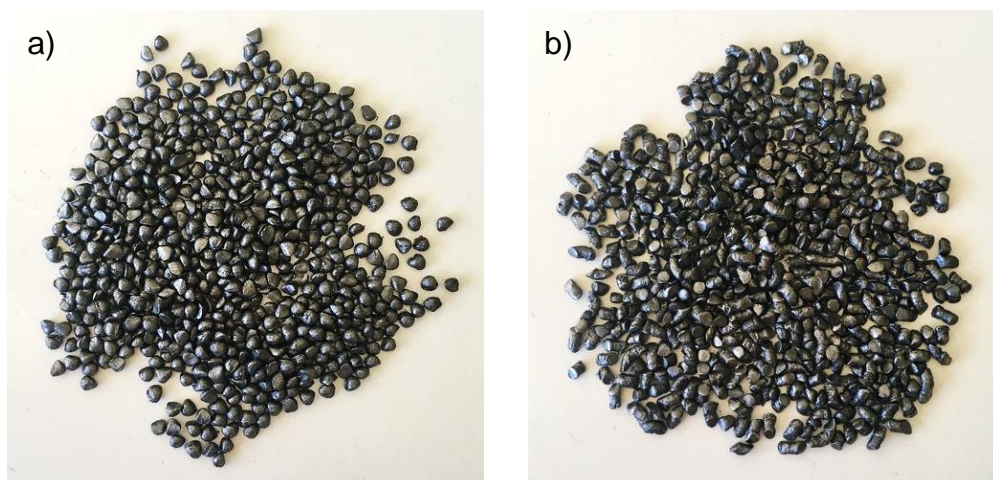


Figure 9. Pellets used for injection molding: a) GR/50; b) GR/70 compound.

For the purpose of the laser flash study, the materials were injection molded into standardized UL 94 “flame bar” specimens of two different thicknesses: 1.47 and 3.2 mm. The remaining two dimensions of the bars are 125 and 12.7 mm. The injection molding was carried out in two series as explained below.

2.2.1. Series 1

The goal of the first series was to obtain different flake orientation, and therefore different directional thermal conductivity for the samples of 1.47 and 3.2 mm thickness. This was based on previous results obtained in the company for a large amount of different compounds, where the specimens of smaller thickness displayed higher in-plane thermal conductivity due to the higher shear rate orienting the flakes along the longitudinal direction of the bars. In fact, the mold cavity thickness was a determining factor for the directional thermal conductivity, whereas the injection molding parameters were not found to have a significant effect. The injection molding parameters used for obtaining Series 1 samples are summarized in Table 4 below. Note that the table does not list the parameters kept constant for all runs, which are: melt temperature (260°C), mold temperature (80°C), maximum filling pressure (140 bar) and cooling time (22 s).

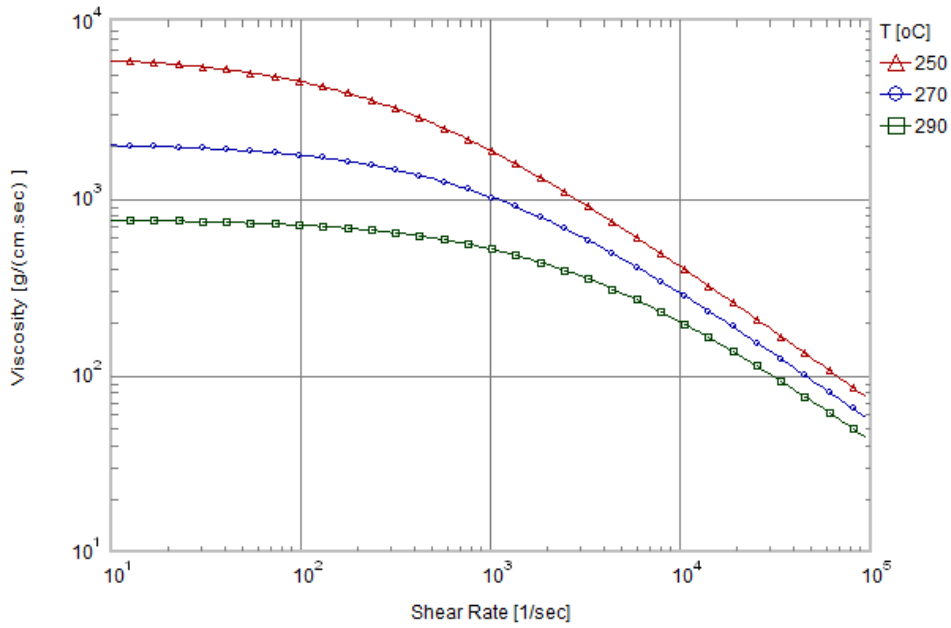
Material	Sample thickness [mm]	Ram position [mm]	VP switch-over by ram position [mm]	Injection velocity [%]	Packing pressure [bar]	Packing time [s]
GR/50	1.47	23	10	20	50	8
	3.20	33	12	20	40	8
GR/70	1.47	20	6	100	65	12
	3.20	33	12	45	50	10

Table 4. Parameters for the injection molding of the two materials in Series 1.

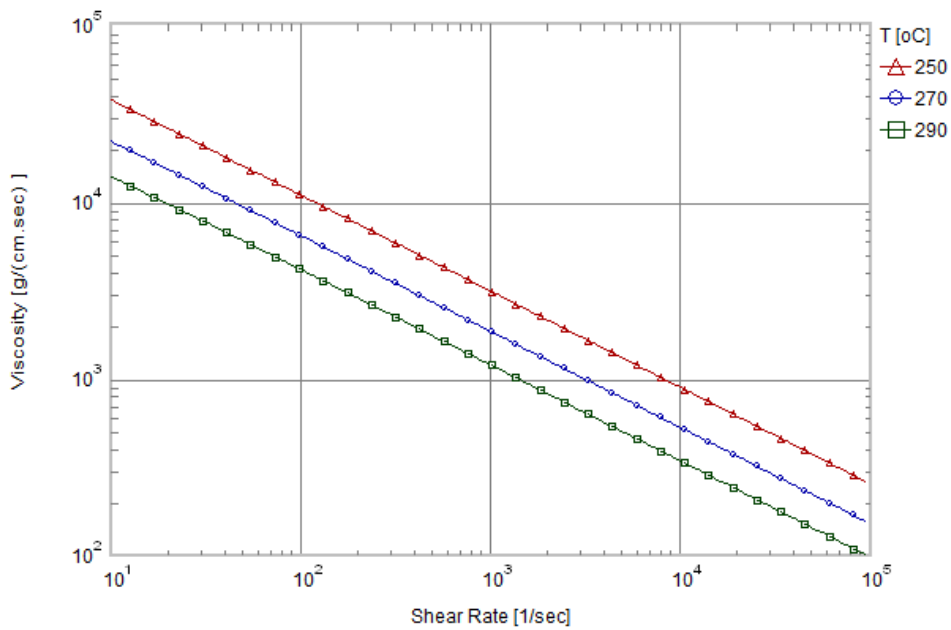
2.2.2. Series 2

After acquiring LFA results for the first series, it was found that in the case of GR/50 there are contradictions with respect to the previous in-company investigations. This is described in more detail in Section 3.2. For enhancing the flake orientation, a very rough approximation was made to increase the shear rate in GR/50 in order to match the shear rate in GR/70. Comparing the data in Figure 10 for the appropriate temperature (260°C) and range of shear rates ($10^2 - 10^3$ 1/s), the viscosity of the GR/70 material is roughly double the viscosity of the GR/50 material. Considering also that the shear rate ($\dot{\gamma}$) is inversely proportional to the viscosity (η) and linearly proportional to the velocity (v):

$$\dot{\gamma} \propto \frac{1}{\eta} \propto v \quad (19)$$



a)



b)

Figure 10. Moldex3D material database viscosity curves for: a) GR/50; b) GR/70.

the desired shear rate for GR/50 was attempted to achieve by employing injection velocity two times higher than the injection velocity for GR/70 in the first series. However, since the GR/70 sample of 1.47 mm was obtained using the maximum velocity of 100%, this value remained unchanged for GR/50 in the second series. The parameters listed as constant for all runs in Series 1 also apply to Series 2, while the rest are summarized in Table 5. Samples obtained in this series are named GR/50_{hv} (hv = high velocity).

Material	Sample thickness [mm]	Ram position [mm]	VP switch-over by ram position [mm]	Injection velocity [%]	Packing pressure [bar]	Packing time [s]
GR/50 _{hv}	1.47	23	10	100	50	8
	3.20	33	12	90	40	8

Table 5. Parameters for the injection molding of GR/50 in Series 2 (GR/50_{hv}).

2.3. Laser flash analysis (LFA)

LFA specimens were made by cutting off pieces from the injection molded bars using a Nebes TM101 PLUS band saw machine. More specifically, one piece was obtained from the central part of the bars (high flake orientation in the longitudinal direction) and another from the bar section near the injection gate (where flakes tend to orient in a more random manner). Measurements of the thermal diffusivity were performed for both the through-plane (TP) and in-plane (IP) direction, which requires slightly different sample preparation (Figure 11). The former is done by simply cutting off a square piece (12.7 mm side) from the injection molded bars (Figure 11-a). For the latter, multiple bars are held together and cut into single strips of 12.7 mm length (Figure 11-b) which are then turned by 90° and placed into the sample support. Both sample types together with the respective holders are presented in Figure 12. As final step of the preparation, both sides of the specimens were coated with a graphite spray (Kontakt Chemie Graphit 33). This is standard LFA practice to enhance the absorption of laser energy, as well as the emission of IR radiation to the detector.

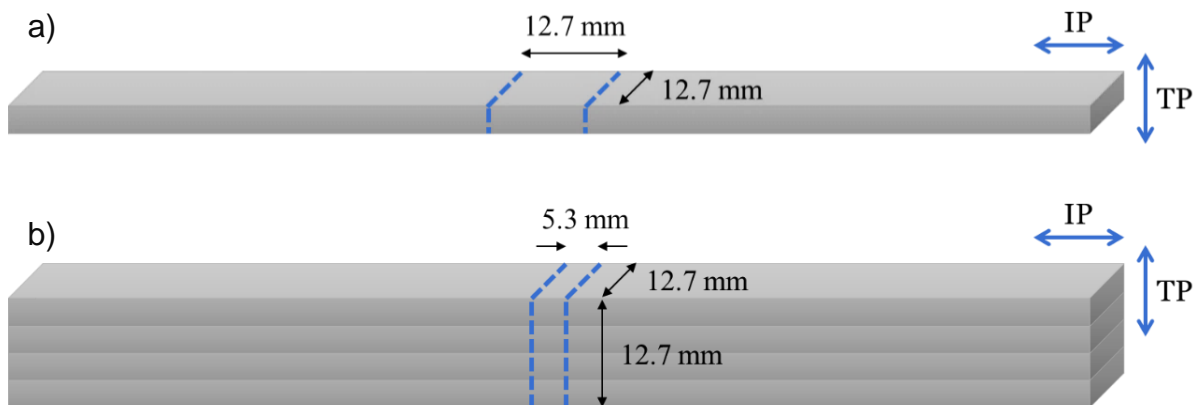


Figure 11. Cutting injection molded flame bars to obtain: a) through-plane; b) in-plane thermal conductivity LFA samples. The bar thickness is as previously defined (1.47 or 3.2 mm).

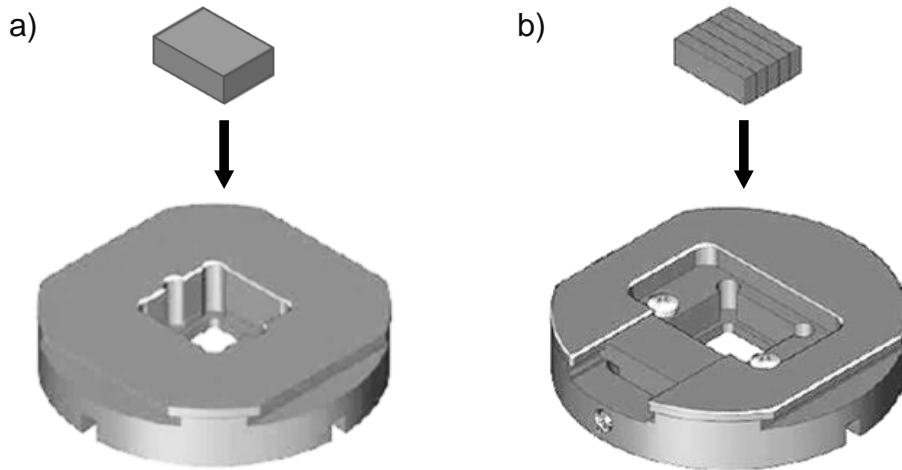


Figure 12. Schematic representation of: a) TP; b) IP thermal diffusivity samples and sample holders (adapted from [61]).

LFA investigations were carried out using a Netzsch LFA 467 HyperFlash® apparatus, which uses a xenon lamp as the flash source. The xenon lamp has a maximum energy of 10 J/pulse that can be varied according to the thickness and heat capacity of the sample. This is done using the instrument software, where the flash power is controlled through the lamp voltage and pulse width. The parameters that were used are those typically suggested for the given range of thermal conductivity and thickness of specimens. Therefore, 230 V lamp voltage and 0.3 ms pulse width was selected for TP conductivity measurement of the 1.47 mm thickness samples, while 260 V lamp voltage and 1 ms pulse width was used in all other cases. For each specimen, the obtained thermal diffusivity from a single measurement is an average over three laser shots applied over a span of few minutes. To investigate the reproducibility of the analysis, three replicate specimens were tested with respect to each material, sample thickness and area of interest. All results were recorded for room temperature (25°C). The instrument software used the Cowan correction model [65] for calculation of the thermal diffusivity.

2.4. Finite element analysis (FEA)

2.4.1. Injection molding simulation

Moldex3D R17 was used as simulation software for the injection molding process. The geometry of the injection molded bars was designed using HyperWorks 2020 and imported into Moldex3D. Meshing the CAD model, designing the runner system and mold were all performed using the Moldex3D module. The mesh size was adjusted so that there is a sufficiently high number of elements in the parts of interest (middle and injection), especially across the bar thickness. Figure 13 depicts the part geometries along with the gate, runner and melt entrance point. Marked in grey are the sections for obtaining LFA samples.

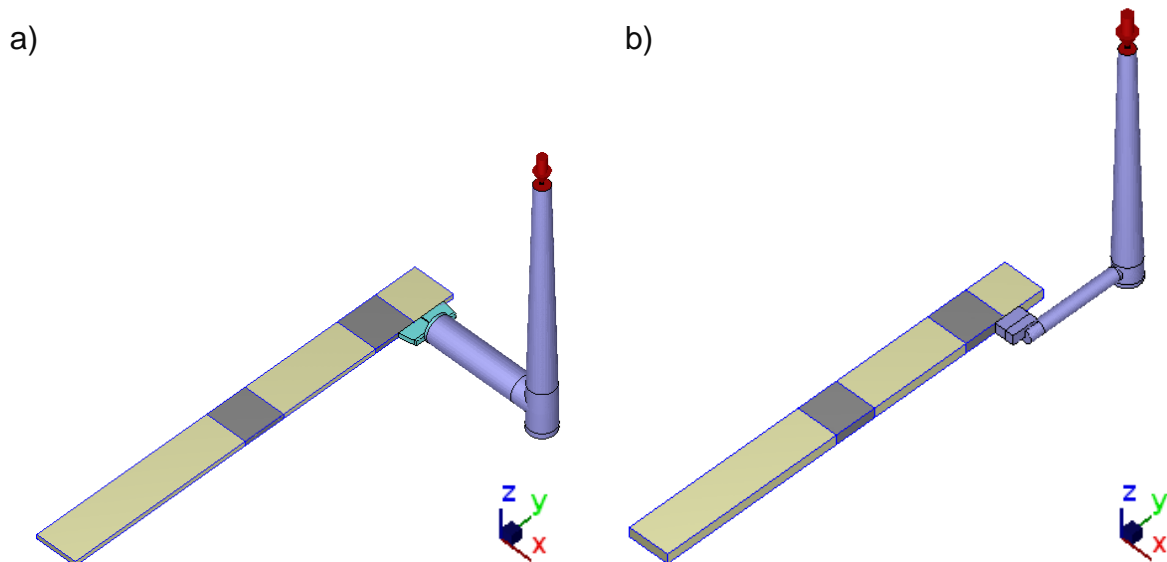


Figure 13. Geometry and runner system for flame bar of: a) 1.47 mm; b) 3.2 mm thickness.

Experimental injection molding parameters were translated into Moldex3D by first creating a custom injection machine profile for the Negri Bossi CANBIO V40-150. By doing so, the software allows input of the exact parameters described in Section 2.2. Material files in Moldex3D contain data that is crucial for good simulation of the complex polymer behavior during the injection molding cycle. For the materials used in this study, the files were available in the Moldex3D bank. Their viscosity is described by the Cross-WLF model [91] and viscosity-shear rate curves for both materials are those shown in Figure 10. In order to obtain results for the flake orientation, the material files were modified to include the mechanical properties of matrix and filler (Table 6). In Moldex3D, filler flakes are modelled as circles with adjustable thickness/diameter ratio (in this case 0.1). All injection molding simulations were carried out for the filling stage, because it is the only one the software considers for determining the final flake orientation.

Material		GR/50 composite	GR/70 composite
Polymer	Density ρ [g/cm ³]	1.13	1.13
	Poisson's ratio [-]	0.4	0.4
	Modulus E [GPa]	3.1	3.1
	Coefficient of linear thermal expansion α [1/K]	$8.5 \cdot 10^{-5}$	$6.5 \cdot 10^{-5}$
Flake	Weight percentage [%]	50	70
	Density ρ [g/cm ³]	2.25	2.25
	Poisson's ratio [-]	0.27	0.27
	Modulus E [GPa]	795	1500
	Coefficient of linear thermal expansion α [1/K]	$3 \cdot 10^{-7}$	$4 \cdot 10^{-6}$
	Aspect ratio (t/d) [-]	0.1	0.1

Table 6. Mechanical properties in Moldex3D material files for GR/50 and GR/70.

2.4.2. Laser flash simulation

FEA experiments were simulated by performing time-dependent thermal analysis in Marc 2018.1. Boundary conditions were set in Patran 2018 for the isotropic model, while Mentat 2018 was used to read and run simulation on the anisotropic model. Geometry of the LFA specimens was created in HyperWorks 2020, taking care that their coordinates match the central and near-injection gate parts of the flame bar geometry (required for the correct flake orientation mapping). Note that the simulations of in-plane thermal conductivity measurements were carried out for a single strip of the specimen described in Section 2.3. Standard isotropic LFA specimens (Pyroceram 9606) with known properties [92] were used to adjust the software parameters in order to obtain a good approximation of the experimental LFA conditions. Pyroceram 9606 samples of 1 and 3 mm thickness were employed for the 0.3 and 1 ms laser pulses, respectively.

Boundary conditions were described as follows. The laser pulse was simulated as heat flux ($q = [W/m^2]$) impinging on the bottom surface of the LFA sample. As previously mentioned, the Netzsch LFA 467 HyperFlash® has a maximum pulse energy of 10 J, that can be adjusted through the lamp voltage and pulse duration. However, because no instrumental data for the correlation between these parameters is available, the heat flux input was determined based on previous studies that include computer simulation of LFA [93], [94]. The fact that the temperature rise of the sample during the laser flash diffusivity measurement is fairly small (only a few °C) was used as a starting point. The energy input E required to increase the reference sample temperature by an arbitrarily chosen value of 3°C was calculated from:

$$E = m \cdot C_p \cdot \Delta T \quad (20)$$

The next step was to determine the power delivered to the sample, which requires definition of the laser pulse shape. Figure 14 depicts the real shapes of the two different experimental pulses. Using them as input for the thermal analysis yielded inaccurate results due to the strong influence of the small impulse fluctuations. Therefore, the 0.3 ms pulse was approximated with a rectangular shape (Figure 15-a). For the 1 ms pulse, two simplified shapes were considered (Figure 15-b and 15-c). Since there was no difference between them with respect to the final result, the simpler triangular shape was selected for the next simulations. By plotting these simplified shapes as power (W) with respect to time (s), the total area below the curve gives the energy (J) (Figure 15). Therefore, by knowing the pulse width and pulse energy the peak power was calculated from simple geometrical considerations. Finally, considering that the laser spot diameter is 8.9 mm, the peak heat flux was computed as the ratio between peak laser power and laser spot area.

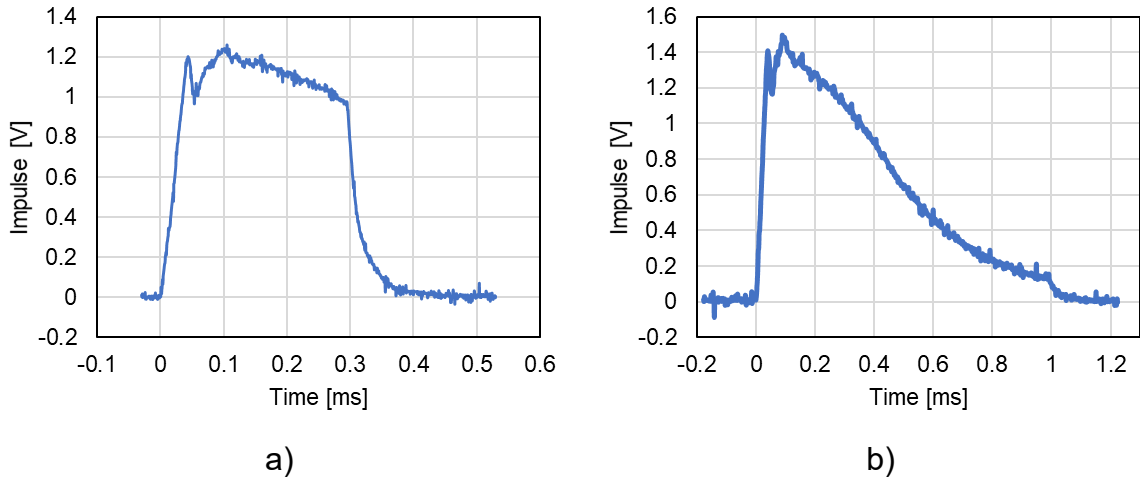


Figure 14. Experimental pulse profiles of the: a) 0.3 ms and b) 1 ms pulse width.

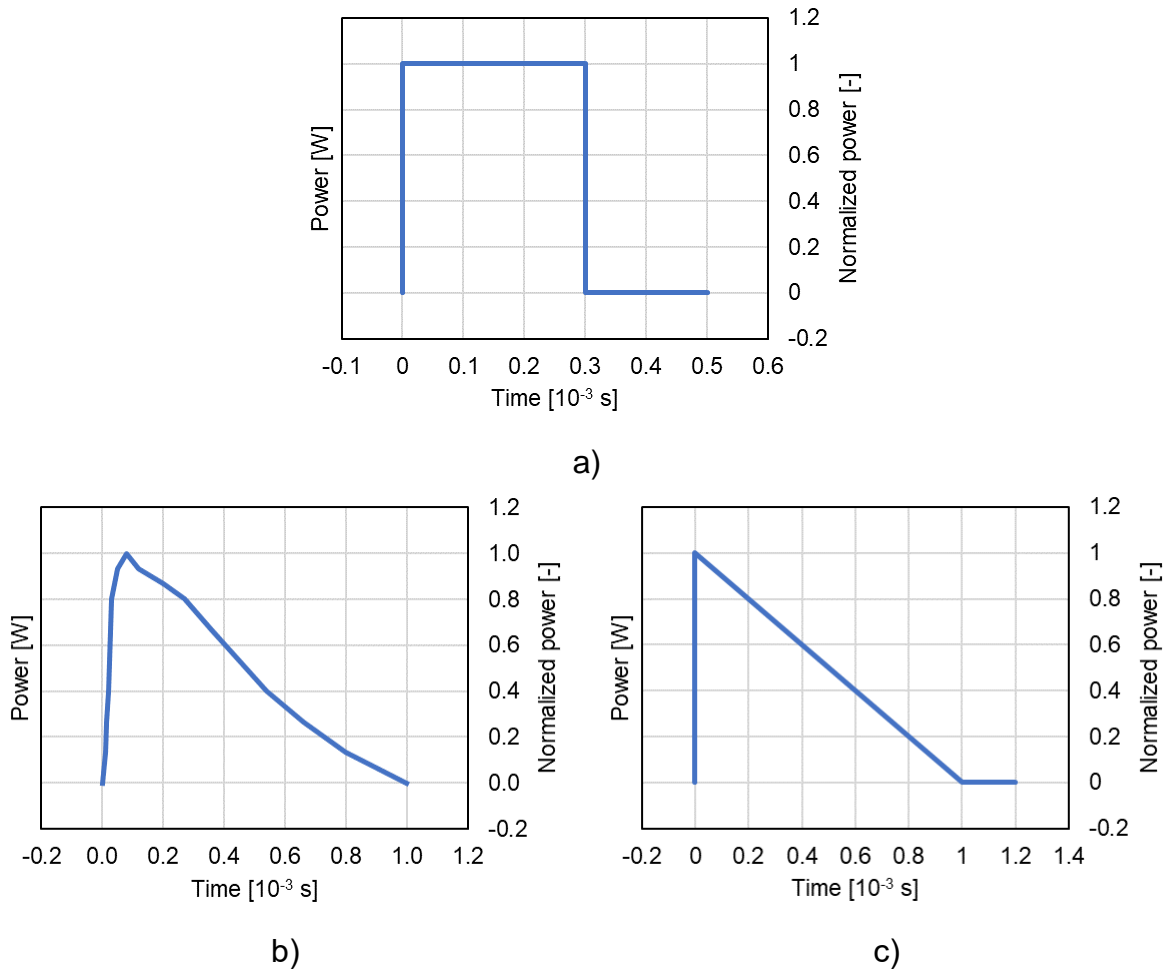


Figure 15. Simplified pulse shapes for the: a) 0.3 ms; b) and c) 1 ms pulse width used for the simulation of LFA.

Convection boundary conditions were assigned to all sample surfaces except the one where the heat flux was applied. Regarding the value of the convection

coefficient, different variations were tried out: no convection, 10 W/m²°C for all surfaces, 5 W/m²°C for all surfaces, 10 W/m²°C only for the opposite sample surface, 5 W/m²°C only for the opposite sample surface and 10 W/m²°C for the opposite sample surface with 5 W/m²°C for the sample perimeter surfaces. It was determined that this had no considerable effect on the thermal analysis results, presumably because of the relatively small sample size, simple geometry, and small temperature increase intrinsic to the laser flash technique. In the end, the single convection coefficient value of 5 W/m²°C was chosen (adopted from Phillip et al. [93]). Radiation is considered to have a significant effect on laser flash measurements only in the case of transparent and/or porous samples, therefore it was neglected in the simulations. The negligible effect of radiation for thermal diffusivity values obtained in similar LFA simulations was also confirmed by Fang et al. [84]. Finally, an initial temperature of 25°C was assigned to the solid sample geometry. Simulation boundary conditions are summarized in Table 7.

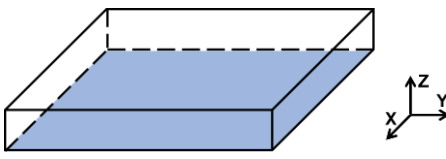
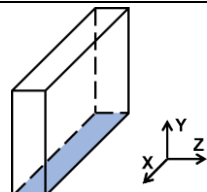
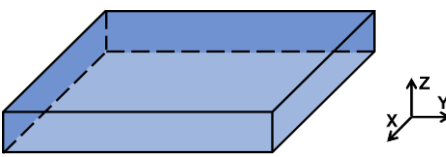
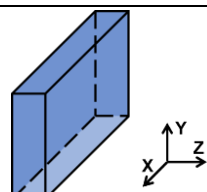
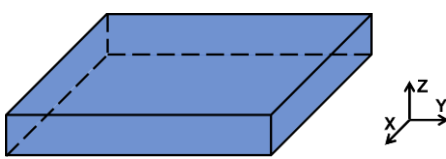
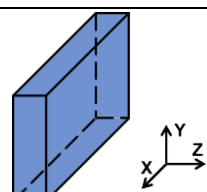
	Value	Application region	
		TP measurement	IP measurement
Heat flux	20 · 10 ⁶ W/m ² (0.3 ms pulse)		
	31 · 10 ⁶ W/m ² (1 ms pulse)		
Convection coefficient	5 W/m ² °C		
Initial temperature	25°C		

Table 7. Summary of boundary conditions used for the simulation of the through-plane (TP) and in-plane (IP) LFA experiments.

Material properties (density, specific heat and thermal conductivity) were also assigned to the finite-element models. Density and specific heat at 25°C for the two materials are presented in Section 3.1. For the isotropic case, the thermal conductivity of the composites was determined as a mean value [95]:

$$\kappa_{iso} = \sqrt{\kappa_{min} \cdot \kappa_{max}} \quad (21)$$

where the indices *iso*, *min* and *max* refer to the isotropic, minimum and maximum values of the thermal conductivity. κ_{min} and κ_{max} correspond a fully TP and fully IP filler

orientation, and they were obtained by extrapolating the LFA-measured values for the middle part of 1.47 and 3.2 mm bars (Section 3.2) to zero thickness. An example is given through the GR/70 material in Figure 16. The calculated K_{iso} values were 3.74 and 10.82 W/m°C for the GR/50 and GR/70 compound, respectively.

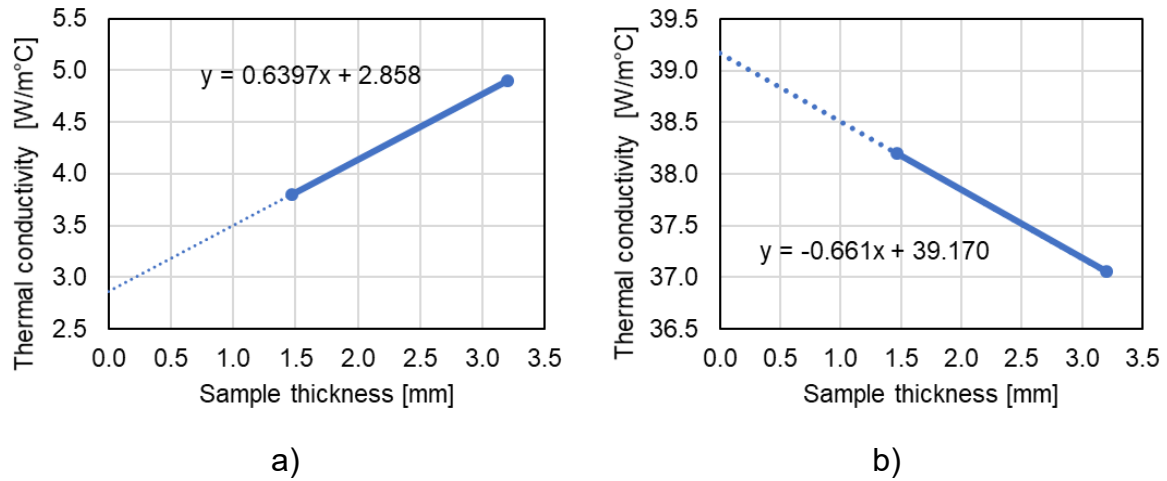


Figure 16. Extrapolation for obtaining: a) the minimum thermal conductivity and b) the maximum thermal conductivity for the GR/70 polymer compound.

The simulations carried out in this research are specific due to the relatively high heat flux input applied in a very short time. The sudden temperature rise at the start of the simulation needs to be accurately captured by using sufficiently small time steps [94]. This is especially true for materials with lower thermal conductivity (i.e. polymers and ceramics), where the heat transport through the sample occurs rather slowly, so it is more challenging to obtain accurate temperature distributions for times close to application of the laser pulse. The small time steps, in turn require finer mesh sizes, as described by the following equation [96]:

$$\Delta t_i = \frac{\Delta X^2 \cdot \rho \cdot C_p}{10 \cdot \kappa} \quad (22)$$

where Δt_i is the initial time step and ΔX^2 is the mesh size. If this condition is not satisfied, computation instability occurs in the beginning of the simulation [97]. However, if the mesh size is smaller than what is needed to obtain accurate results, this can significantly increase the computational power and time. Due to the simple geometry of the specimens, a hexagonal element solid mesh was utilized for all analyses. For the Pyroceram 9606, the most appropriate mesh sizes were 0.15 for the thinner sample and 0.3 for the thicker sample, and these mesh sizes were also adopted for the samples of interest. For the preliminary analysis, an adaptive thermal time step was used, with initial time step of 10^{-6} s and total time of 5 s. Different time step combinations were evaluated in order to determine the most accurate one to be used with the GR/50 and GR/70 materials (Figure 17). Apart from the already mentioned adaptive thermal, the following two were also investigated: the time steps described by Evans et al. [94] and the time steps suggested by Philipp et al. [93]

(10^6 s for the time of the pulse application) followed by adaptive thermal time step until 5 s. The time step size of the former study resulted with temperature rise curves that closely match the experimental curves for the Pyroceram 9606, and therefore it was the one utilized for the LFA simulations of the polymer compound materials.

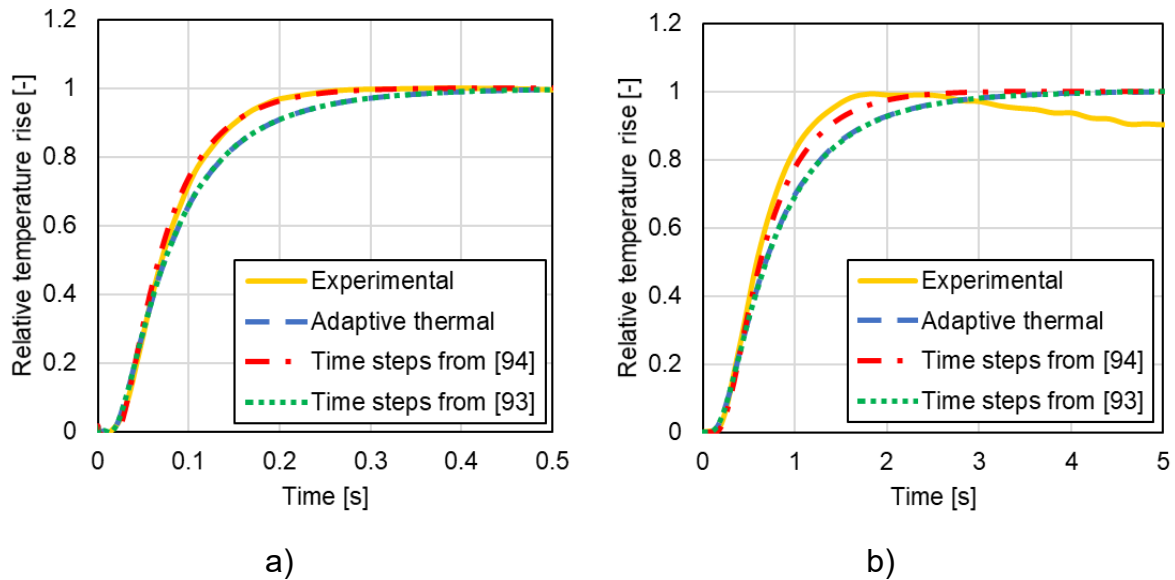


Figure 17. Comparison between LFA experiment and LFA simulations with various time steps for Pyroceram 9606 sample of: a) 1 mm; b) 3 mm thickness.

In conclusion, by evaluating different simulation parameters using the reference samples, it was established which are the most appropriate ones to proceed with the samples of interest. Additionally, in case further adjustments were required, the parameters that influence and those that do not influence the final result were learned (presented in the Section 3.4).

2.4.3. Flake orientation mapping

This section describes the main focus of the thesis work, i.e. the FEA model used for simulation of the anisotropic thermal behavior of injection molded polymer composites. The anisotropy of the polymer compounds is considered by using the flake orientation obtained from Moldex3D, finite element analyses performed using the MSC software packages and a Microsoft Excel macro program developed by the Technical Assistance in LATI.

Firstly, the injection molding simulations in Moldex3D and LFA simulations in MSC Patran were done as described in Section 2.4.1 and 2.4.2. Then, using the FEA interface function in Moldex3D, the graphite flake orientation is mapped over the LFA sample geometry by importing the .dat file acquired from the MSC Patran isotropic analysis. In this way, the flake orientation for the LFA sample is obtained. As already mentioned, it is essential that the coordinates of the LFA sample geometry match the area of interest of the part geometry used in Moldex3D. In this case, different geometry files were created corresponding to the middle and injection areas of the injection

molded flame bar. For the next part, the following steps were performed by using the Excel macros:

- *Importing the .dat file* containing the geometry and results from the LFA simulation of the isotropic material in Patran;
- *Importing the .o2d file* obtained from mapping the flake orientation in Moldex3D. This file contains the filler orientation along the x-, y- and z-axes for each mesh element. The macro takes into account the minimum and maximum thermal conductivity, corresponding to a fully TP and fully IP filler orientation (explained in Section 2.4.2 and Figure 16), and applies these values in the three directions according to flake orientation. The flake orientation is given by:

$$\theta = \theta_{xx} + \theta_{yy} + \theta_{zz} = 1 \quad (23)$$

where θ_{xx} , θ_{yy} and θ_{zz} represent the relative amounts of flakes oriented in the specific direction. Then, the thermal conductivity along the three directions is:

$$\kappa_{xx} = \kappa_{min} + \theta_{xx}(\kappa_{max} - \kappa_{min}) \quad (24)$$

$$\kappa_{yy} = \kappa_{min} + \theta_{yy}(\kappa_{max} - \kappa_{min}) \quad (25)$$

$$\kappa_{zz} = A[\kappa_{min} + \theta_{zz}(\kappa_{max} - \kappa_{min})] \quad (26)$$

where A is a factor that takes into account filler anisotropy. For the GR/70 material shown in Figure 16, the obtained values for κ_{min} and κ_{max} were 3 and 39 W/m°C, respectively. In the case of GR/50, due to contradictory results which are discussed in Section 3.2, approximate thermal conductivities of 1 and 14 W/m°C were used. Filler anisotropy was considered by a correction factor of 0.4 (determined as most accurate for the current analysis);

- *Filling in the material card.* In this step, a tolerance value (0.01 – 0.5) is input so that elements with similar values of the κ_{xx} and κ_{yy} thermal conductivity can be grouped together. This creates a material card which represents the anisotropic flake-filled material as a combination of a number of materials with various anisotropic thermal conductivities. In this case, the tolerance values were chosen so that the number of materials is 1000±50;
- *Modifying the original .dat file* to include the material card;
- *Exporting the modified .dat file* compatible with MSC Marc Mentat.

Finally, the modified .dat file was imported into MSC Marc Mentat in order to perform thermal transient analysis for the anisotropic material. The loading and boundary conditions were the exact same ones used in MSC Patran, as this information is also contained in the .dat file.

2.4.4. Case study

The accuracy of the anisotropic model for thermal conductivity was also evaluated for a real case study; simulation results were compared with experimentally measured temperature distributions for a GR/50 heat sink used for downlights. This part of the work is based on a previous collaboration between LATI and Whitecroft Lighting (UK).

Experimental thermal tests were performed by Whitecroft Lighting. The temperature distribution for the heat sink of an operating downlight was measured via infrared camera (Fluke Ti25 Thermal Imager) at ambient temperature of 22°C. Results were collected for LEDs with different light intensities of 2000, 3000 and 5000 lm.

The geometry used for performing the computer simulations contains the GR/50 heat sink with an aluminium spreader and aluminium printed circuit board (PCB) and is presented in Figure 18. First, the heat sink injection molding (only for the filling stage) was simulated using Moldex3D. The process parameters were adjusted from the default software-suggested values, with setting a 1.5 s filling time in order to guarantee the complete filling of the part. Regarding the injection molding configuration, a simple center sprue gate was used. MSC Patran interface was again utilized for performing isotropic thermal simulations as the second step. For the case study, steady state thermal analyses were performed with boundary conditions explained in the following. The source of thermal energy was the diode with varying light intensities, represented as heat flux loading applied over the PCB. Information about the LED thermal power was supplied by Whitecroft Lighting. For calculating the heat flux, the thermal power was divided by the PCB area (345.95 mm²), resulting with 32.66, 45.93 and 90.65 mW/mm² for the 2000, 3000 and 5000 lm LEDs, respectively. The convection coefficient was 10 W/m²°C, assigned to all external surfaces of the heat sink. In contrast to the simple LFA geometry, heat transfer by radiation is an important contribution for heat sinks. Radiation view factor for the fins was calculated within the MSC Patran interface and emissivity of 0.89 was input for the GR/50 material. Two different GR/50 thermal conductivities were evaluated: 3.74 W/m°C (calculated in Section 2.4.2) and 10 W/m°C (previously determined by LATI Technical Assistance as best fit for thermal analysis). The aluminium was assigned a thermal conductivity of 130 W/m°C. To simulate the heat transfer between the heat sink, spreader and PCB, they were modelled as deformable contact bodies with contact heat transfer coefficient of 10⁶ W/m²°C. Regarding the Excel macros, two values for the filler anisotropy were compared: 0.4 (best fitting the LFA simulations) and 1 (used by LATI Technical Assistance in the past). The material card was filled in with 1037 isotropic materials by inputting a tolerance coefficient of 0.126. The analyses were again concluded by running anisotropic material simulations using Marc Mentat interface.

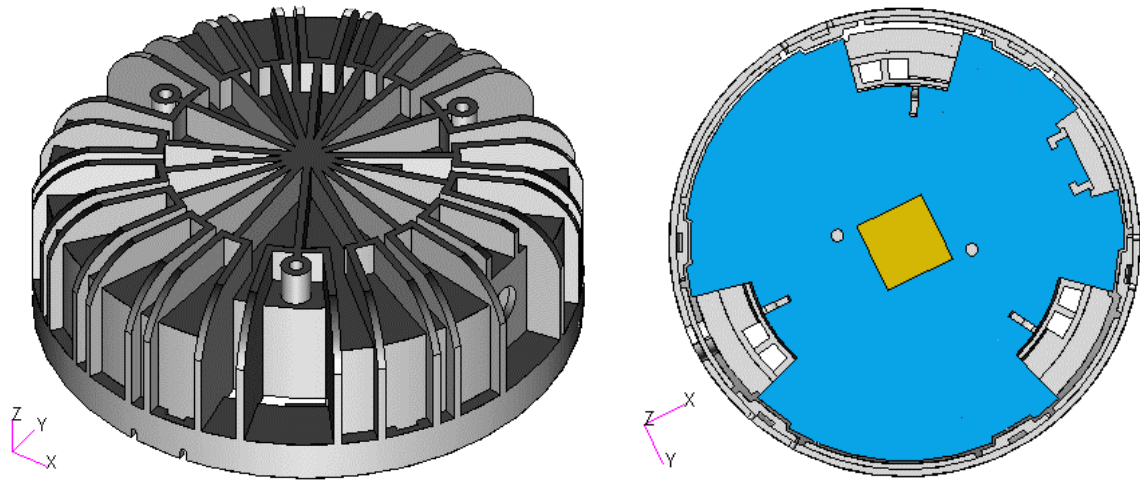


Figure 18. Geometry file for the GR/50 heat sink (grey) with aluminium spreader (blue) and PCB (yellow).

3. Results and discussion

3.1. Material characterization

Results of all characterization procedures performed for the GR/50 and GR/70 materials are summarized in Table 8 below. Increasing the graphite content increases the composite density, as the typical value of density for PA6 is 1.14 g/cm³, while for expanded graphite it is 2.25 g/cm³. The elastic modulus is higher for GR/70, which indicates higher composite stiffness. It is known that this occurs due to the dominant effect of graphite rigidity at high loadings, which is also the case here. The graphite flakes reduce the mobility of the polymer chains, further contributing to the modulus increase [98]. Such result also suggests good filler dispersion and good filler-matrix interaction [99]. On the other hand, the presence of 20 wt% more graphite in the polymeric compound decreased the ultimate tensile strength by 2 MPa. This can be explained through the fact that the mechanical strength has greater sensitivity to defects in the matrix than the elastic modulus does [100]. Increasing the amount of graphite may introduce defects due to agglomeration, but considering the small difference between GR/50 and GR/70, the effect here is almost negligible. The effect on toughness evaluated through the fracture energy is more evident. The Charpy test gives information about the energy absorption and dissipation phenomena. It can be seen that adding graphite in higher concentrations resulted with a more brittle compound, which is in line with previously reported results [101]. This can be attributed to a modification of the energy absorption mechanism, increased brittleness [102] and decreased molecular mobility [103] of the composite. Finally, the addition of graphite in higher concentrations decreases the specific heat capacity. This improves the thermal stability of the material, which is key for the applications of the GR/50 and GR/70 compounds.

Material		GR/50 composite	GR/70 composite
Density ρ [g/cm ³]		1.494	1.728
Modulus E [GPa]		8.372	11.344
Ultimate tensile strength σ_{UTS} [MPa]		48	46
Fracture energy [kJ/m ²]	Unnotched specimen	8.951	3.744
	Notched specimen	3.258	1.529
Specific heat capacity C_p [J/g°C]	25°C	1.119	1.012
	50°C	1.264	1.139
	75°C	1.393	1.243

Table 8. Physical, mechanical and thermal properties of used materials.

SEM micrographs presented in Figure 19 were obtained from the cross-section of a 1.47 mm thick GR/50 bar. The letter in the top-left index describes the location with respect to the longitudinal dimension of the bar, i.e. middle (M) and injection (I) zone. On the other hand, the numbers 1, 2 and 3 describe the origin of the SEM image

with respect to the bar width and are interpreted as left, center and right, respectively. For reference, the injection gate is located on the right side. The results reveal a compact microstructure of a composite with well-dispersed filler particles. No clear indications of graphite agglomeration can be seen, which would cause significant changes in the local thermal conductivity [104]. The typical skin-core morphology of injection molded samples is observed in Figure 19 (M-2 and I-2). In the skin layer, the flakes are highly oriented along the flow direction and are parallel to the surfaces of the cavity. This is caused by the fountain flow behavior of the melt front pushing out the flakes from the center layer to the walls, where they are subjected to the maximum shear stresses in the flow profile and therefore strongly oriented. They maintain this high orientation in the final product since the skin layer is the first one to solidify (neglecting the very thin surface layer with a random-in-plane filler orientation described in section 1.2.1). The core layer of the cross section has a more disordered structure but the orientation along the flow direction is still clearly visible, similarly to [104]. Comparing M-2 and I-2 in Figure 19, it can be seen that the skin layer thickness in the injection area is slightly smaller compared to the middle of the bar. Since the thermal conductivity is strongly affected by filler orientation, the injection area can be expected to have a lower IP and higher TP thermal conductivity due to the larger size of the core layer where randomly oriented graphite forms a three-dimensional conductive network. Also, the alignment of flakes in the core region is generally stronger for the middle, but it can still be noticed for the injection zone. This is in accordance with the results of Hamanaka et al. [105], who found that the filler orientation in the central part of the thickness profile intensifies as filling advances. In Figure 19 (M-1, I-1 and M-3) one can also observe the graphite flakes being pushed up the vertical walls of the mold. Moving towards the center of the core layer, it is evident how the flake alignment gradually changes from a vertical to a horizontal direction. The area represented in Figure 19 (I-3) is the closest to the injection gate and therefore it is noticeably different than the other ones. Near the injection gate, the flake orientation is more chaotic and since this location is where the hot melt enters the mold, the orientation resembles the fountain flow.

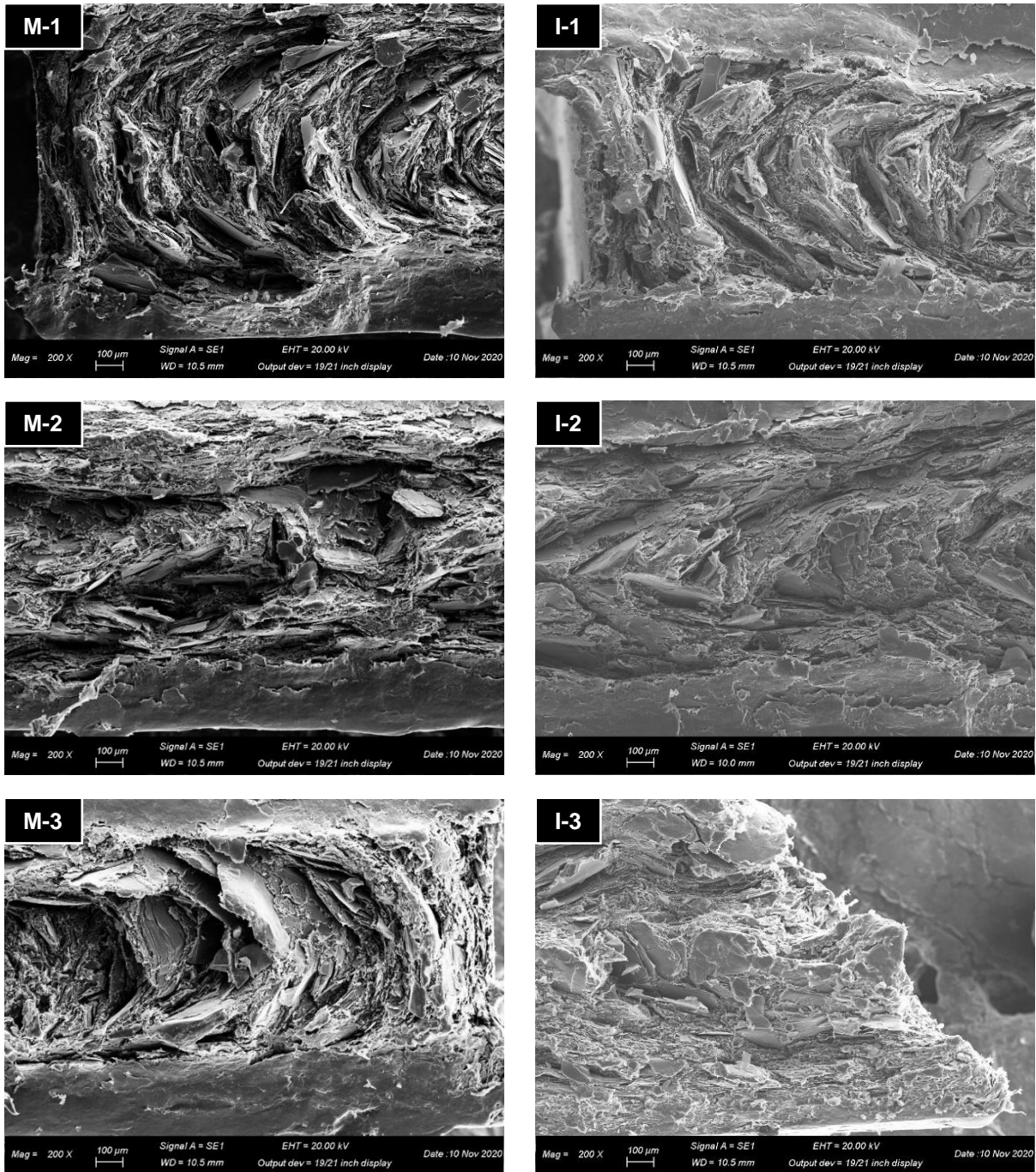


Figure 19. SEM images taken from the cross section of a 1.47 mm thick GR/50 flame bar.

3.2. LFA experimental results

3.2.1. Series 1

This section presents the results of the LFA measurements for the first series of injection molded samples. As explained in Section 1.1.3.2, the laser flash method measures the thermal diffusivity, and together with the material density and specific heat capacity, it is used to calculate the thermal conductivity. Results for the GR/50

compound are shown in Table 9. The table presents results from all three replicate measurements by considering the bar area from which the LFA sample was cut, the injection molded bar thickness and measurement direction. The results match the theory regarding the filler orientation influence on the thermal conductivity; the samples transfer heat much faster along the graphite two-dimensional planes, i.e. the in-plane direction.

Area	Sample thickness [mm]	Direction	α [mm ² /s]			κ [W/m°C]		
			1°	2°	3°	1°	2°	3°
Middle	1.47	TP	0.750	0.770	0.773	1.255	1.289	1.294
		IP	7.816	7.520	7.812	13.080	12.586	13.073
	3.20	TP	1.166	1.179	1.147	1.951	1.973	1.919
		IP	8.330	8.195	8.129	13.941	13.715	13.604
Near injection gate	1.47	TP	0.832	0.836	0.900	1.392	1.399	1.506
		IP	7.162	7.031	7.241	11.986	11.767	12.118
	3.20	TP	1.311	1.314	1.253	2.195	2.199	2.097
		IP	7.849	7.797	7.845	13.135	13.049	13.129

Table 9. LFA results for GR/50 samples.

For better visual representation, average values from the results in Table 9 are given in Figure 20, together with the standard deviation. The standard deviation is higher for the IP thermal conductivity, probably due to the higher sample thickness and less straightforward sample preparation. Figure 20 also reveals that the highest average IP conductivity value was achieved for the 3.2 mm thick sample. Before carrying out the experiment, it was assumed that the bars of 1.47 mm thickness would have higher flake orientation and therefore higher κ value along the longitudinal bar direction. The assumption was based on the idea that the shear stress in the thinner bar would be higher, increasing the directionality of the graphite. However, this was not confirmed experimentally. From Figure 20, the 1.47 mm bar showed lower IP conductivity, both in the middle and in the injection area of the bars. The 3.2 mm sample also showed higher thermal conductivity in the TP direction, which is more in line with previous expectations, since the anticipated lower shear stress should allow the flakes to orient more along the through-plane direction.

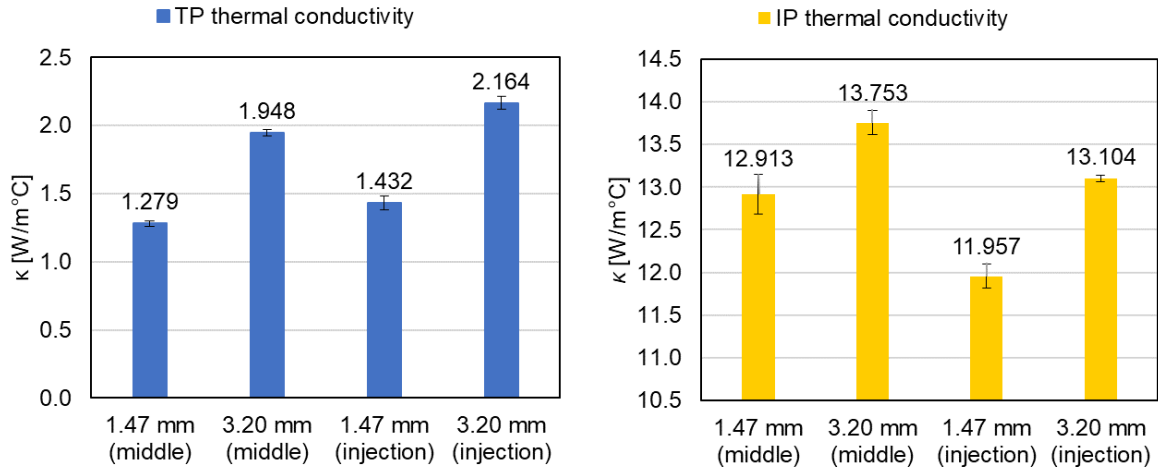


Figure 20. Average values and standard deviation for the thermal conductivity of GR/50.

Regarding the unexpectedly high IP conductivity for the 3.2 mm sample, it can be potentially explained through the relative thickness of the core layer (containing less IP oriented filler particles) being influenced by the cavity thickness. The higher shear rates in the 1.47 mm specimens could cause greater shear thinning (pseudoplasticity) with a corresponding flatter velocity profile, and therefore a wider core region. In any case, as the thermal conductivity values for the two bar thicknesses are rather similar, it can be expected that any existing difference in the relative core layer thickness is only marginal, which is in agreement with [106]. However, it is interesting that the 1.47 mm sample measured lower conductivity not only in the IP, but also in the TP direction. This suggests that the answer might not be only in the flake orientation (although it still plays an important role).

If the shear-thinning effect is not very strong (which can indeed be the case for lower injection speeds [106]), the shear stress may be high as initially presumed and therefore separate the graphite flakes more efficiently. The degree of dispersion for high aspect ratio fillers is not a simple consideration when it comes to its effect on the thermal conductivity. In Figure 21, the same amount of filler is represented with two different dispersion qualities: ideal (Figure 21-a) and good dispersion with the presence of some agglomerates (Figure 21-b). Higher κ value in all directions will most probably be achieved in the latter scenario, which in this case corresponds to the 3.2 mm samples. Such moderate degree of agglomeration forms a path for the phonons to travel far without hinderance. On the other hand, the perfectly dispersed filler (as in the 1.47 mm thick samples) forms a shorter path with a larger number of interfaces. The filler/matrix interfaces might be a bigger obstacle for heat transport than the slightly longer phonon path [104], making the samples of 3.2 mm thickness better thermal conductors.

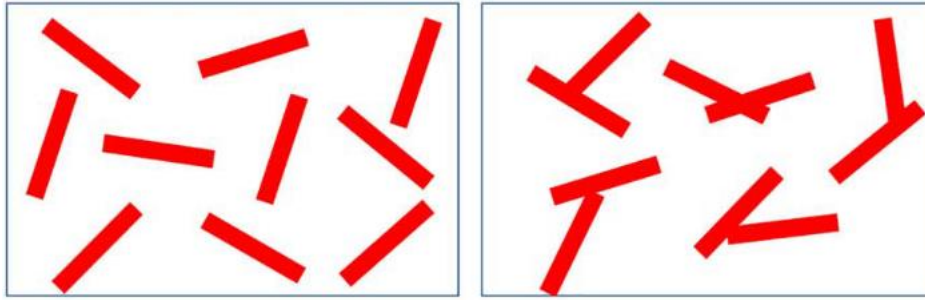


Figure 21. High aspect ratio fillers (red) in a polymer matrix (white) with a different degree of dispersion: a) ideal; b) good dispersion with presence of agglomerates [104].

Observing the average values for the middle against the injection areas, the obtained results are more in line with the study hypothesis. Indeed, from Figure 20 it is evident that the value for the TP conductivity increases while for IP it decreases, confirming again the more random orientation near the injection gate. Additionally, this occurs due to already mentioned variation of the skin region size (the skin layer has higher thickness in the middle area, and since it contains more oriented flakes it increases the IP thermal conductivity).

Table 10 presents the α and κ values for all three replicate measurements carried out for the GR/70 compound. Average values for the thermal conductivity, along with the standard deviation are illustrated in Figure 21. Again, the thermal transport constants are higher in the IP direction, but the highest average value was recorded for the 1.47 mm thick sample taken from the middle of the bar. Moreover, by changing the graphite content from 50 wt% to 70 wt%, the in-plane thermal conductivity increases more readily with respect to the through-plane. This is due to the nature of the injection molding process, which causes the polymer chains to flow and filler particles to align with the flow. The reduced number of graphite/polymer interfaces, as well as the anisotropy of the graphite itself contribute to the enhanced thermal conductivity in the IP direction [104].

Area	Sample thickness [mm]	Direction	α [mm ² /s]			κ [W/m°C]		
			1°	2°	3°	1°	2°	3°
Middle	1.47	TP	2.139	2.144	2.227	3.744	3.753	3.898
		IP	21.557	22.255	21.650	37.738	38.959	37.899
	3.20	TP	2.791	2.665	2.950	4.886	4.665	5.164
		IP	20.897	21.548	21.058	36.581	37.721	36.864
Near injection gate	1.47	TP	2.531	2.536	2.499	4.431	4.439	4.373
		IP	21.786	20.859	20.965	38.137	36.516	36.701
	3.20	TP	3.400	3.447	3.451	5.952	6.035	6.041
		IP	20.236	19.896	20.981	35.425	34.830	36.729

Table 10. LFA results for GR/70 samples.

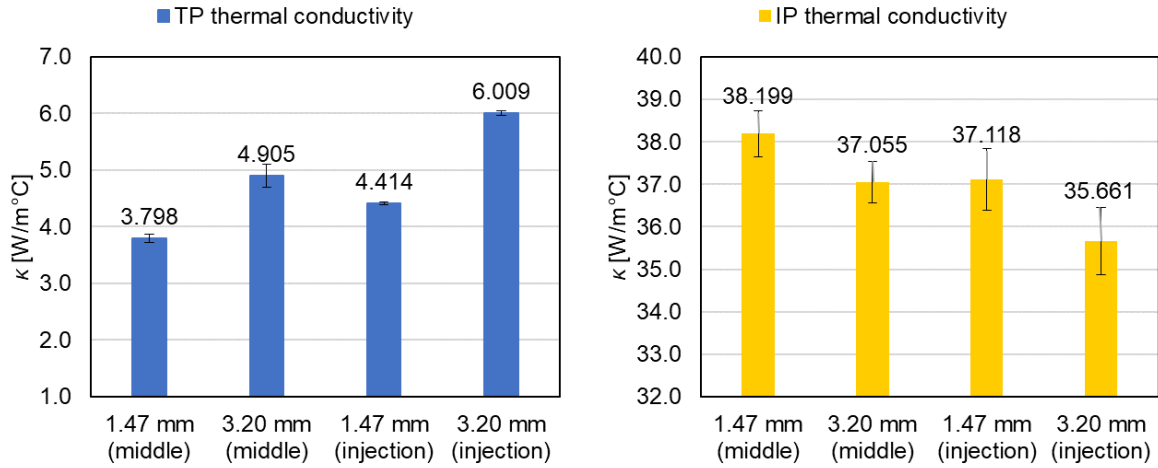


Figure 22. Average values and standard deviation for the thermal conductivity of GR/70.

In the case of GR/70, results considering the sample thickness and directional thermal conductivity match the expectations; LFA specimens obtained from the thinner injection molded bar showed higher IP thermal conductivity. Two phenomena with opposite effects may contribute to this: 1) The higher graphite content in GR/70 makes this compound more thermally conductive. By decreasing the cooling time, the frozen layer skin thickness increases and the high shear region is moved away from the walls, resulting with a reduced core area; 2) The larger filler content increases the degree of non-Newtonian behavior (shear thinning) in the melt, creating a flatter velocity profile and therefore a larger core area. With analogy to the results of [106], the 3.2 mm bar should have a thinner skin layer by increasing the graphite content. This is a result of the flatter velocity profile caused by the more pronounced non-Newtonian behavior. On the other hand, in the case of 1.47 mm the skin layer likely has a higher thickness for the GR/70 compared to the GR/50 material samples. In this case, the effect of faster cooling probably dominates over the increased shear thinning, producing a thicker frozen skin layer of highly oriented flakes. Furthermore, for the GR/70 compound, the TP conductivity of the thinner specimens remains lower compared to the thicker ones, providing another indication of higher alignment of the flakes in the longitudinal direction.

The GR/70 melt has higher viscosity at the injection molding temperature, which makes full dispersion of graphite flakes in the 1.47 mm samples more difficult. Furthermore, due to their increased number, the graphite flakes will have more contact points, and form agglomerates more easily, which was already explained as beneficial for the continuity of the conductive network. Finally, the contrast when going from the middle to the injection area of the bar is evident as in the case of the GR/50 compound; the IP conductivity decreases and TP conductivity increases due to more random flake orientation and decreased thickness of the skin layer.

3.2.2. Series 2

The results of the second series are presented with the same template as Series 1, with the individual measurement results in Table 11 and average results with standard deviation in Figure 23. Although the purpose of this series was to correct the unexpected results regarding the two different thicknesses of the GR/50 bars, its outcome was not very different; the 3.2 mm samples retained the higher in-plane conductivity. Once again, the 3.2 mm sample had higher conductivity also in the through-plane direction. However, the thermal conductivities for the 1.47 mm thick bar did display a small increase in both directions. The average values of the IP thermal conductivity in the middle zone of the bars decrease compared to the first series GR/50. What potentially happened can be explained this way: at higher injection speeds, the frozen layer thickness decreases due to the greater degree of shear thinning flattening the velocity profile and bringing the high shear region closer to the walls. Therefore, the more randomly oriented core layer will have greater influence on the heat transport properties, increasing the TP and decreasing the IP thermal conductivity. This is in accordance with the obtained results, as seen from comparing the middle zone thermal conductivities in Figures 20 and 23. Furthermore, this effect is less pronounced for the 3.2 mm sample, due to the reduced influence of the frozen skin layer in the thicker profile [106]. Indeed, the rise of TP thermal conductivity due to increasing the injection speed in Series 2 was 29.5% for the 1.47 and 14.0% for the 3.2 mm thick specimens.

Area	Sample thickness [mm]	Direction	α [mm ² /s]			κ [W/m°C]		
			1°	2°	3°	1°	2°	3°
Middle	1.47	TP	1.084	1.080	1.087	1.815	1.807	1.819
		IP	7.637	7.616	8.160	12.781	12.746	13.656
	3.20	TP	1.289	1.331	1.326	2.158	2.227	2.220
		IP	7.973	7.897	8.303	13.343	13.216	13.895
Near injection gate	1.47	TP	1.147	1.057	1.123	1.920	1.769	1.879
		IP	7.836	7.942	7.881	13.114	13.292	13.189
	3.20	TP	1.297	1.318	1.320	2.171	2.206	2.209
		IP	8.099	8.591	8.105	13.554	14.378	13.565

Table 11. LFA results for GR/50_{hv} samples.

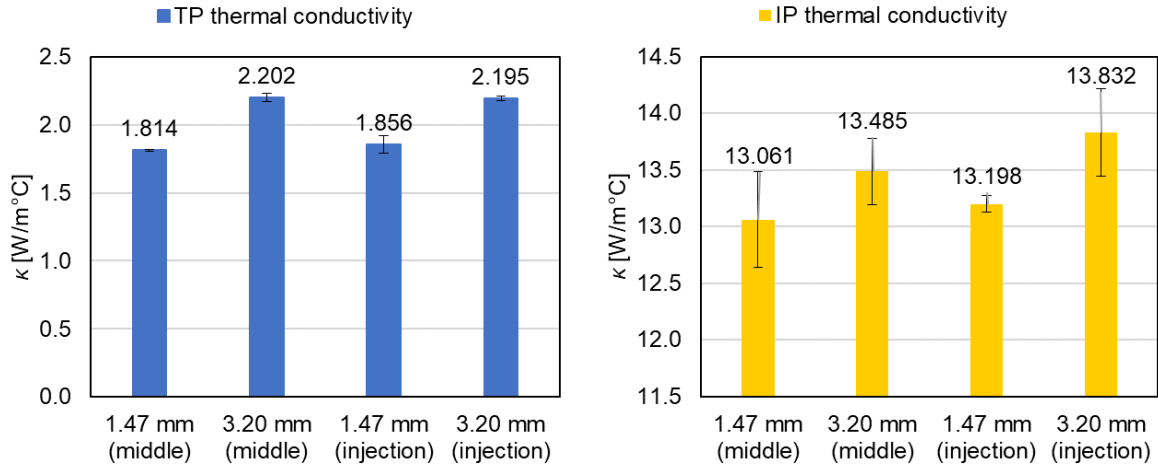


Figure 23. Average values and standard deviation for the thermal conductivity of GR/50_{hv}.

The main difference compared to the GR/50 samples of the first series is the degree of flake alignment in the middle with respect to the injection area. In the second series, the highest IP thermal conductivity was reached for the 3.2 mm thick sample representing the injection zone. Furthermore, the TC values of the middle and injection regions are more similar to each other (Figure 23).

3.3. Injection molding simulation results

The injection molding simulations were performed not only for the need of the anisotropic thermal analysis, but also to further evaluate the reported results for the thermal diffusivity and conductivity. Simulation results for the flake orientation are presented in Figure 24. The labelled areas correspond to the SEM micrographs in Figure 19, demonstrating a good match for the flake orientation between experiment and simulation. The numeric scale represents the filler orientation distribution in the major direction of filler orientation. A value of 0.3 signifies that the graphite flakes are oriented completely randomly (Figure 25), while a value of 1 means that the flakes are fully oriented over that region by the flow field. Note that for all Moldex3D results, the flake alignment is given by the orientation of the normal axis (red arrow in Figure 25).

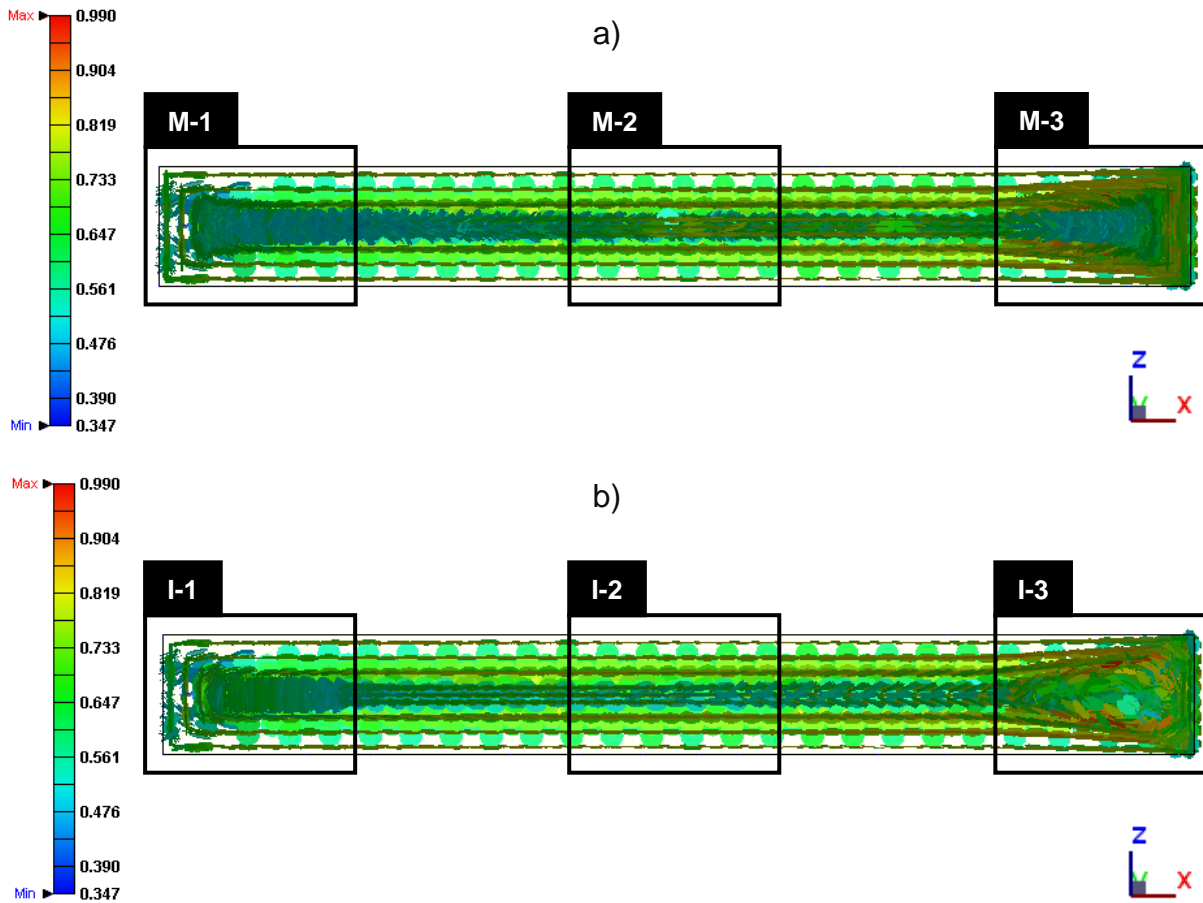


Figure 24. Flake orientation for GR/50 in the cross section referring to the: a) middle area; b) injection gate-area.

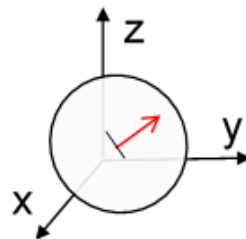
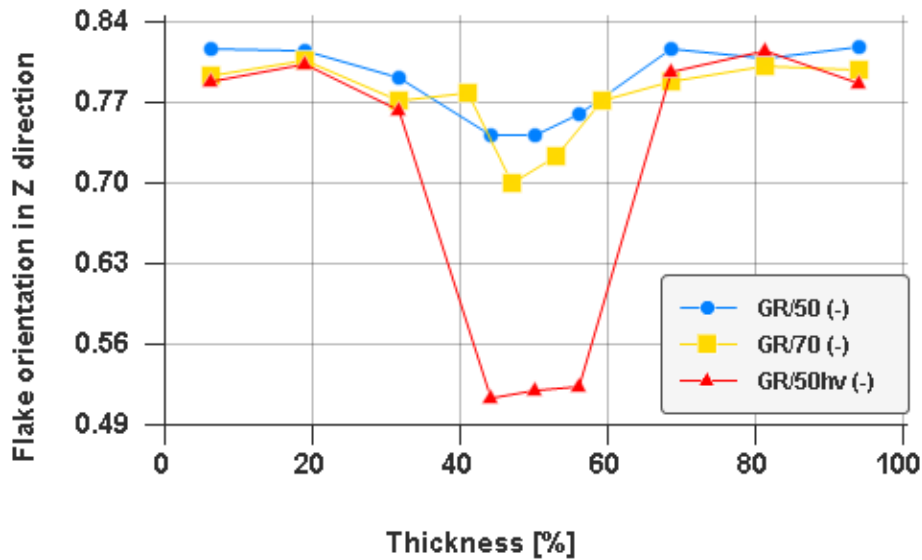


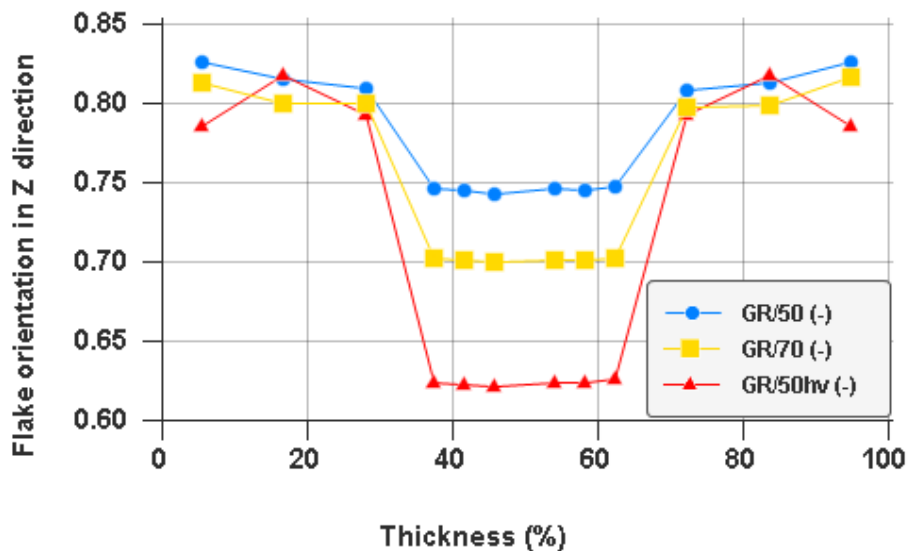
Figure 25. Representation of flake orientation in Moldex3D.

Figure 26 shows the through-thickness flake orientation in z-direction in the middle zone, for the central part of the cross section (M-2 according to the indexing in Figure 19 and 24). The GR/70 has the smallest relative core thickness out of all 1.47 mm samples (Figure 26-a). This is due to the high viscosity contributing to the formation of a thin and discontinuous core [107], as well as the previously explained effects of faster cooling. The GR/50_{hv} sample shows the lowest flake orientation in the core layer, due to the low shear rate which can be seen in Figure 27-c. Indeed, the GR/50 and GR/70 cross sections show higher shear rate in the central area (Figure 27-a and 27-b), while for the GR/50_{hv} the shear rate in the center decreases with respect to the top and bottom cavity walls. Similar trends for the core layer orientation of GR/50 and GR/50_{hv} can be observed for the 3.2 mm sample (Figure 19-b). This is

in correspondence with the LFA results that revealed lower thermal conductivity for the GR/50_{hv}, as well with its lower shear rate in the mid-plane (Figure 27-d and 27-f). By comparing Figure 26-a and figure 26-b, the GR/70 frozen layer thickness decreases for the 3.2 mm sample due to the more pronounced shear thinning behavior, which was also evident in the experimental LFA results. The simulations confirmed that the high shear region is closer to the walls for the 3.2 mm sample, which can be seen by comparing Figure 27-b and 27-e. Moldex simulations for the GR/70 specimens also validate the flatter velocity profile for the thicker flame bar (Figure 28).

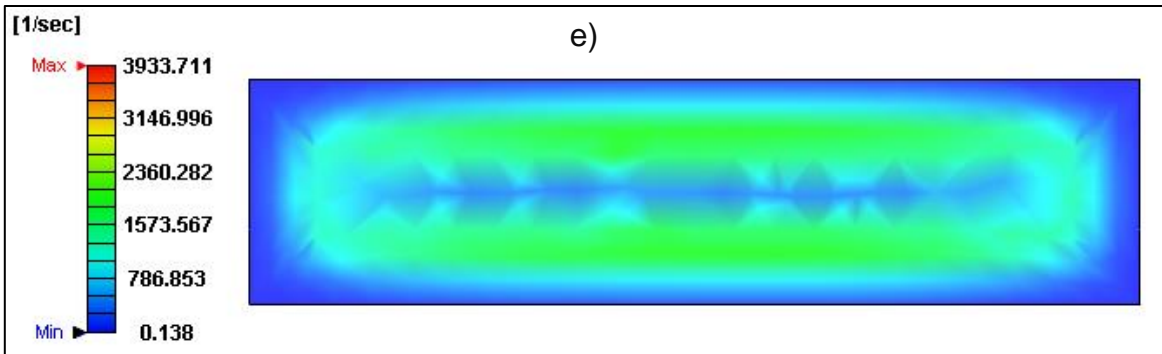
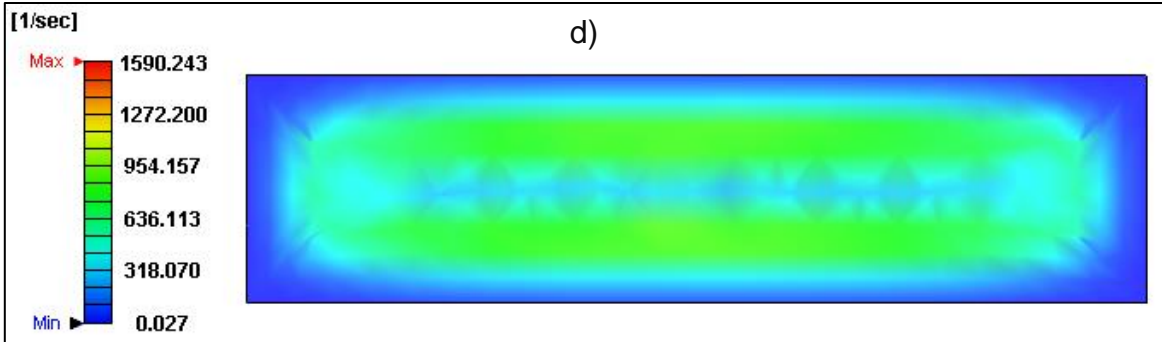
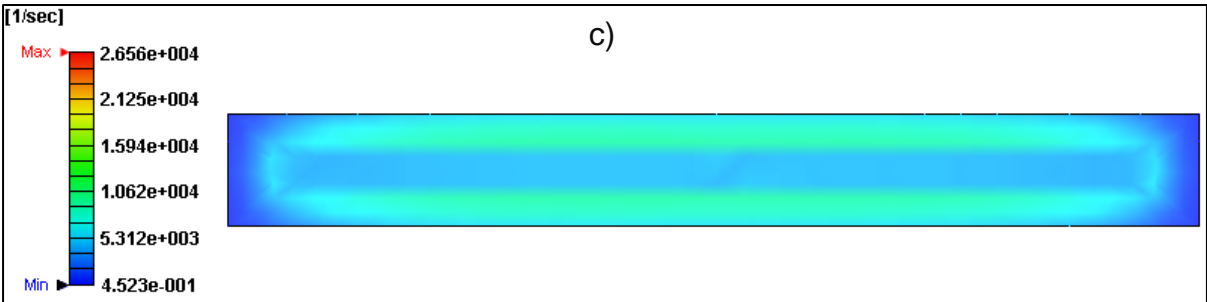
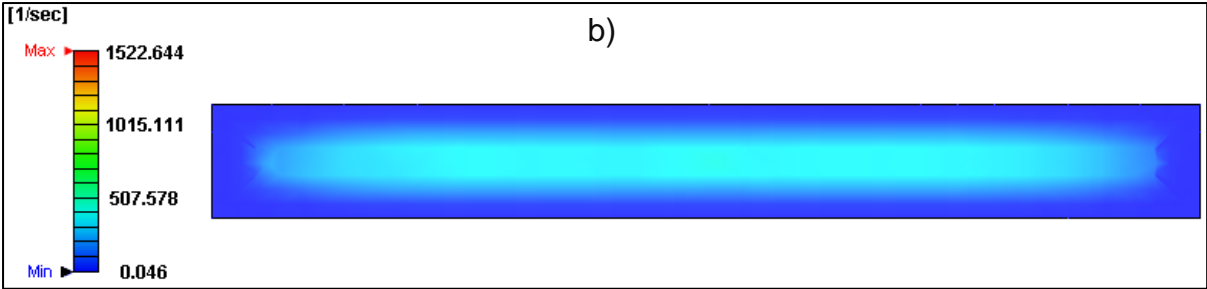
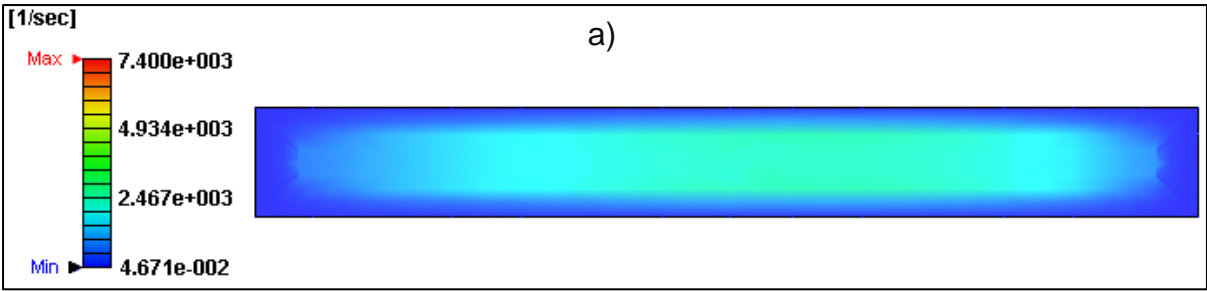


a)



b)

Figure 26. Profile of the flake orientation in z-direction for the central part of the injection molded bars: a) 1.47 mm thickness; b) 3.2 mm thickness.



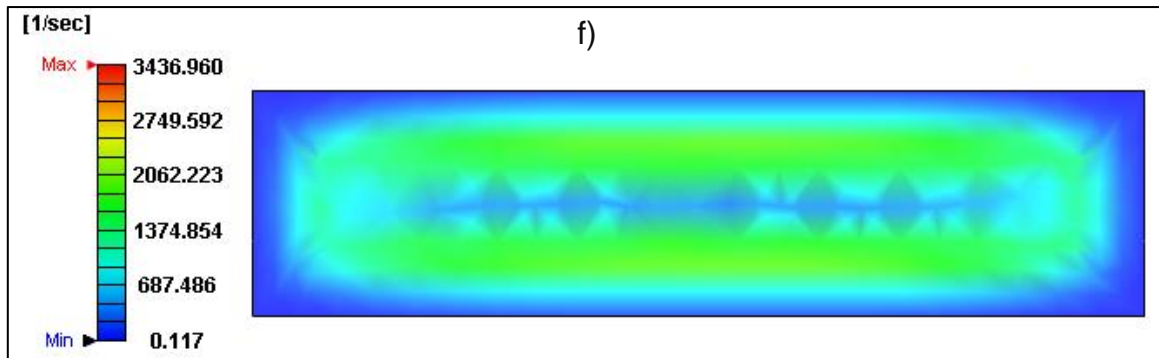


Figure 27. Shear rate at the end of filling across the central cross-section of: a) GR/50 (1.47 mm); b) GR/70 (1.47 mm); c) GR/50_{hv} (1.47 mm); d) GR/50 (3.2 mm); e) GR/70 (3.2 mm); f) GR/50_{hv} (3.2 mm).

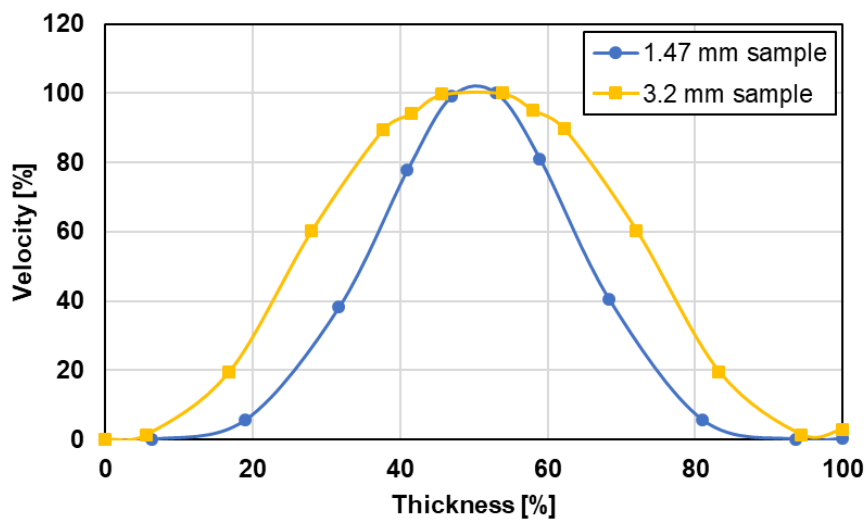


Figure 28. Through-thickness velocity distribution in the center of GR/50 flame bars.

Figure 29 is in agreement with the SEM (Figure 19) and LFA results (Table 9; Figure 20) regarding the orientation distribution in the middle against the injection zone for the GR/50 sample of 1.47 thickness. The explanation behind this phenomenon has already been discussed in Sections 3.1. and 3.2. Figure 30 suggests the lower shear rate in the central part of the injection cross section as a possible reason for low orientation in the core region.

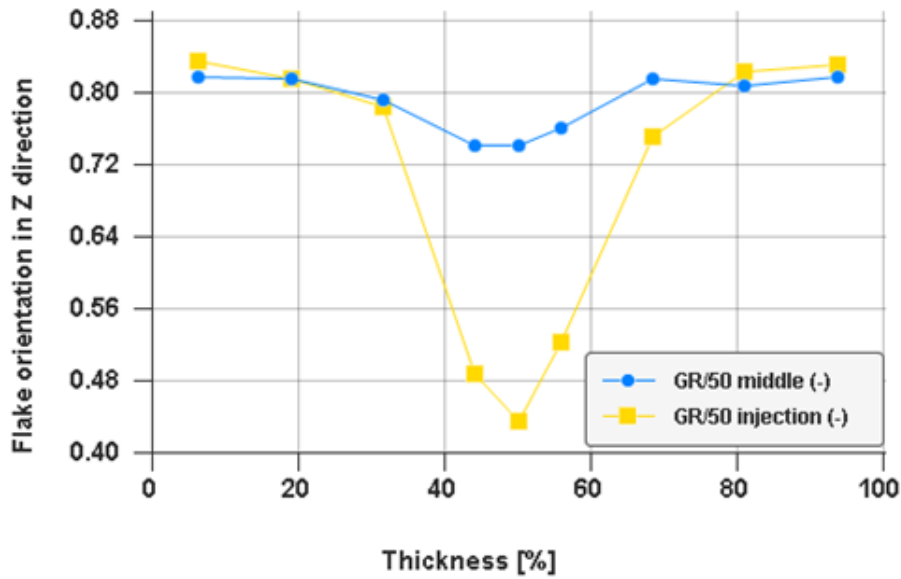


Figure 29. Through-thickness orientation for the middle and injection zones of the GR/50 1.47 mm bar.



Figure 30. Shear rate at the end of filling across the injection zone cross-section of the GR/50_{hv} sample of 1.47 mm thickness.

Shear stresses along the runner and bar at the end of the filling stage are given in Figure 31. These simulation results reveal that the shear stress varies along the bar length in the case of GR/50 and GR/70 (Figure 31-a to 31-d), contributing to the more contrasting LFA results between the middle and injection gate zone. On the other hand, for the GR/50_{hv} samples, the fast injection causes high shear rates and shear stresses in the runner (Figure 31-c), which result with a significant decrease in the viscosity. This, in turn, decreases the shear stress for the rest of the melt path, and therefore the shear stress along the injection molded bar is more uniform (Figure 31-e and 31-f). This aligns with the GR/50_{hv} results from the LFA analysis, where the middle and injection zone possess more similar thermal conductivities, and the IP thermal conductivity is even slightly higher near the injection region (Figure 23).

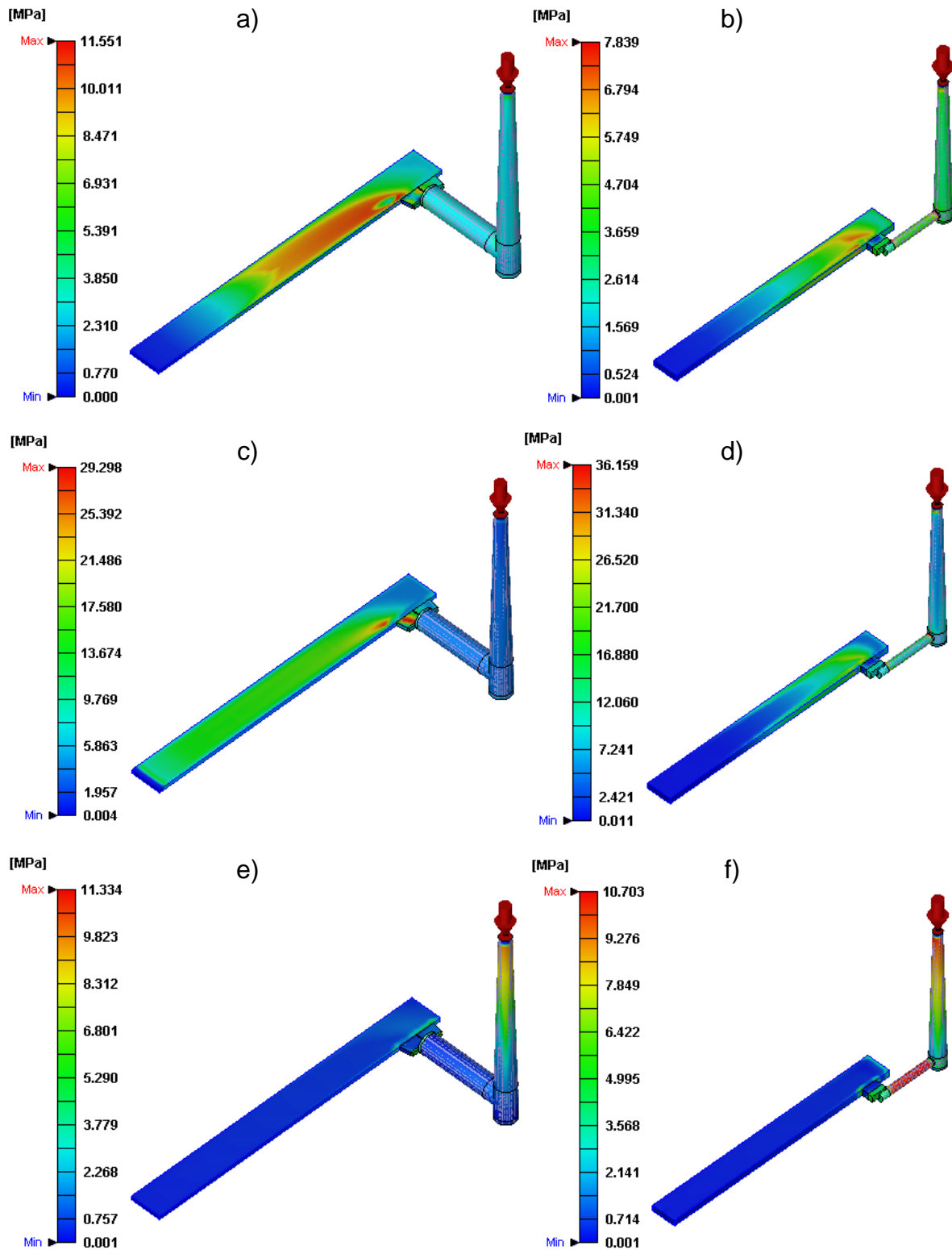


Figure 31. Shear stress distribution at end of filling for: a) GR/50 (1.47 mm); b) GR/50 (3.2 mm); c) GR/70 (1.47 mm); d) GR/70 (3.2 mm); e) GR/50_{hv} (1.47 mm); f) GR/50_{hv} (3.2 mm).

3.4. LFA simulation results

During the simulations, the key influencing factors for the end result were taken into consideration. It was found that the material properties (density, specific heat, conductivity), pulse duration (refers to the real pulse whose power is different from zero at the pulse width) and time steps used for the transient analysis affected the half-time obtained using the LFA simulations. The number of materials assigned by the macros also played a role, particularly the lower number of materials (higher tolerance) decreased the model accuracy. The heat flux, i.e. the amount of thermal power applied to the surface influenced only the temperature distribution by shifting it to higher values, but the half-time always remained same when considering the relative temperature rise. The 1 ms pulse shape approximations also did not show any significant difference between them. Neither changing the convection coefficient, nor whether it is assigned to the perimeter surfaces made a significant difference in the final curve. No convection conditions only slightly decreased the rate of the temperature rise. The generally small influence of the convection coefficient is likely attributed to the simple geometry and small size of the specimen, as well as the small temperature difference between the specimen and the surrounding. Decreasing the mesh size below the chosen size did not have a significant effect (not considering the computation time), but too rough of a mesh started to change the shape of LFA simulation curves so that there was less agreement with the experimental ones. Note that the rough mesh was only assessed for the isotropic case, and in the anisotropic model it would probably cause a more considerable difference.

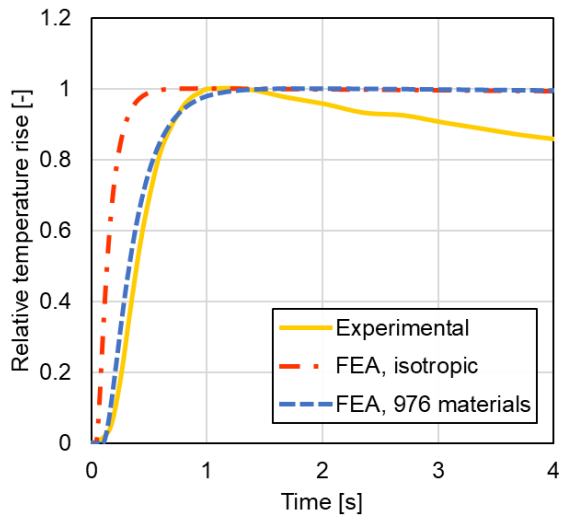
Figures 32-37 show the normalized temperature rise curves for the rear surface of LFA samples. Comparisons are given between the experimental results and computer simulations using the isotropic and anisotropic models. The number of materials contained in the material card of the anisotropic model for each sample is presented in the graph legends. It is evident that the LFA anisotropic simulation curves fit the experimentally obtained results very well. For all samples, the isotropic model resulted with a temperature rise that is too fast for the TP and too slow for the IP direction. Tables 12-14 give a closer look of the agreement between the experiment and LFA simulations. A material's thermal diffusivity using the laser flash method is computed by using the half-time from the output curve. Therefore, this parameter was extracted from each of the anisotropic model functions and used to calculate the thermal diffusivity and conductivity according to Equations 4 and 3. The results of these calculations reaffirmed the high accuracy of the model.

The highest percent error is 28.8%, obtained for the TP conductivity of the GR/50 sample representing the injection area of the 1.47 mm thick flame bar (Table 12). By looking at Table 12, it can be noticed that significantly higher deviations from the real case were obtained for the TP thermal conductivity of the thinner samples, which coincide with the experimental LFA measurements that produced the most unexpected results. Since the flame bars of two different thicknesses were made from the same compound, lower IP conductivity of 1.47 mm samples should correspond to a higher TP thermal conductivity with respect to the 3.2 mm samples. In the

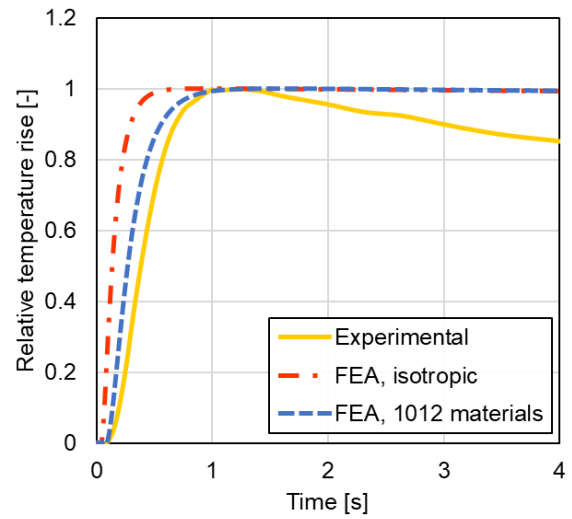
experimental results, GR/50 samples of 1.47 mm thickness measured lower conductivity in both directions. Furthermore, the outcome of LFA simulations was in line with predictions before starting the experimental work, i.e. higher IP thermal conductivity was obtained for the thinner injection molded bars due to higher flake orientation along the flow. This suggests that the graphite alignment along the flow direction might be overestimated by the software, and parameters such as the filler aspect ratio should be further adjusted. However, this may also mean that the origin of higher general conductivity in the 3.2 mm samples is the degree of dispersion, which is not taken into account in the exploited simulation models (Moldex3D considers the ideal case of no agglomeration). For the GR/70 composite, the anisotropic model proved highly accurate and all errors with respect to the experimental measurements are less than 9% (Table 13). The higher conductivity for the thinner samples obtained in this case matches the thesis assumptions and LFA measurements. For the GR/50_{hv}, the same discrepancies as in the case of Series 1 GR/50 occurred. However, the lowest percentage of error of only 0.7% was found for the IP thermal conductivity of the GR/50_{hv} sample cut from the middle part of a 1.47 mm thick bar (Table 14).

Although the experimental and anisotropic simulation LFA curves are very similar in the heating range, the real samples cool down faster after reaching the maximum temperature. Both isotropic and anisotropic models show only negligible temperature decrease of the top surface during the analysis time. This may be due to the omission of radiation heat transfer in the performed simulation runs [93]. Taking into consideration convection currents and Benard cells [108] by using a computational fluid dynamics (CFD) software may also have some effect. Nevertheless, this part of the curve is not an influential factor for what considers the determination of the LFA half-time, and subsequently, the thermal diffusivity and conductivity of the material.

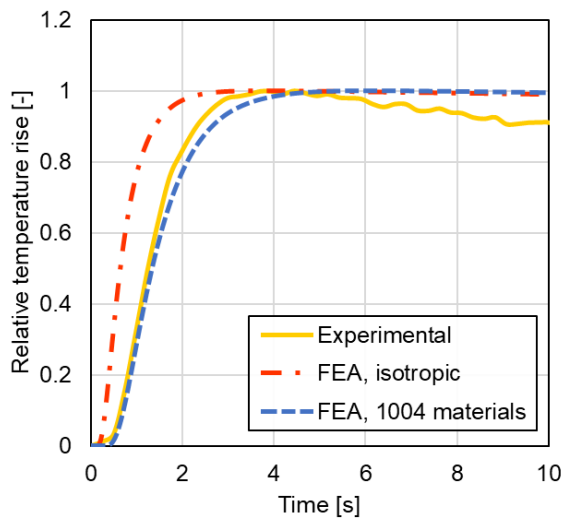
In order to further investigate and adapt its applicability, thermal analysis for different composite materials, geometries and loadings, could be carried out using this model. It can be expected that in these scenarios the relative influence of various parameters would change, so it is necessary to consider some possibilities for future adjustments. One of them is injection molding the materials into bars with another thickness, lower than 1.47 and 3.2 mm. LFA results from such samples could be useful for a more accurate extrapolation of K_{min} and K_{max} . In the current model, the directional thermal conductivity is a simple linear function of the specimen thickness because only two data points were considered (Figure 16). Adding thermal conductivity values for a thickness that is smaller than 1.47 mm would better represent the thermal conductivity trend when going to zero thickness. Another possibility for tuning the model is to use an average value for the thermal conductivity in place of the difference ($K_{max} - K_{min}$) in Equations 24-26.



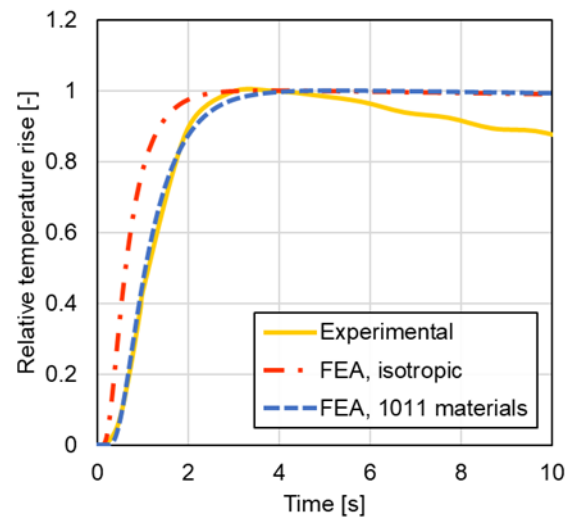
a)



b)



c)



d)

Figure 32. LFA results for GR/50 samples (TP): a) middle zone of 1.47 mm thick bar; b) injection zone of 1.47 mm thick bar; c) middle zone of 3.2 mm thick bar; d) injection zone of 3.2 mm thick bar.

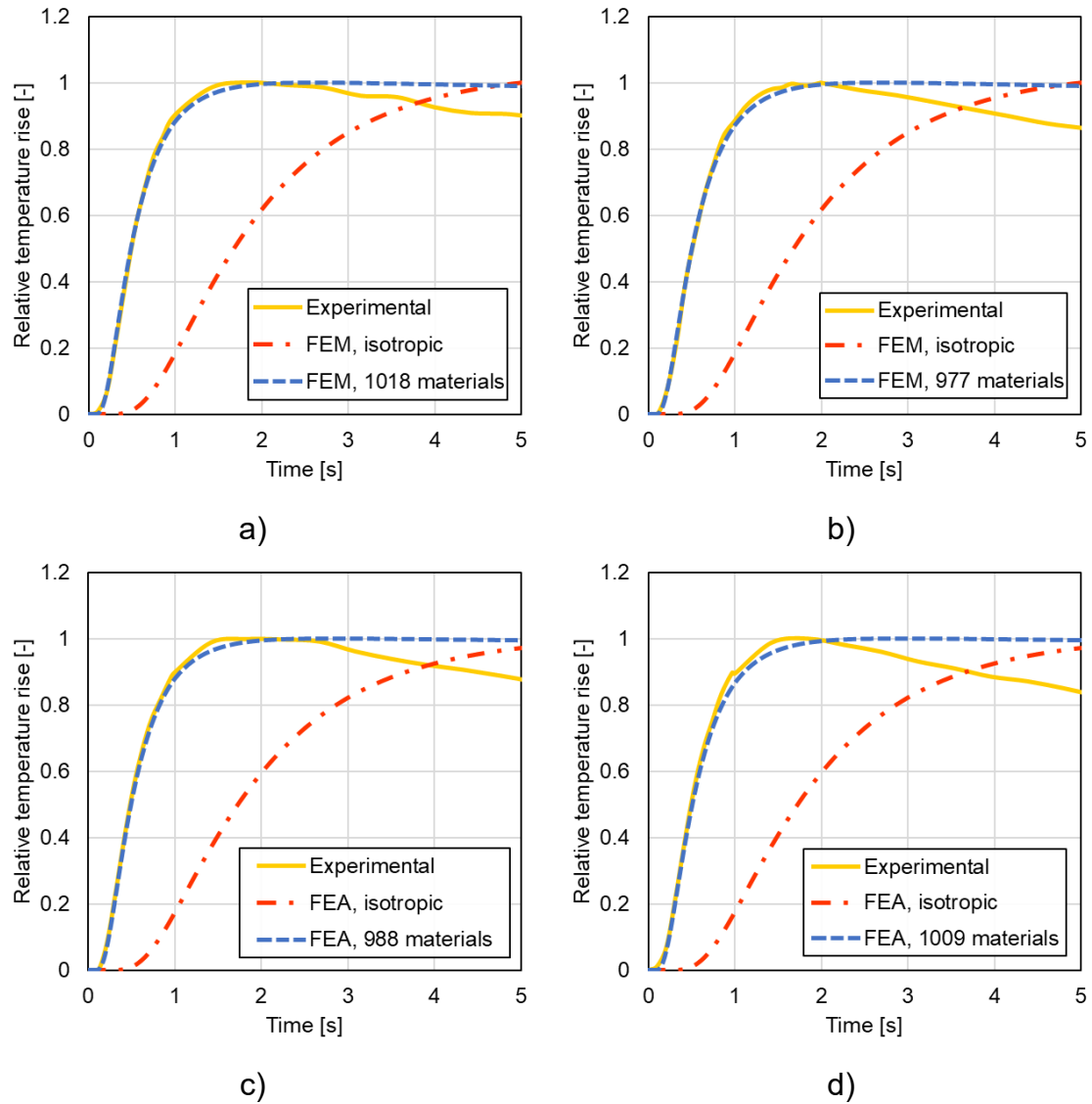


Figure 33. LFA results for GR/50 samples (IP): a) middle zone of 1.47 mm thick bar; b) injection zone of 1.47 mm thick bar; c) middle zone of 3.2 mm thick bar; d) injection zone of 3.2 mm thick bar.

Area	Sample thickness [mm]	Direction	α [mm ² /s]	κ [W/m°C]	Error [%]
Middle	1.47	TP	0.907	1.517	18.6
		IP	7.933	13.263	2.7
	3.20	TP	1.068	1.786	8.3
		IP	7.895	13.198	4.0
Near injection gate	1.47	TP	1.104	1.845	28.8
		IP	7.691	12.858	7.5
	3.20	TP	1.329	2.222	2.7
		IP	7.621	12.740	2.8

Table 12. Simulation results for the thermal diffusivity and conductivity of GR/50 samples with percentage error compared to experimental results.

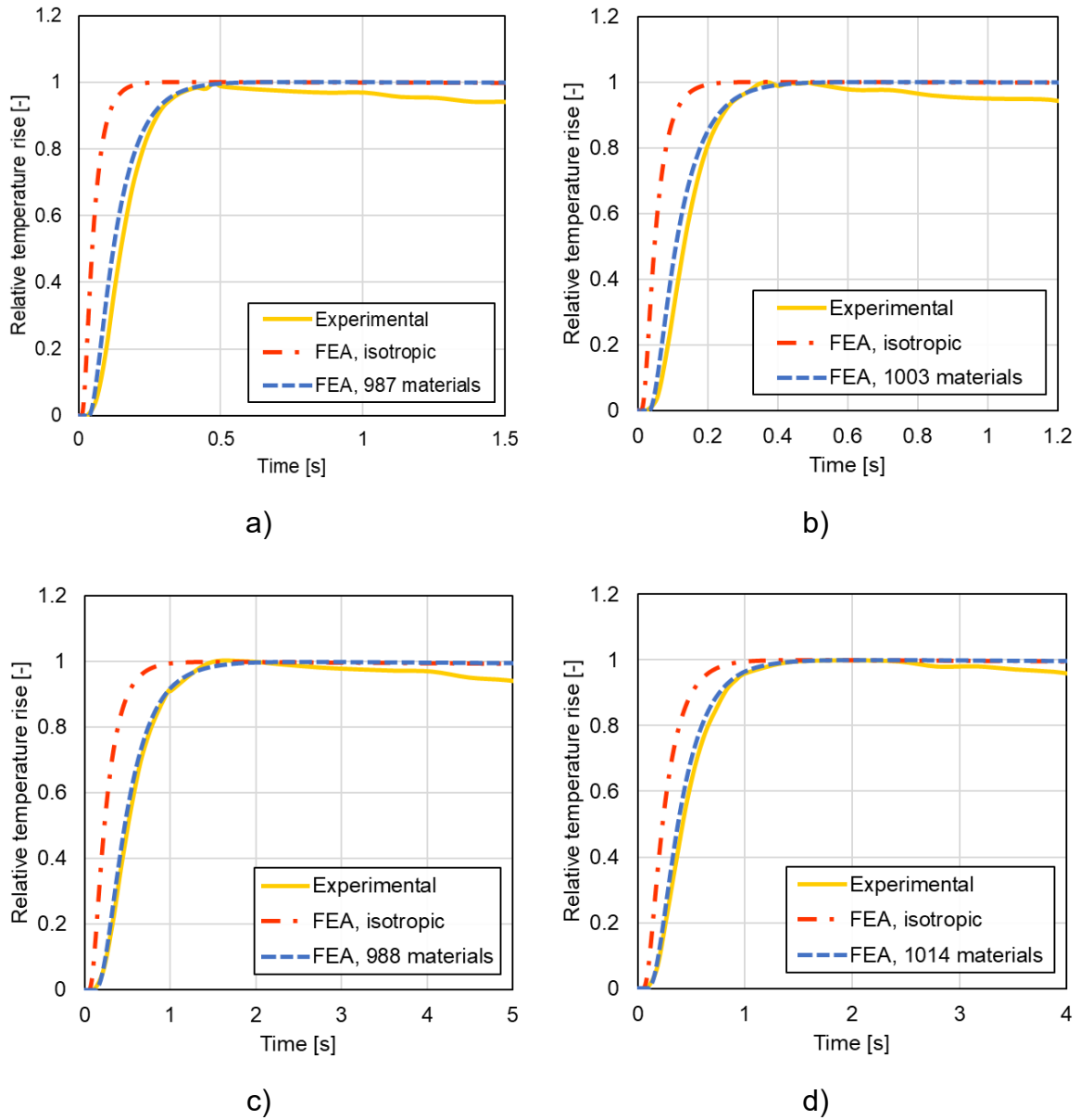


Figure 34. LFA results for GR/70 samples (TP): a) middle zone of 1.47 mm thick bar; b) injection zone of 1.47 mm thick bar; c) middle zone of 3.2 mm thick bar; d) injection zone of 3.2 mm thick bar.

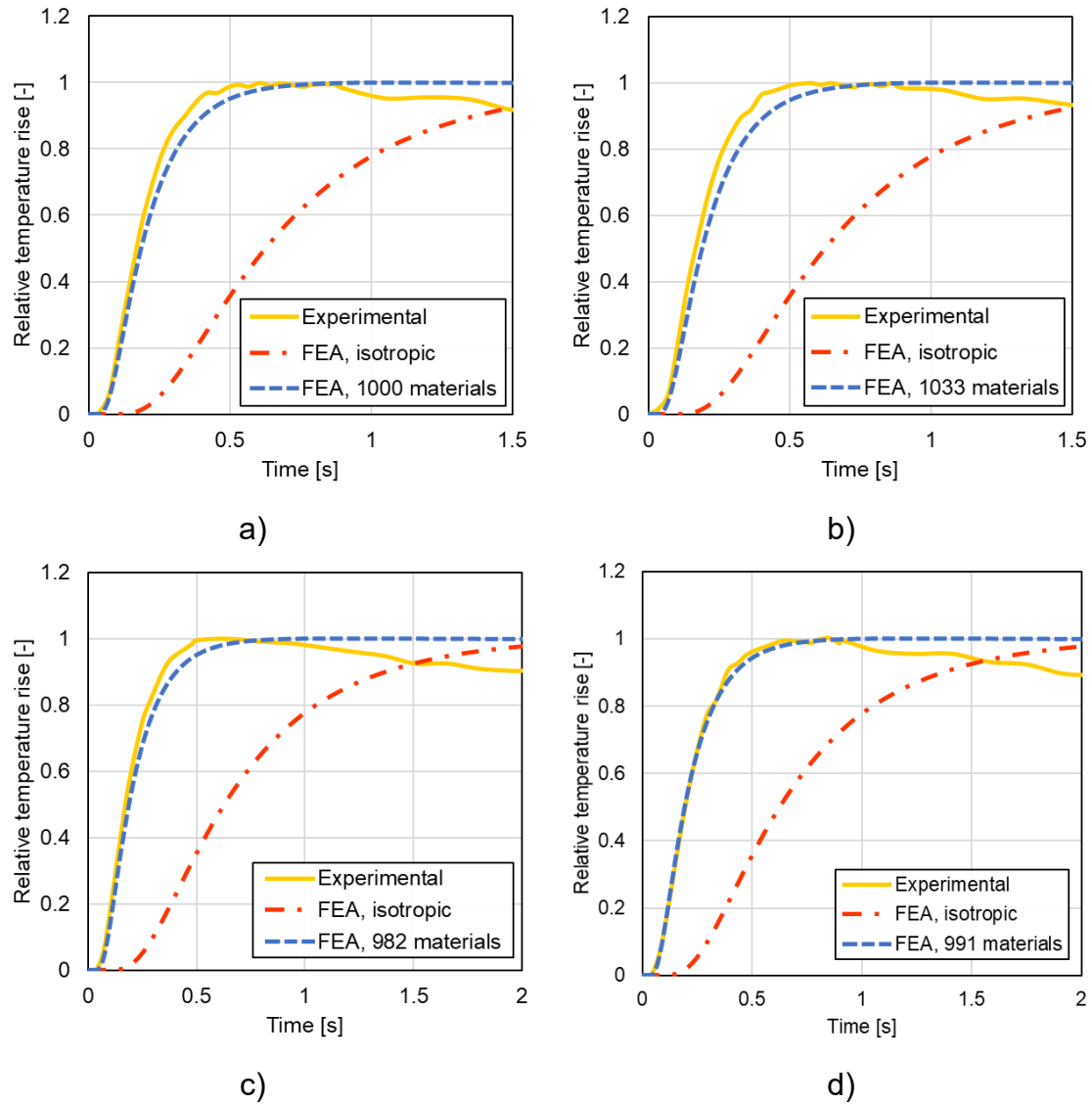
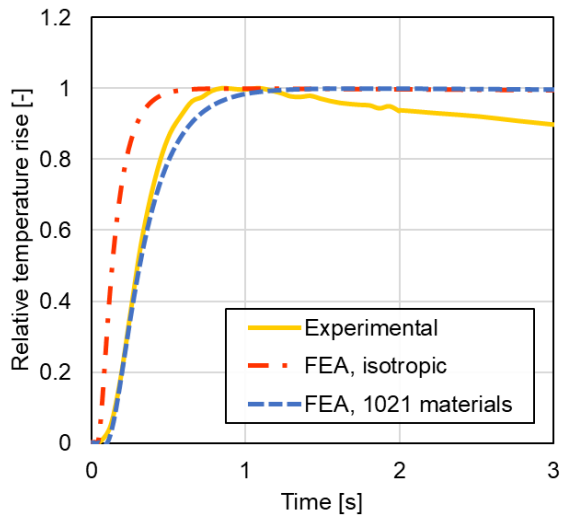


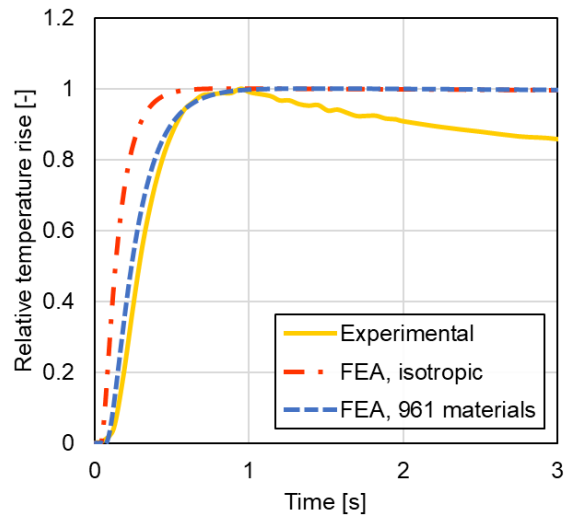
Figure 35. LFA results for GR/70 samples (IP): a) middle zone of 1.47 mm thick bar; b) injection zone of 1.47 mm thick bar; c) middle zone of 3.2 mm thick bar; d) injection zone of 3.2 mm thick bar.

Area	Sample thickness [mm]	Direction	α [mm ² /s]	κ [W/m°C]	Error [%]
Middle	1.47	TP	2.438	4.076	7.3
		IP	20.840	34.840	8.8
	3.20	TP	3.019	5.046	2.9
		IP	20.868	34.887	5.9
Near injection gate	1.47	TP	2.732	4.567	3.5
		IP	20.353	34.025	8.3
	3.20	TP	3.762	6.290	4.7
		IP	20.094	33.593	5.8

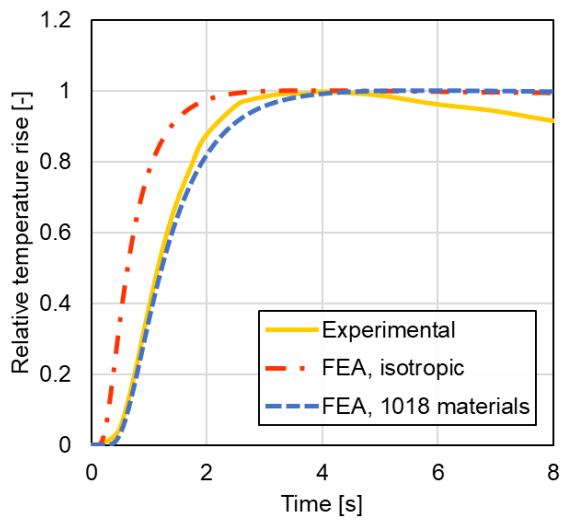
Table 13. Simulation results for the thermal diffusivity and conductivity of GR/70 samples with percentage of error compared to experimental results.



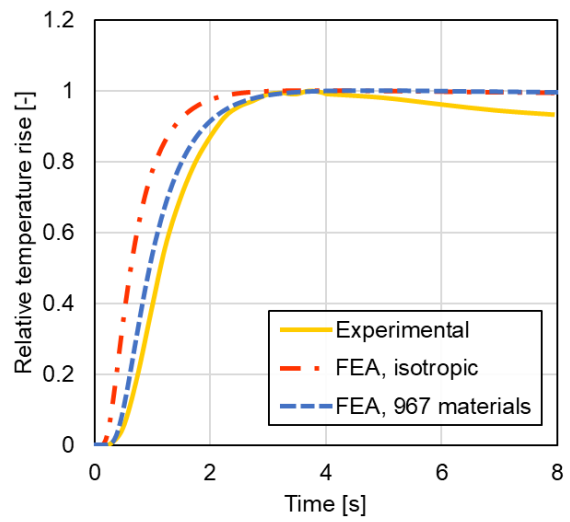
a)



b)



c)



d)

Figure 36. LFA results for GR/50_{hv} samples (TP): a) middle zone of 1.47 mm thick bar; b) injection zone of 1.47 mm thick bar; c) middle zone of 3.2 mm thick bar; d) injection zone of 3.2 mm thick bar.

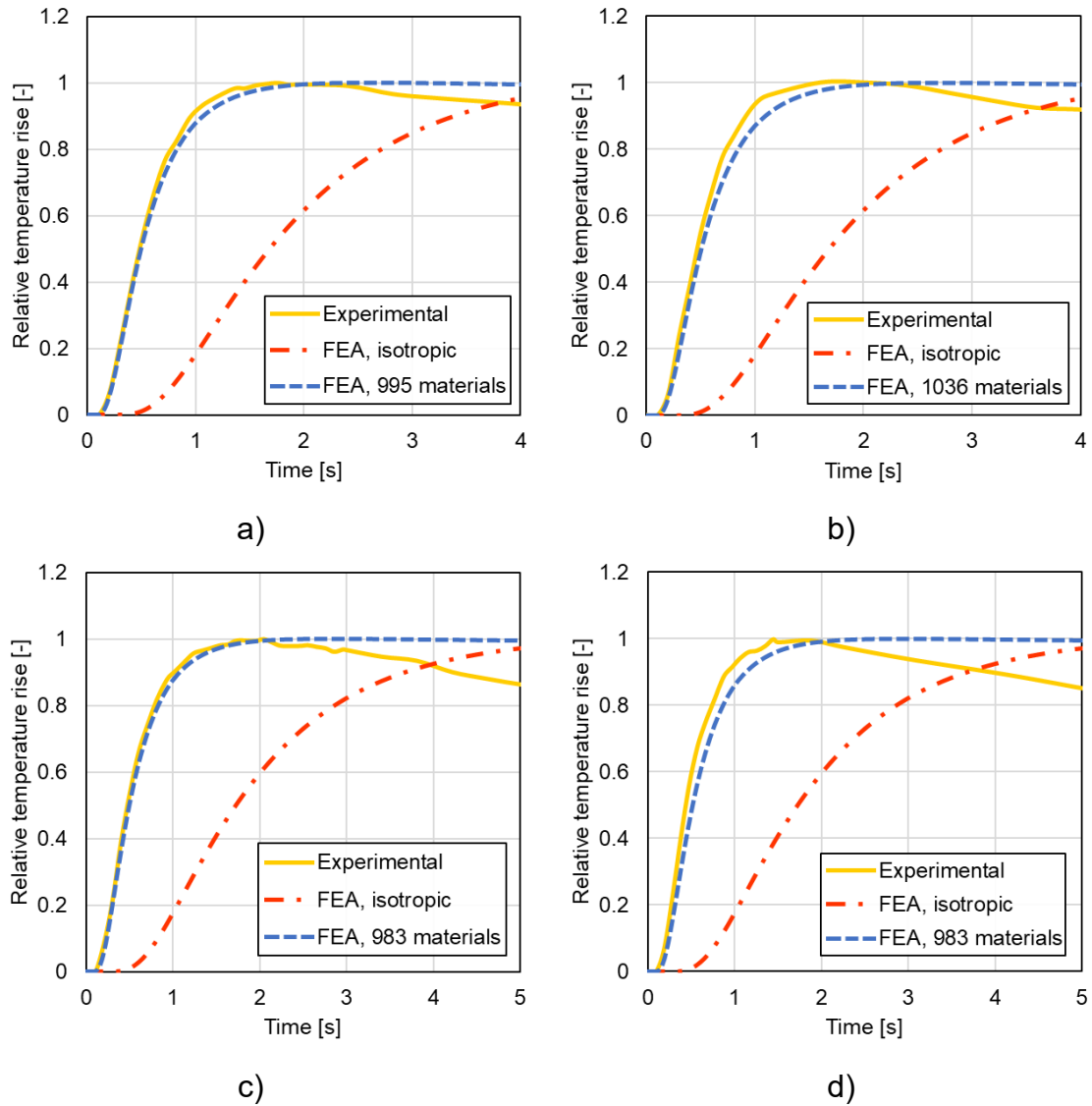


Figure 37. LFA results for GR/50_{hv} samples (IP): a) middle zone of 1.47 mm thick bar; b) injection zone of 1.47 mm thick bar; c) middle zone of 3.2 mm thick bar; d) injection zone of 3.2 mm thick bar.

Area	Sample thickness [mm]	Direction	α [mm ² /s]	κ [W/m°C]	Error [%]
Middle	1.47	TP	0.952	1.591	12.3
		IP	7.870	13.158	0.7
	3.20	TP	1.160	1.939	11.9
		IP	7.768	12.986	3.7
Near injection gate	1.47	TP	1.243	2.077	11.4
		IP	7.711	12.890	2.3
	3.20	TP	1.491	2.493	13.6
		IP	7.478	12.502	9.6

Table 14. Simulation results for the thermal diffusivity and conductivity of GR/50_{hv} samples with percentage error compared to experimental results.

Figure 38 shows a temperature cross-section of the TP (Figure 38-a and 38-b) and IP (Figure 38-c and 38-d) samples of GR/70 with 3.2 mm thickness during a simulation of the LFA. The laser pulse has partially propagated through the sample and the difference in the simulative temperature distribution between the isotropic and anisotropic model can be clearly seen. In all cases, the conditions at analysis time of 1.25 s, corresponding to increment 625, are represented. By considering the results regarding the accuracy of each model, the real temperature distributions in the samples at the given time is likely closer to the cases presented in Figure 38-b and 38-d.

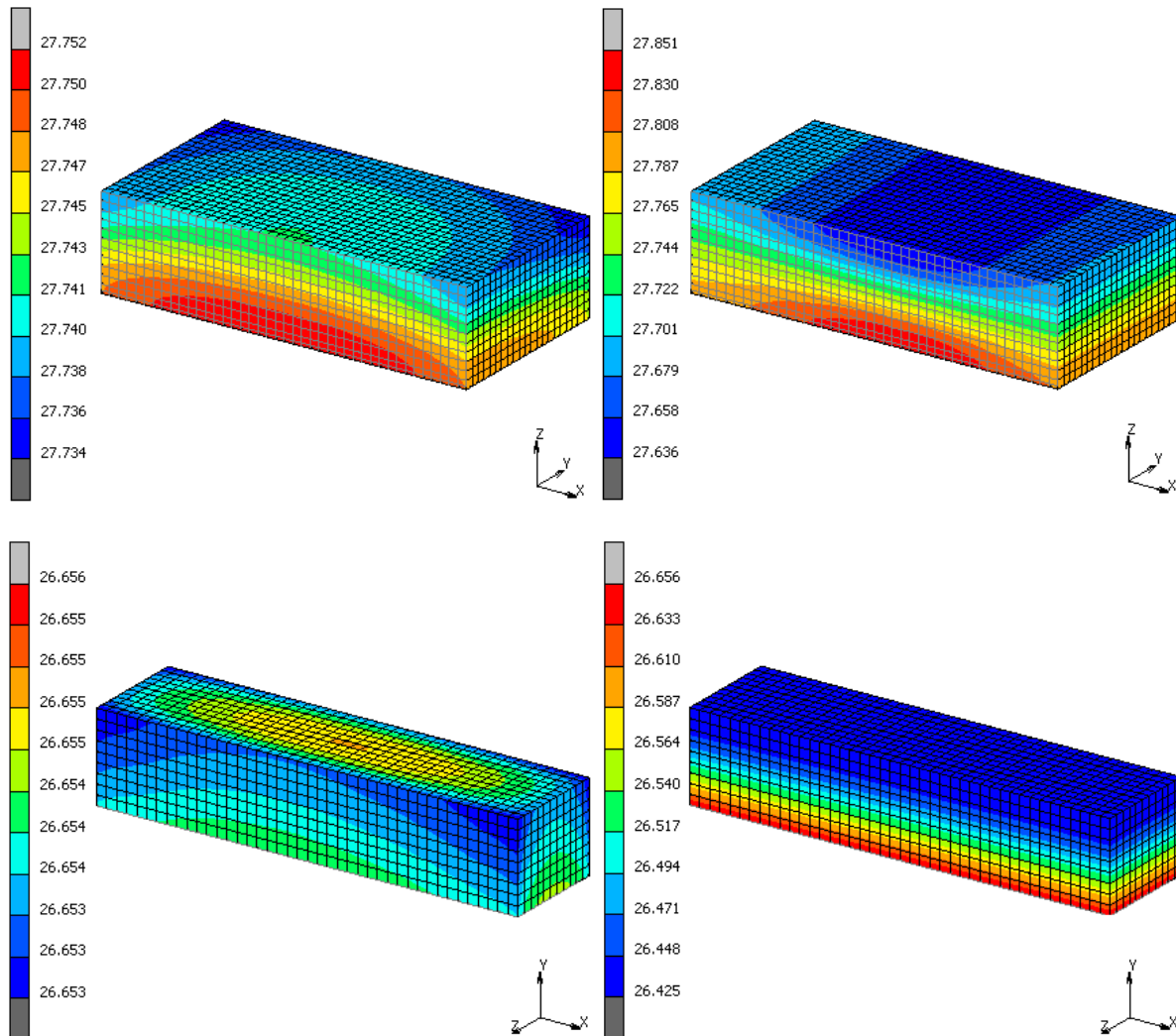
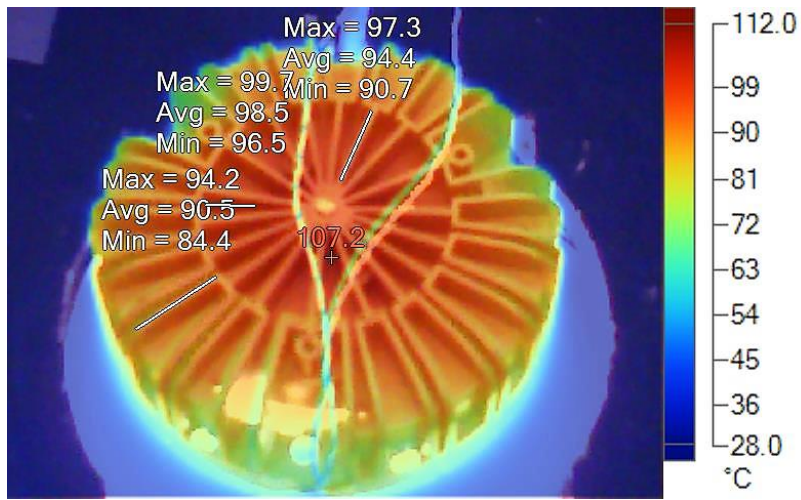


Figure 38. Cross section of temperature at 1.25 s calculated by FEA for 3.2 mm thick GR/50 samples: a) isotropic model, TP measurement; b) anisotropic model, TP measurement; c) isotropic model, IP measurement; d) anisotropic model, IP measurement.

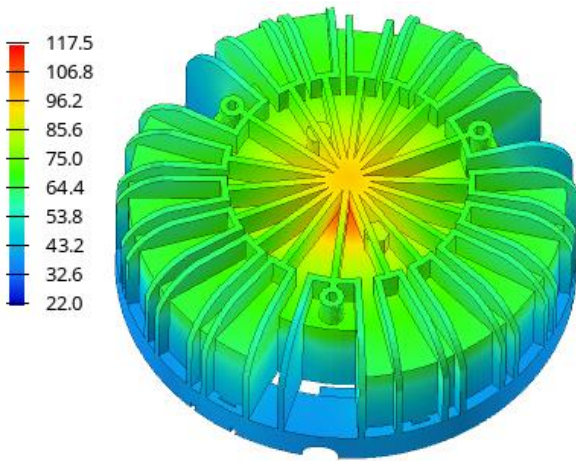
3.5. Case study

Figures 39-a, 40-a and 41-a show the results from the IR camera temperature evaluation, kindly provided by Whitecroft Lighting. Details for the minimum, maximum and average temperature of each measurement are shown in Table 15. Comparing the experimental measurements to the steady state thermal analysis, it can be noticed that the results are rather different with respect to the LFA case. From the first series of simulations performed for light intensity of 5000 lm (Figure 20), it is very difficult to assess which of the models is most accurate with respect to the real temperature distribution. The main problem in all cases is that the temperature tends to be too high in the central part of the heat sink, and too low around the circumference. The finite element analysis approximately closest to the real temperature distribution was obtained by using the isotropic model with GR/50 conductivity of 10 W/m°C (Figure 39-d). On the other hand, using the anisotropic model with the same correction factor used in the LFA simulations (Figure 39-c) resulted with the biggest temperature gradient between the center and external parts of the heat sink. The temperature of the PCB was also very high in this case (not shown here). Furthermore, the results using an isotropic filler assumption (Figure 39-e) were more approaching to the real case, even though it is known that graphite is an anisotropic filler. The most probable explanation for the inaccuracy of the anisotropic model in the case study is the use of a software that does not support computational fluid dynamics (CFD). For more complex parts, and especially for heat sinks, it is very difficult to perform manual calculations for the convection coefficient. The convection coefficient for the fins increases with their surface area, but can also significantly decrease if the spacing between them is too small. The situation gets more complex considering the V-shaped fins with a radial distribution present in this case. Moreover, the number of nodes along the thickness is likely too low for an accurate thermal analysis, as well as an accurate prediction of flake alignment. Probably by increasing the through-thickness element count from two to four or six, the thermal dissipation and filler orientation will be better captured. Therefore, although the anisotropic model exploited through the Excel macros shows great promise for increased accuracy of thermal analysis, it needs further adjustments for more complex geometries (some of which are discussed in Section 3.4). For these cases also the use of a CFD software is recommended.

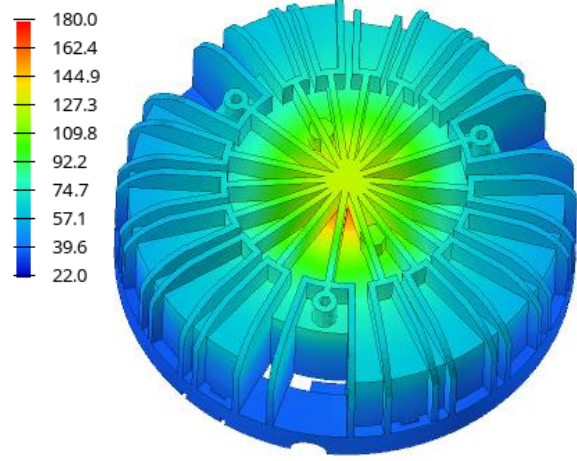
Since the isotropic model with thermal conductivity of 10 W/m°C and the anisotropic model with an isotropic assumption for the filler were determined as most similar to the real case, they were used in the steady-state thermal analysis with the remaining two light intensities. The results for 3000 and 2000 lm are shown in Figures 40 and 41, however the conclusion remains the same.



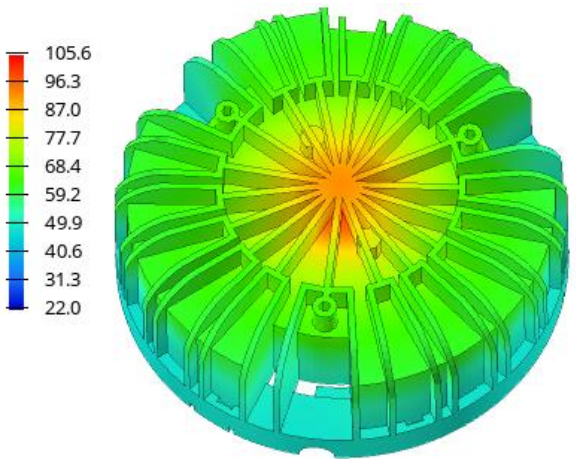
a)



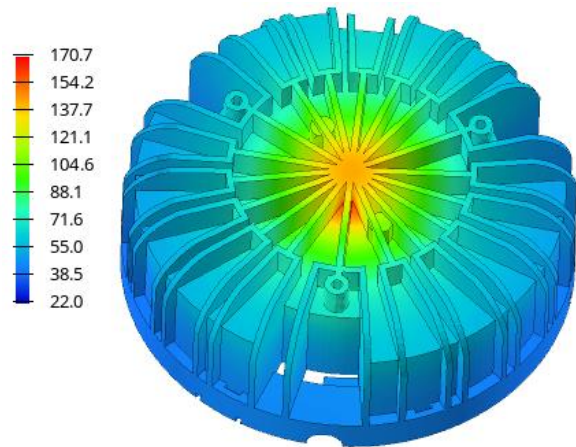
b)



c)

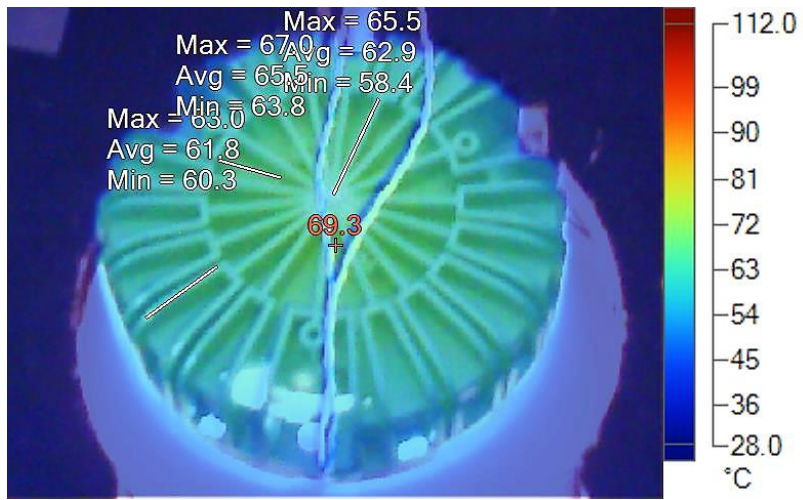


d)



e)

Figure 39. Steady-state thermal distribution [°C] of heat sink for 5000 lm LED: a) experimental; b) isotropic model ($\kappa=3.74$ W/m°C); c) anisotropic model (0.4 filler anisotropy correction); d) isotropic model ($\kappa=10$ W/m°C); e) anisotropic model (isotropic filler).



a)

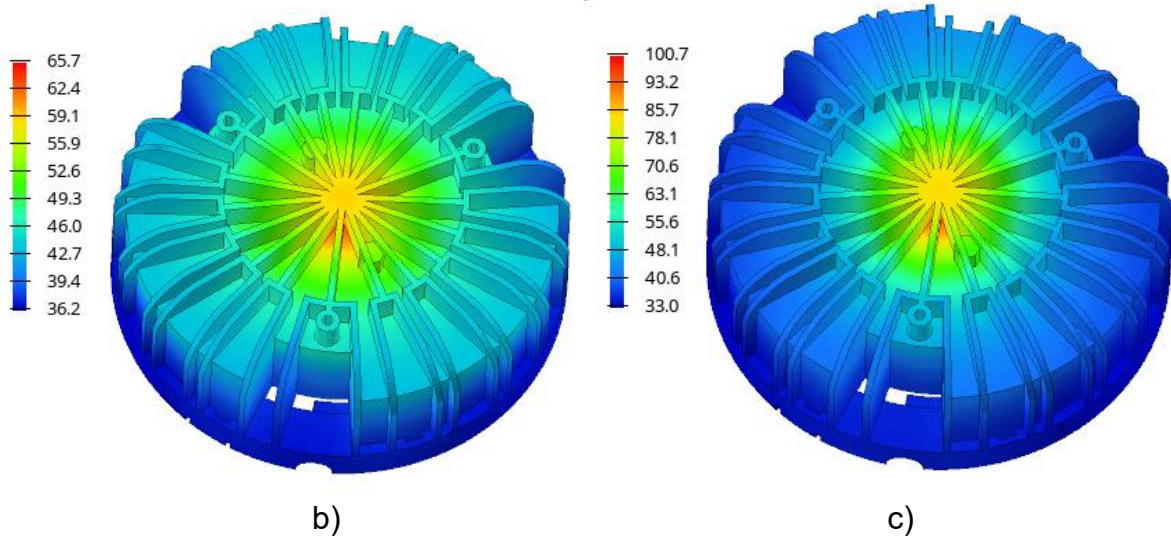
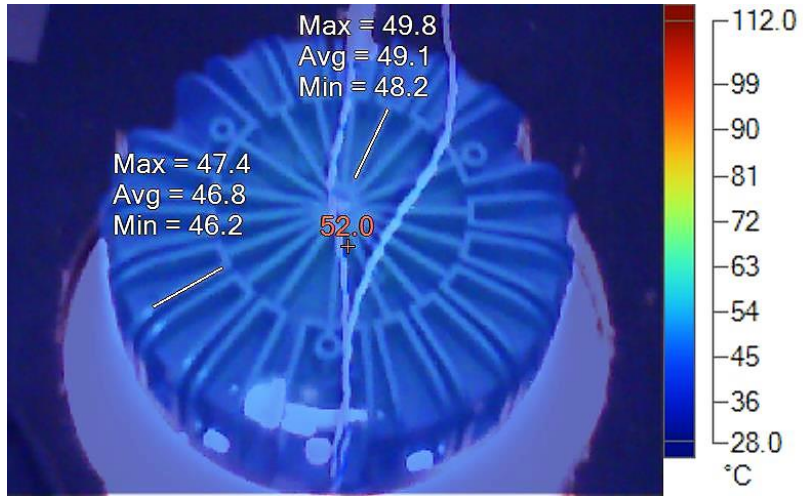
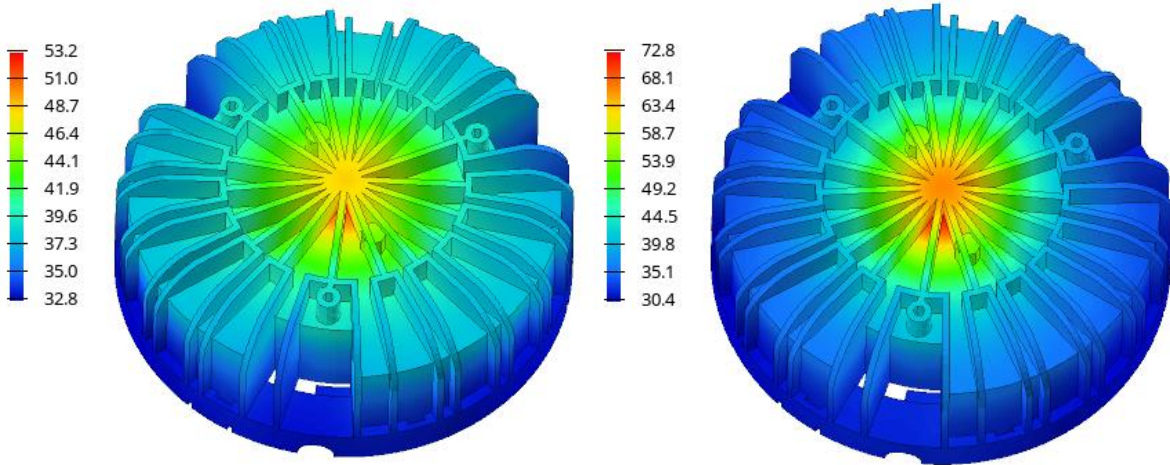


Figure 40. Steady-state thermal distribution [°C] of heat sink for 3000 lm LED: a) experimental; b) isotropic model ($\kappa=10$ W/m°C); c) anisotropic model (isotropic filler).



a)



b)

c)

Figure 41. Steady-state thermal distribution [°C] of heat sink for 2000 lm LED: a) experimental; b) isotropic model ($\kappa=10 \text{ W/m}^\circ\text{C}$); c) anisotropic model (isotropic filler).

	5000 lm	3000 lm	2000 lm
Maximum temperature [°C]	107.2	69.3	52.0
Minimum temperature [°C]	26.7	27.2	25.3
Average temperature [°C]	60.3	45.4	37.3

Table 15. Details for the IR camera results.

Conclusions and future work

In the present thesis, the accuracy of an anisotropic model for the thermal conductivity of injection molded plastic compounds was evaluated. The study was organized in two parts: laboratory experimental work and computer simulations using said model. The results of the two were then compared. All work was done with the company LATI, where two proprietary PA6-based compounds were chosen as subjects of the study. The compounds, named as GR/50 and GR/70 contain different amounts of graphite as a thermally conductive filler, 50 wt% and 70 wt%, respectively.

The experimental part, carried out in the LATI R&D department, comprised injection molding of the compounds, characterization, and LFA for determining their thermal diffusivity and conductivity. With the injection molding, standardized bars of two different thicknesses (1.47 mm and 3.2 mm) were obtained, under the assumption that the higher shear stresses in the thinner mold cavity should lead to a stronger filler alignment along the flow, and in turn, to a higher IP thermal conductivity. This was based on previous company research for a number of compounds, where the results suggested that the cavity thickness has a deciding effect on filler orientation and directional thermal conductivity, whereas the injection molding parameters do not have a significant influence.

The GR/50 and GR/70 materials were characterized using various techniques, and the results showed that the increased graphite content contributes to a higher density, stiffness and thermal stability, while decreasing the ductility and only slightly decreasing the tensile strength. SEM observation of the cross-section of a 1.47 mm thick GR/50 bar revealed the typical skin-core layers of components produced by injection molding. The microstructure was compact, with well-dispersed graphite flakes and no visible agglomeration that can affect the local thermal conductivity. Furthermore, the flake alignment was stronger in the middle area of the bar, while flakes were oriented more randomly in the region near the injection gate, which was in line with expectations.

Regarding the thermal conductivity, the results of the GR/50 LFA were different than what was anticipated based on the previous study. Namely, the measured thermal conductivity for the thicker samples was higher in both TP and IP directions. The average measured values were: 1.279 W/m°C (TP) and 12.913 W/m°C (IP) for the 1.47 mm samples, and 1.948 W/m°C (TP) and 13.753 W/m°C (IP) for 3.2 mm samples. This can be potentially explained with the effect of cavity thickness on the relative size of the skin (in-plane filler orientation) and core (random-in-plane filler orientation) layer; the higher shear rate for the 1.47 mm samples could cause more shear thinning, and the flattening of the velocity profile forms a wider core region where the orientation is random-in-plane. Furthermore, there could be a possible difference in the degree of graphite dispersion between the samples of different thickness. The presumed higher shear stress in the 1.47 mm cavity may separate the flakes more efficiently and increase the number of PA6/graphite interfaces, which has a negative effect on thermal transport. This reasoning could be more probable, since 1.47 mm samples measured lower values in both directions, suggesting that there is another

influencing factor besides graphite orientation. Results for thermal conductivity with respect to the position along the bar conform to expectations, and the more random filler orientation in the injection region increased the TP and decreased the IP conductivity values compared to the middle region.

The thermal performance of GR/70 samples aligned with the hypothesis, therefore higher IP thermal conductivity was recorded for the 1.47 mm bars (38.199 W/m°C) compared to the 3.2 mm thick bars (37.055 W/m°C). Consequentially, the average TP values for the thinner and thicker sample were 3.798 and 4.905 W/m°C, respectively. In this case, the faster cooling due to the higher graphite content dominates over the increased shear thinning in the 1.47 mm samples, thus increasing the size of the highly oriented skin layer. Furthermore, due to the higher viscosity and higher graphite loading of the GR/70 melt, the flakes are not likely to be fully dispersed, thus they form more contact points and agglomerates even in the 1.47 mm thick sample. The comparison between the middle and injection zone samples is the same as in the GR/50 case and aligns with expectations.

The GR/50 composite was also injection molded with a higher velocity (GR/50_{hv}), in an attempt to match the shear rate of the GR/70 samples and obtain a more IP oriented microstructure in the thinner bars. While the thermal conductivity of the 1.47 mm bar did show a slight increase in both directions, the general trend with respect to the 3.2 mm samples remained the same. Regarding the 3.2 mm thick sample, the higher injection rate decreased the IP thermal conductivity due to the flatter velocity profile bringing the high shear region closer to the walls and increasing the size of the core region. An interesting result for the GR/50_{hv} samples was that the thermal conductivities of the middle and injection zones were closer together, with the IP results even suggesting higher flake orientation in the area near the injection gate (13.832 compared to 13.485 W/m°C).

For the second part of the work, finite element analyses were performed with the LATI Technical Assistance department. This segment consisted of simulations of the injection molding process, the laser flash method and a case study of a real component.

Injection molding simulations were part of the assessing the anisotropic model accuracy, but they were also utilized to evaluate the potential factors that contributed to the measured values of the directional thermal conductivity. The flake orientation cross-section generated by the software was very similar to the SEM images. Furthermore, results suggested that the relative core size of the GR/70 samples of 1.47 mm thickness was smaller than in the case of GR/50 and GR/50_{hv}, likely due to the faster cooling and higher viscosity. Comparing the GR/70 bars of 1.47 to 3.2 mm thickness, the FEA confirms the increased core area and flatter velocity profile. The IP filler orientation in the core layer was least pronounced for the GR/50_{hv} compound, due to the lower shear rate in the center plane which was found in the simulations. Regarding the differences in microstructural orientation between the central and near-injection gate samples, computational analyses are in line with LFA and SEM investigations. The injection cross section also shows lower shear rate in the center of

the sample, contributing to the lower flake orientation. Simulation results for the shear stress distribution in the runner and cavity at the end of filling suggest that the possible reason for the closer thermal conductivity values between middle and injection regions for the GR/50_{hv} could be the more uniform shear stress along the bar.

The accuracy of the anisotropic thermal conductivity model was studied by running finite element simulations of the LFA and comparing the obtained thermal conductivity values with the instrumental ones. Throughout the thermal transient analyses done for this purpose, it was found which parameters have a significant influence on the simulative thermal diffusivity and conductivity (material properties, tolerance used for the anisotropic model, pulse duration, time steps, mesh size, adiabatic conditions). The temperature rise curves obtained by isotropic LFA simulations were overestimating the TP and underestimating the IP rate of heat transfer. On the other hand, the anisotropic model showed a very good agreement with the experimental curves. The highest percentage errors for the thermal conductivity values (28.8% and 18.6%) coincided with the samples that also displayed the most unexpected experimental results. The lowest error percentage was only 0.7%. For the GR/50, the simulation results were in line with the pre-experimental anticipations that the thinner bars would display higher thermal conductivity, suggesting that the software might be overestimating the flake orientation for the thinner samples or that the origin of the instrumental results might indeed be the degree of flake dispersion. For the GR/70, all error percentages were below 9%. By observing the temperature cross-section at a fixed time of the simulation, clear differences can be seen between the two models.

Finally, the anisotropic model was used for a steady state analysis of a heatsink for downlights, considering three different LED intensities (2000, 3000 and 5000 lm). Experimental thermography results were kindly provided by Whitecroft Lighting. However, the simulations generally resulted with a temperature that is too high in the center of the heatsink (near the LED PCB) and too low around the perimeter, compared to the instrumental values. Furthermore, the anisotropic model that showed a very good fit for the LFA experimental results did not perform as good in this case. In fact, the FEA results that most resembled the measured temperature distribution were for an isotropic model with an approximated thermal conductivity of 10 W/m°C (previously determined by LATI Technical Assistance as best fit for thermal analysis).

In conclusion, the investigated model for determining the anisotropic thermal conductivity of injection molded composites shows great promise for accurate simulation of material behavior. However, it needs to be further tuned for use in more complex geometries, where an accurate estimation of convection coefficients and refined meshing are required. For the former, a use of CFD software is also recommended. For the future, thermal analysis of different composites, geometries and loading cases is suggested. Some considerations for adjusting the model are: a more accurate determination of the K_{min} and K_{max} , using the average thermal conductivity in the computation of the thermal conductivity tensor, and adjusting the filler aspect ratio for the injection molding simulations.

Bibliography

- [1] S. Li *et al.*, “High thermal conductivity in cubic boron arsenide crystals,” *Science*, 2018, doi: 10.1126/science.aat8982.
- [2] Z. Han and A. Fina, “Thermal conductivity of carbon nanotubes and their polymer nanocomposites: A review,” *Progress in Polymer Science (Oxford)*. 2011, doi: 10.1016/j.progpolymsci.2010.11.004.
- [3] R. W. Lewis, P. Nithiarasu, and K. N. Seetharamu, *Fundamentals of the Finite Element Method for Heat and Fluid Flow*, vol. 3. 2005.
- [4] LATI, “Laticonther thermally conductive thermoplastic compounds.” .
- [5] J.M. Ziman, *Electrons and Phonons: The Theory of Transport Phenomena in Solids*. 2001.
- [6] P. G. Klemens, “Thermal Conductivity and Lattice Vibrational Modes,” *Solid State Physics - Advances in Research and Applications*, 1958, doi: 10.1016/S0081-1947(08)60551-2.
- [7] X. Huang, P. Jiang, and T. Tanaka, “A review of dielectric polymer composites with high thermal conductivity,” *IEEE Electrical Insulation Magazine*, vol. 27, no. 4, pp. 8–16, 2011, doi: 10.1109/MEI.2011.5954064.
- [8] W. D. Callister and D. G. Rethwisch, *Fundamentals of Materials Science and Engineering an integrated approach*. 2012.
- [9] Y. Guo, K. Ruan, X. Shi, X. Yang, and J. Gu, “Factors affecting thermal conductivities of the polymers and polymer composites: A review,” *Composites Science and Technology*, vol. 193, no. December 2019, p. 108134, 2020, doi: 10.1016/j.compscitech.2020.108134.
- [10] C. Huang, X. Qian, and R. Yang, “Thermal conductivity of polymers and polymer nanocomposites,” *Materials Science and Engineering R: Reports*, vol. 132. pp. 1–22, 2018, doi: 10.1016/j.mser.2018.06.002.
- [11] S. Shen, A. Henry, J. Tong, R. Zheng, and G. Chen, “Polyethylene nanofibres with very high thermal conductivities,” *Nature Nanotechnology*, 2010, doi: 10.1038/nnano.2010.27.
- [12] A. A. Askadskii, M. D. Petunova, and V. A. Markov, “Calculation scheme for the evaluation of polymer thermal conductivity,” *Polymer Science - Series A*, 2013, doi: 10.1134/S0965545X13090010.
- [13] T. Xiao, X. Fan, D. Fan, and Q. Li, “High thermal conductivity and low absorptivity/ emissivity properties of transparent fluorinated polyimide films,” *Polymer Bulletin*, 2017, doi: 10.1007/s00289-017-1974-6.
- [14] T. Zhang, X. Wu, and T. Luo, “Polymer nanofibers with outstanding thermal

- conductivity and thermal stability: Fundamental linkage between molecular characteristics and macroscopic thermal properties,” *Journal of Physical Chemistry C*, 2014, doi: 10.1021/jp5051639.
- [15] H. Ma and Z. Tian, “Effects of polymer chain confinement on thermal conductivity of ultrathin amorphous polystyrene films,” *Applied Physics Letters*, 2015, doi: 10.1063/1.4929426.
- [16] T. Zhang and T. Luo, “Role of Chain Morphology and Stiffness in Thermal Conductivity of Amorphous Polymers,” *Journal of Physical Chemistry B*, 2016, doi: 10.1021/acs.jpcc.5b09955.
- [17] Z. Guo *et al.*, “Tuning the thermal conductivity of solar cell polymers through side chain engineering,” *Physical Chemistry Chemical Physics*, 2014, doi: 10.1039/c4cp00393d.
- [18] H. Ma and Z. Tian, “Effects of polymer topology and morphology on thermal transport: A molecular dynamics study of bottlebrush polymers,” *Applied Physics Letters*, 2017, doi: 10.1063/1.4976946.
- [19] L. Zhang, M. Ruesch, X. Zhang, Z. Bai, and L. Liu, “Tuning thermal conductivity of crystalline polymer nanofibers by interchain hydrogen bonding,” *RSC Advances*, 2015, doi: 10.1039/c5ra18519j.
- [20] G. Kikugawa, T. G. Desai, P. Keblinski, and T. Ohara, “Effect of crosslink formation on heat conduction in amorphous polymers,” *Journal of Applied Physics*, 2013, doi: 10.1063/1.4813505.
- [21] X. Xie *et al.*, “High and low thermal conductivity of amorphous macromolecules,” *Physical Review B*, 2017, doi: 10.1103/PhysRevB.95.035406.
- [22] D. M. Bigg, “Thermal conductivity of heterophase polymer compositions,” *Advances in Polymer Science*. 1995, doi: 10.1007/bfb0021279.
- [23] J. Hansson, T. M. J. Nilsson, L. Ye, and J. Liu, “Novel nanostructured thermal interface materials : a review,” *International Materials Reviews*, vol. 6608, no. 63:1, pp. 22–45, 2018, doi: 10.1080/09506608.2017.1301014.
- [24] S. Bordbar, M. Rezaeizadeh, and A. Kaviani, “Improving thermal conductivity and corrosion resistance of polyurea coating on internal tubes of gas heater by nano silver,” *Progress in Organic Coatings*, 2020, doi: 10.1016/j.porgcoat.2020.105722.
- [25] I. L. Ngo, S. Jeon, and C. Byon, “Thermal conductivity of transparent and flexible polymers containing fillers: A literature review,” *International Journal of Heat and Mass Transfer*, vol. 98, pp. 219–226, 2016, doi: 10.1016/j.ijheatmasstransfer.2016.02.082.
- [26] Y. Yoo, H. L. Lee, S. M. Ha, B. K. Jeon, J. C. Won, and S. G. Lee, “Effect of

- graphite and carbon fiber contents on the morphology and properties of thermally conductive composites based on polyamide 6,” *Polymer International*, 2014, doi: 10.1002/pi.4534.
- [27] Y. P. Mamunya, V. V. Davydenko, P. Pissis, and E. V. Lebedev, “Electrical and thermal conductivity of polymers filled with metal powders,” *European Polymer Journal*, 2002, doi: 10.1016/S0014-3057(02)00064-2.
- [28] X. Li, W. Park, Y. P. Chen, and X. Ruan, “Effect of particle size and aggregation on thermal conductivity of metal-polymer nanocomposite,” *Journal of Heat Transfer*, 2017, doi: 10.1115/1.4034757.
- [29] A. S. Luyt, J. A. Molefi, and H. Krump, “Thermal, mechanical and electrical properties of copper powder filled low-density and linear low-density polyethylene composites,” *Polymer Degradation and Stability*, 2006, doi: 10.1016/j.polymdegradstab.2005.09.014.
- [30] S. Wang, Y. Cheng, R. Wang, J. Sun, and L. Gao, “Highly thermal conductive copper nanowire composites with ultralow loading: Toward applications as thermal interface materials,” 2014, doi: 10.1021/am500009p.
- [31] A. R. J. Hussain, A. A. Alahyari, S. A. Eastman, C. Thibaud-Erkey, S. Johnston, and M. J. Sobkowicz, “Review of polymers for heat exchanger applications: Factors concerning thermal conductivity,” *Applied Thermal Engineering*, vol. 113, pp. 1118–1127, 2017, doi: 10.1016/j.applthermaleng.2016.11.041.
- [32] W. Zhou, S. Qi, Q. An, H. Zhao, and N. Liu, “Thermal conductivity of boron nitride reinforced polyethylene composites,” *Materials Research Bulletin*, 2007, doi: 10.1016/j.materresbull.2006.11.047.
- [33] Z. Liu, B. Wu, and M. Gu, “Effect of hydrolysis of AlN particulates on corrosion behavior of Al/AlNp composite in neutral chloride solution,” *Composites Part A: Applied Science and Manufacturing*, 2007, doi: 10.1016/j.compositesa.2006.01.016.
- [34] K. Sato *et al.*, “Thermally conductive composite films of hexagonal boron nitride and polyimide with affinity-enhanced interfaces,” *Journal of Materials Chemistry*, 2010, doi: 10.1039/b924997d.
- [35] S. N. Leung *et al.*, “Analytical modeling and characterization of heat transfer in thermally conductive polymer composites filled with spherical particulates,” *Composites Part B: Engineering*, 2013, doi: 10.1016/j.compositesb.2012.10.001.
- [36] Z. Han, J. W. Wood, H. Herman, C. Zhang, and G. C. Stevens, “Thermal properties of composites filled with different fillers,” 2008, doi: 10.1109/ELINSL.2008.4570381.
- [37] B. Lee, J. Z. Liu, B. Sun, C. Y. Shen, and G. C. Dai, “Thermally conductive and

- electrically insulating EVA composite encapsulant for solar photovoltaic (PV) cell," *Express Polymer Letters*, 2008, doi: 10.3144/expresspolymlett.2008.42.
- [38] H. Chen *et al.*, "Thermal conductivity of polymer-based composites: Fundamentals and applications," *Progress in Polymer Science*, vol. 59, pp. 41–85, 2016, doi: 10.1016/j.progpolymsci.2016.03.001.
- [39] S. M. Lebedev and O. S. Gefle, "Evaluation of electric, morphological and thermal properties of thermally conductive polymer composites," *Applied Thermal Engineering*, 2015, doi: 10.1016/j.applthermaleng.2015.08.046.
- [40] X. Chen, Y. Su, D. Reay, and S. Riffat, "Recent research developments in polymer heat exchangers - A review," *Renewable and Sustainable Energy Reviews*. 2016, doi: 10.1016/j.rser.2016.03.024.
- [41] S. Zhou, Y. Chen, H. Zou, and M. Liang, "Thermally conductive composites obtained by flake graphite filling immiscible Polyamide 6/Polycarbonate blends," *Thermochimica Acta*, 2013, doi: 10.1016/j.tca.2013.05.027.
- [42] B. Debelak and K. Lafdi, "Use of exfoliated graphite filler to enhance polymer physical properties," *Carbon*, 2007, doi: 10.1016/j.carbon.2007.05.010.
- [43] Q. B. Ho, O. Osazuwa, R. Modler, M. Daymond, M. T. Gallerneault, and M. Kontopoulou, "Exfoliation of graphite and expanded graphite by melt compounding to prepare reinforced, thermally and electrically conducting polyamide composites," *Composites Science and Technology*, 2019, doi: 10.1016/j.compscitech.2019.03.024.
- [44] S. Ghosh *et al.*, "Extremely high thermal conductivity of graphene: Prospects for thermal management applications in nanoelectronic circuits," *Applied Physics Letters*, 2008, doi: 10.1063/1.2907977.
- [45] E. Pop, D. Mann, Q. Wang, K. Goodson, and H. Dai, "Thermal conductance of an individual single-wall carbon nanotube above room temperature," *Nano Letters*, 2006, doi: 10.1021/nl052145f.
- [46] A. Li, C. Zhang, and Y. F. Zhang, "Thermal conductivity of graphene-polymer composites: Mechanisms, properties, and applications," *Polymers*. 2017, doi: 10.3390/polym9090437.
- [47] C. Pan, K. Kou, Y. Zhang, Z. Li, and G. Wu, "Enhanced through-plane thermal conductivity of PTFE composites with hybrid fillers of hexagonal boron nitride platelets and aluminum nitride particles," *Composites Part B: Engineering*, 2018, doi: 10.1016/j.compositesb.2018.07.019.
- [48] T. M. L. Dang, C. Y. Kim, Y. Zhang, J. F. Yang, T. Masaki, and D. H. Yoon, "Enhanced thermal conductivity of polymer composites via hybrid fillers of anisotropic aluminum nitride whiskers and isotropic spheres," *Composites Part B: Engineering*, 2017, doi: 10.1016/j.compositesb.2017.02.008.

- [49] T. L. Li and S. L. C. Hsu, "Enhanced thermal conductivity of polyimide films via a hybrid of micro- and nano-sized boron nitride," *Journal of Physical Chemistry B*, 2010, doi: 10.1021/jp101857w.
- [50] B. Mortazavi, M. Baniassadi, J. Bardon, and S. Ahzi, "Modeling of two-phase random composite materials by finite element, Mori-Tanaka and strong contrast methods," *Composites Part B: Engineering*, 2013, doi: 10.1016/j.compositesb.2012.05.015.
- [51] W. Tian and R. Yang, "Phonon transport and thermal conductivity percolation in random nanoparticle composites," *CMES - Computer Modeling in Engineering and Sciences*, 2008, doi: 10.3970/cmes.2008.024.123.
- [52] Q. Liao, Z. Liu, W. Liu, C. Deng, and N. Yang, "Extremely High Thermal Conductivity of Aligned Carbon Nanotube-Polyethylene Composites," *Scientific Reports*, 2015, doi: 10.1038/srep16543.
- [53] X. Zhao and L. Ye, "Structure and properties of highly oriented polyoxymethylene/multi-walled carbon nanotube composites produced by hot stretching," *Composites Science and Technology*, 2011, doi: 10.1016/j.compscitech.2011.05.011.
- [54] Z. Liu *et al.*, "Electric-field-induced out-of-plane alignment of clay in poly(dimethylsiloxane) with enhanced anisotropic thermal conductivity and mechanical properties," *Composites Science and Technology*, 2018, doi: 10.1016/j.compscitech.2018.06.015.
- [55] C. Pan, J. Zhang, K. Kou, Y. Zhang, and G. Wu, "Investigation of the through-plane thermal conductivity of polymer composites with in-plane oriented hexagonal boron nitride," *International Journal of Heat and Mass Transfer*, vol. 120, no. December, pp. 1–8, 2018, doi: 10.1016/j.ijheatmasstransfer.2017.12.015.
- [56] B. Wolfgang and S. Rudtsch, "Thermal Properties," in *Springer Handbook of Materials Measurement Methods*, Springer, Berlin, Heidelberg, 2006, pp. 399–429.
- [57] N. Yüksel, "The Review of Some Commonly Used Methods and Techniques to Measure the Thermal Conductivity of Insulation Materials," in *Insulation Materials in Context of Sustainability*, 2016.
- [58] "Guarded-Hot-Plate method for determining thermal conductivity (GHP)," *Tec-science*. <https://www.tec-science.com/thermodynamics/heat/guarded-hot-plate-method-for-determining-thermal-conductivity-ghp/> (accessed Nov. 04, 2020).
- [59] "Heat-Flow-Meter method for determining thermal conductivity (HFM)," *Tec-science*. <https://www.tec-science.com/thermodynamics/heat/heat-flow-meter-method-for-determining-thermal-conductivity-hfm/> (accessed Nov. 04, 2020).

- [60] W. J. Parker, R. J. Jenkins, C. P. Butler, and G. L. Abbott, "Flash method of determining thermal diffusivity, heat capacity, and thermal conductivity," *Journal of Applied Physics*, 1961, doi: 10.1063/1.1728417.
- [61] NETZSCH, "Operating instructions HyperFlash apparatus LFA 467." 2012.
- [62] "Laser flash analysis," *Wikipedia*. https://en.wikipedia.org/wiki/Laser_flash_analysis (accessed Nov. 16, 2020).
- [63] NETZSCH, "Laser Flash Technique (LFA)." <https://www.netzsch-thermal-analysis.com/en/contract-testing/methods/laser-flash-technique-lfa/> (accessed Nov. 16, 2020).
- [64] W. J. Parker and R. J. Jenkins, "Thermal conductivity measurements on bismuth telluride in the presence of a 2 MeV electron beam," *Advanced Energy Conversion*, 1962, doi: 10.1016/0365-1789(62)90012-7.
- [65] R. D. Cowan, "Pulse method of measuring thermal diffusivity at high temperatures," *Journal of Applied Physics*, 1963, doi: 10.1063/1.1729564.
- [66] J. A. Cape and G. W. Lehman, "Temperature and finite pulse-time effects in the flash method for measuring thermal diffusivity," *Journal of Applied Physics*, 1963, doi: 10.1063/1.1729711.
- [67] R. C. Heckman, "Finite pulse-time and heat-loss effects in pulse thermal diffusivity measurements," *Journal of Applied Physics*, 1973, doi: 10.1063/1.1662393.
- [68] L. M. Clark and R. E. Taylor, "Radiation loss in the flash method for thermal diffusivity," *Journal of Applied Physics*, 1975, doi: 10.1063/1.321635.
- [69] Linseis, "Laser flash analysis LFA 1000." 2018, [Online]. Available: http://www.ribori-instrumentation.com/wp-content/uploads/2018/10/LINSEIS_LFA_1000_2000.pdf.
- [70] A. Publisher, "Importance of Modeling and Simulation of Materials in Research," *Journal of Modeling and Simulation of Materials*, vol. 1, no. 1, pp. 1–2, 2018, doi: 10.21467/jmsm.1.1.1-2.
- [71] S. M. Ha *et al.*, "Thermal conductivity of graphite filled liquid crystal polymer composites and theoretical predictions," *Composites Science and Technology*, 2013, doi: 10.1016/j.compscitech.2013.08.022.
- [72] R. L. McCullough, "Generalized combining rules for predicting transport properties of composite materials," *Composites Science and Technology*, 1985, doi: 10.1016/0266-3538(85)90087-9.
- [73] H. J. Ott, "THERMAL CONDUCTIVITY OF COMPOSITE MATERIALS.," *Plastics and Rubber Processing and Applications*, 1981.

- [74] M. James Clerk, *A treatise on electricity and magnetism*. 2010.
- [75] H. W. Russell, "PRINCIPLES OF HEAT FLOW IN POROUS INSULATORS," *Journal of the American Ceramic Society*, 1935, doi: 10.1111/j.1151-2916.1935.tb19340.x.
- [76] D. A. G. Bruggeman, "Berechnung verschiedener physikalischer Konstanten von heterogenen Substanzen. I. Dielektrizitätskonstanten und Leitfähigkeiten der Mischkörper aus isotropen Substanzen," *Annalen der Physik*, 1935, doi: 10.1002/andp.19354160705.
- [77] J. C. H. Affdl and J. L. Kardos, "The Halpin-Tsai equations: A review," *Polymer Engineering & Science*. 1976, doi: 10.1002/pen.760160512.
- [78] T. B. Lewis and L. E. Nielsen, "Dynamic mechanical properties of particulate-filled composites," *Journal of Applied Polymer Science*, 1970, doi: 10.1002/app.1970.070140604.
- [79] S. Zhai, P. Zhang, Y. Xian, J. Zeng, and B. Shi, "Effective thermal conductivity of polymer composites: Theoretical models and simulation models," *International Journal of Heat and Mass Transfer*. 2018, doi: 10.1016/j.ijheatmasstransfer.2017.09.067.
- [80] S. Zhou *et al.*, "Modeling the in-plane thermal conductivity of a graphite/polymer composite sheet with a very high content of natural flake graphite," *Carbon*, 2012, doi: 10.1016/j.carbon.2012.06.045.
- [81] G. Zhang *et al.*, "A percolation model of thermal conductivity for filled polymer composites," *Journal of Composite Materials*, 2010, doi: 10.1177/0021998309349690.
- [82] T. Y. Wang and J. L. Tsai, "Investigating thermal conductivities of functionalized graphene and graphene/epoxy nanocomposites," *Computational Materials Science*, 2016, doi: 10.1016/j.commatsci.2016.05.039.
- [83] F. Zhou and G. Cheng, "Lattice Boltzmann model for predicting effective thermal conductivity of composite with randomly distributed particles: Considering effect of interactions between particles and matrix," *Computational Materials Science*, 2014, doi: 10.1016/j.commatsci.2014.05.039.
- [84] Z. Fang *et al.*, "Geometrical Effect on Thermal Conductivity of Unidirectional Fiber-Reinforced Polymer Composite along Different In-plane Orientations," *Applied Composite Materials*, 2018, doi: 10.1007/s10443-017-9664-y.
- [85] R. Brooks, "Injection Molding Based Techniques," in *Comprehensive Composite Materials*, 2000.
- [86] Polyplastics, "The outline of injection molding." <https://www.polyplastics.com/en/support/mold/outline/index.html> (accessed

Nov. 24, 2020).

- [87] S.-J. Liu, "Injection molding in polymer matrix composites," in *Manufacturing Techniques for Polymer Matrix Composites (PMCs)*, 2012.
- [88] J. Brezinová and A. Guzanová, "Friction conditions during the wear of injection mold functional parts in contact with polymer Composites," *Journal of Reinforced Plastics and Composites*, vol. 29, no. 11, pp. 1712–1726, 2010, doi: 10.1177/0731684409341675.
- [89] S. H. Park and M. Y. Lyu, "Observation of Two-Dimensional Shaped Aluminum Flake Orientation During Injection Molding and Its Orientation Mechanism," *Macromolecular Research*, vol. 27, no. 5, pp. 481–489, 2019, doi: 10.1007/s13233-019-7097-1.
- [90] T. Wieme, L. Duan, N. Mys, L. Cardon, and D. R. D'hooge, "Effect of matrix and graphite filler on thermal conductivity of industrially feasible injection molded thermoplastic composites," *Polymers*, vol. 11, no. 1, pp. 4–6, 2019, doi: 10.3390/polym11010087.
- [91] M. A. Peydró, F. Parres, J. E. Crespo, and D. Juárez, "Study of rheological behavior during the recovery process of high impact polystyrene using cross-WLF model," *Journal of Applied Polymer Science*, 2011, doi: 10.1002/app.33444.
- [92] M. J. Assael, K. Gialou, K. Kakosimos, and I. Metaxa, "Thermal Conductivity of Reference Solid Materials 1," vol. 25, no. 2, 2004.
- [93] A. Philipp, J. F. Eichinger, R. C. Aydin, A. Georgiadis, C. J. Cyron, and M. Retsch, "The accuracy of laser flash analysis explored by finite element method and numerical fitting," *Heat and Mass Transfer/Waerme- und Stoffuebertragung*, 2019, doi: 10.1007/s00231-019-02742-7.
- [94] L. M. Evans *et al.*, "Transient thermal finite element analysis of CFC-Cu ITER monoblock using X-ray tomography data," *Fusion Engineering and Design*, vol. 100, no. June, pp. 100–111, 2015, doi: 10.1016/j.fusengdes.2015.04.048.
- [95] T. Ohmura, M. Tsuboi, and T. Tomimura, "Estimation of the Mean Thermal Conductivity of Anisotropic Materials," vol. 23, no. 3, pp. 843–853, 2002.
- [96] MSC Software, "Interface To MD Nastran Preference Guide Volume 2: Thermal Analysis." 2009.
- [97] A. Philipp, J. F. Eichinger, R. C. Aydin, A. Georgiadis, J. Cyron, and M. Retsch, "Supplementary Material The accuracy of laser flash analysis explored by finite element modeling and numerical fitting Finite element modeling," vol. 42, no. M, pp. 1–4.
- [98] H. Sun *et al.*, "Graphite fluoride reinforced PA6 composites: Crystallization and

- mechanical properties,” *Materials Today Communications*, vol. 16, no. May, pp. 217–225, 2018, doi: 10.1016/j.mtcomm.2018.06.007.
- [99] K. Sever, I. H. Tavman, Y. Seki, A. Turgut, M. Omastova, and I. Ozdemir, “Electrical and mechanical properties of expanded graphite/high density polyethylene nanocomposites,” *Composites Part B: Engineering*, vol. 53, pp. 226–233, 2013, doi: 10.1016/j.compositesb.2013.04.069.
- [100] S. Y. Fu, X. Q. Feng, B. Lauke, and Y. W. Mai, “Effects of particle size, particle/matrix interface adhesion and particle loading on mechanical properties of particulate-polymer composites,” *Composites Part B: Engineering*, vol. 39, no. 6, pp. 933–961, 2008, doi: 10.1016/j.compositesb.2008.01.002.
- [101] N. F. Braga, F. R. Passador, E. Saito, and F. H. Cristovan, “Effect of Graphite Content on The Mechanical Properties of Acrylonitrile-Butadiene-Styrene (ABS),” *Macromolecular Symposia*, vol. 383, no. 1, pp. 1–6, 2019, doi: 10.1002/masy.201800018.
- [102] A. Yasmin and I. M. Daniel, “Mechanical and thermal properties of graphite platelet/epoxy composites,” *Polymer*, 2004, doi: 10.1016/j.polymer.2004.09.054.
- [103] Y. Li, D. Wu, and G. Chen, “Preparation and characterization of high-density polyethylene/expanded graphite conducting masterbatch,” *Journal of Applied Polymer Science*, 2007, doi: 10.1002/app.25842.
- [104] T. Wieme, D. Tang, L. Delva, D. R. D’hooge, and L. Cardon, “The relevance of material and processing parameters on the thermal conductivity of thermoplastic composites,” *Polymer Engineering and Science*. 2018, doi: 10.1002/pen.24667.
- [105] S. Hamanaka, K. Yamashita, C. Nonomura, T. B. N. Thi, T. Wakano, and A. Yokoyama, “Measurement of fiber orientation distribution in injection-molded composites with high filler content,” *AIP Conference Proceedings*, vol. 1914, no. December, pp. 1–6, 2017, doi: 10.1063/1.5016776.
- [106] R. Brooks, “Injection Molding Based Techniques,” *Comprehensive Composite Materials*, pp. 999–1028, 2000, doi: 10.1016/b0-08-042993-9/00189-3.
- [107] A. Király and F. Ronkay, “Effect of processing technology on the morphological, mechanical and electrical properties of conductive polymer composites,” *Journal of Polymer Engineering*, vol. 33, no. 8, pp. 691–699, 2013, doi: 10.1515/polyeng-2013-0038.
- [108] J. P. Holman, “Natural convection systems,” in *Heat transfer*, 10th ed., McGraw-Hill, 2009, pp. 327–362.